Downloaded from orbit.dtu.dk on: Apr 19, 2024

DTU Library

Upconversion Detector for Remote Gas Sensing

Meng, Lichun

Publication date:
2018

Document Version
Publisher's PDF, also known as Version of record

Link back to DTU Orbit

Citation (APA):
Meng, L. (2018). *Upconversion Detector for Remote Gas Sensing*. Technical University of Denmark.

General rights
Copyright and moral rights for the publications made accessible in the public portal are retained by the authors and/or other copyright owners and it is a condition of accessing publications that users recognise and abide by the legal requirements associated with these rights.

- Users may download and print one copy of any publication from the public portal for the purpose of private study or research.
- You may not further distribute the material or use it for any profit-making activity or commercial gain
- You may freely distribute the URL identifying the publication in the public portal

If you believe that this document breaches copyright please contact us providing details, and we will remove access to the work immediately and investigate your claim.

Ph.D. Thesis

Upconversion Detector for Remote Gas Sensing

Lichun MENG

DTU Risø Campus 2018

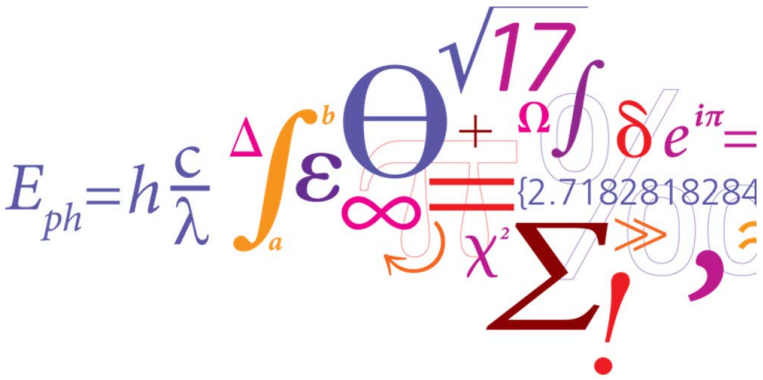

DTU Fotonik
Department of Photonics Engineering

"Linearity is beautiful, but nonlinearity is wonderful. Symmetry is brilliant, but asymmetry is genius."

Lichun Meng

TECHNICAL UNIVERSITY OF DENMARK

Abstract

Optical Sensor Technology Group
DTU Fotonik, Risø campus

Doctor of Philosophy

Upconversion Detector for Remote Gas Sensing

by Lichun MENG

An intracavity-enhanced upconversion detector (UCD) for range-resolved atmospheric CH_4 sensing over a long distance is demonstrated. The UCD detects an IR signal at 1645 nm by mixing with a 150 W 1064 nm laser inside a bulk periodically poled $LiNbO_3$ to produce an upconverted signal with a maximum efficiency of $\sim 40\,\%$. A photomultiplier tube is used to measure the upconverted signal yielding a noise equivalent power of $127\,\mathrm{fW}/\sqrt{\mathrm{Hz}}$ for the whole detection system. The UCD outperforms a conventional APD in an atmospheric CH_4 DIAL measurement, and the differential absorption optical depths given by the UCD have less than 11 % error at ranges between 3 km and 9 km. In addition, the UCD is based on a ring cavity with the ability of single-longitudinal mode pumping, which makes the detector free of frequency beat noise. In an experimental demonstration of high-speed IR detection, a UCD with a bandwidth larger than 1 GHz is demonstrated. Performing both experimental and theoretical investigation of the noise property of the UCD is another essential content of this thesis. Two additional UCDs (one is a single-pass, short-wavelength pumped UCD, and the other is an intracavity-enhanced, long-wavelength pumped UCD) are built in order to study the noise sources (USPDC, SHG-SPDC, upconverted thermal radiation and upconverted SRS processes) systematically. The following conclusions are obtained: 1) for the short-wavelength pumped UCD, the USPDC noise due to the RDC error of PPLN crystal is the primary noise source when the IR signal wavelength is smaller than 2 µm, and the upconverted thermal radiation becomes the primary noise source when the wavelength is larger than 3 µm. 2) As a newly identified noise source, the SHG-SPDC process can be avoided by choosing a proper combination of PPLN poling period, operating temperature and bandpass filter. 3) For the long-wavelength pumped, intracavity-enhanced UCD, the USPDC process is avoided fundamentally, but the noise count rate can be larger than $5 \times 10^4/\mathrm{s}$ due to the upconverted SRS process, especially when the Raman frequency shift is small. During the process of noise investigation, the radially modulated pattern of the USPDC noise is first observed. Based on that discovery, a noise reduction method for the short-wavelength pumped UCD is proposed: collecting the upconverted signal at the local minimum of the noise pattern, and the noise can be reduced with the use of noncollinear QPM condition and a proper spatial filter. This simple technique results in a 14 dB reduction of dark-count rate with only 2.2 dB signal loss.

Acknowledgements

First of all, I would like to thank my supervisors Peter John Rodrigo and Christian Pedersen. They guided me through this project and helped me whenever I need it. We had numerous discussions about the basic theory and the experiment design together, and it was always informative and inspiring. I also would like to thank Lasse Høgstedt, my external supervisor, who designed and built our first generation UCD before. I am grateful for his generous sharing of his experience, which helped me avoid unnecessary obstacles during the project. I would furthermore thank Peter Tidemand-Lichtenberg for his always joining in our group discussion and providing valuable ideas and suggestions for my project. From the Optical Sensor Technology group, I would like to thank all my colleagues and friends for their support and help, especially Yupei Tseng for the fruitful discussion with her about the fabrication of PPLN crystal and Ajanta Barh for the discussion on the noise modelling.

I would like to thank Andreas Fix from the Atmospheric Physics Department at the German Aerospace Center (DLR) for his total involvement in the experiment of lidar measurement, his help in the lab was crucial for our successful experiment. I also would like to thank my other external partner Anuja Padhye from the Optical Parametric Oscillators group in ICFO, Spain. Her cooperation in the dark lab for many hours provides solid experimental support for our noise investigation.

Lichun Meng
October 2018, Risø campus DTU

List of Publications

Journal Paper, First Author

1. **GHz-bandwidth upconversion detector using a unidirectional ring cavity to reduce multilongitudinal mode pump effects.**
Lichun Meng, Lasse Høgstedt, Peter Tidemand-Lichtenberg, Christian Pedersen, and Peter John Rodrigo.
Optics Express, Volume 25, Number 13, Pages 14783-14794 (2017)

2. **Upconversion detector for range-resolved DIAL measurement of atmospheric CH_4.**
Lichun Meng, Andreas Fix, Martin Wirth, Lasse Høgstedt, Peter Tidemand-Lichtenberg, Christian Pedersen, and Peter John Rodrigo.
Optics Express, Volume 26, Number 4, Pages 3850-3860 (2018)

3. **Enhancing the detectivity of an upconversion single-photon detector by spatial filtering of upconverted parametric fluorescence.**
Lichun Meng, Lasse Høgstedt, Peter Tidemand-Lichtenberg, Christian Pedersen, and Peter John Rodrigo.
Optics Express, Volume 26, Number 19, Pages 24712-24722 (2018)

Journal Paper, Co-Author

1. **Mid-IR hyperspectral imaging for label-free histopathology and cytology.**
Hermes, M.; Morrish, R. Brandstrup; Huot, Laurent; Meng, Lichun; Junaid, Saher; Tomko, J.; Lloyd, G. R.; Masselink, W. T.; Tidemand-Lichtenberg, Peter ; Pedersen, Christian; Palombo, F.; Stone, N.
Journal of Optics, Volume 20, Number 2, Page 023002 (2018)

2. **Time-resolved infrared photoluminescence spectroscopy using parametric three-wave mixing with angle-tuned phase matching.**
Søren Roesgaard, Lichun Meng, Peter Tidemand-Lichtenberg, Jeppe Seidelin Dam, Peter John Rodrigo, Christian Pedersen, and Brian Julsgaard.
Optics Letters, Volume 43, Number 12, Pages 3001-3004 (2018)

Conference Contribution, First Author

1. **Intracavity upconversion for IR absorption lidar: Comparison of linear and ring cavity designs.**
Lichun Meng, Lasse Høgstedt, Peter Tidemand-Lichtenberg, Christian Pedersen, and Peter John Rodrigo.
2017 Conference on Lasers and Electro-Optics Europe and European Quantum Electronics Conference. IEEE, 2017. p. 1-1.

2. **Upconversion detector for methane atmospheric sensor.**
Lichun Meng, Andreas Fix, Lasse Høgstedt, Peter Tidemand-Lichtenberg, Christian Pedersen, and Peter John Rodrigo.
Optics and Photonics for Energy and the Environment, EE 2017. Vol. Part F65-EE 2017 OSA - The Optical Society, 2017. EW4B.2.

3. **S/N ratio of an upconversion detector dominated by upconverted spontaneous parametric down-conversion noise.**
Lichun Meng, Lasse Høgstedt, Peter Tidemand-Lichtenberg, Christian Pedersen, and Peter John Rodrigo.
Mid-Infrared Coherent Sources 2018. Optical Society of America OSA, 2018. Paper MM4C.5.

Supervised Master Project

1. **Upconversion ringdown spectroscopy for medical diagnostics.**
Author: Aaron Anthony Samuel Doug Deen
Supervisors: Peter Tidemand-Lichtenberg, Anders Brusch, David Balslev-Harder, Peter John Rodrigo, Lichun Meng and Christian Pedersen

Contents

Abstract v

Acknowledgements vii

List of Publications ix

Contents xi

List of Abbreviations xiii

1 Introduction 1
- 1.1 Structure of the Thesis . . . 1
- 1.2 Motivation of the Project . . . 2
- 1.3 State-of-the-art Review . . . 4
  - 1.3.1 Pioneers of Frequency Upconversion . . . 4
  - 1.3.2 Recent Developments in Upconversion Detection . . . 6
- 1.4 Project Goals . . . 8

2 Theory of Frequency Upconversion 11
- 2.1 Theory of 2nd order Nonlinear Optical Process . . . 11
  - 2.1.1 2nd order Nonlinear Susceptibility . . . 11
  - 2.1.2 Coupled-Wave Equations for Sum and Difference Frequency Generation . . . 12
  - 2.1.3 SPDC and Vacuum Fluctuation . . . 14
- 2.2 Phase Matching Condition . . . 15
  - 2.2.1 Phase Matching Condition and Upconversion Efficiency . . . 15
  - 2.2.2 Quasi-Phase Matching . . . 17
  - 2.2.3 Super-Phase Matching . . . 19
- 2.3 Periodically Poled $LiNbO_3$ . . . 21
  - 2.3.1 Fabrication of PPLN and the Poling Errors . . . 21
  - 2.3.2 Incidental Parametric Processes in PPLN . . . 22

3 Detector Configuration 25
- 3.1 Short-wavelength-pumped UCD with Intracavity Enhancement . . . 25
  - 3.1.1 UCD Design . . . 25
  - 3.1.2 Characterization of PPLN Crystals . . . 28
- 3.2 Characterization of the UCD . . . 30
  - 3.2.1 Intracavity Power . . . 31
  - 3.2.2 Upconversion Efficiency and Background Noise . . . 32
- 3.3 UCD for Weak Signal Detection . . . 32
  - 3.3.1 Experimental Setup and Results . . . 32
  - 3.3.2 Signal-to-Noise Ratio . . . 34

4 Noise Properties of the Upconversion Detector **37**
4.1 Frequency Beat Noise . . . 37
4.1.1 Introduction . . . 38
4.1.2 Theory . . . 39
4.1.3 Experimental Setup . . . 41
4.1.4 Results . . . 43
4.1.5 Discussion and Conclusion . . . 47
4.2 Noise from the Parametric Process . . . 49
4.2.1 Introduction . . . 50
4.2.2 Theory . . . 51
4.2.3 Experimental Setup . . . 55
4.2.4 Results . . . 56
4.2.5 Conclusion . . . 59
4.3 Upconverted SRS Noise of the Long-wavelength-pumped UCD . . . 61
4.3.1 Theory . . . 61
4.3.2 Experimental Setup . . . 62
4.3.3 Results and Discussion . . . 63
4.4 Pattern of USPDC and Noise Reduction . . . 64
4.4.1 Introduction . . . 64
4.4.2 Spatial Distribution of USPDC Noise . . . 65
4.4.3 Signal-to-Noise Ratio Improvement for the Short-wavelength-pumped Upconversion Single-photon Detector . . . 69
4.4.4 Summary and Discussion . . . 72
4.5 Choice of Detectors for IR Detection . . . 73

5 Atmospheric CH_4 Sensing Using Upconversion Detector **77**
5.1 Introduction . . . 77
5.2 Theory . . . 78
5.2.1 Detector Étendue . . . 78
5.2.2 Signal-to-Noise Ratio . . . 79
5.3 Characteristics of the UCD . . . 79
5.3.1 Setup of the UCD . . . 79
5.3.2 Quantum Efficiency of the UCD . . . 81
5.3.3 Noise Properties of the UCD . . . 82
5.4 Experiment . . . 83
5.4.1 IPDA Measurement . . . 83
5.4.2 DIAL Measurement . . . 86
5.5 Discussion . . . 88
5.6 Summary . . . 89

6 Conclusion and Outlook **91**
6.1 Conclusion . . . 91
6.2 Outlook . . . 92

A Derivation of $|\widetilde{g}(\Delta k)|^2$ **95**

B Poster Presented at DOPS 2016 **99**

C Poster at CLEO Europe 2017 **101**

Bibliography **103**

List of Abbreviations

APD	**A**valanche **P**hoto**d**iode
DFG	**D**ifference **F**requency **G**eneration
SHG	**S**econd **H**armonic **G**eneration
SFG	**S**um **F**requency **G**eneration
DIAL	**D**ifferential **A**bsorption **L**idar
EM-CCD	**E**lectron **M**ultiplying **C**harge **C**oupled **D**evice
FFT	**F**ast **F**ourier **T**ransform
FOV	**F**ield **O**f **V**iew
FWHM	**F**ull **W**idth at **H**alf **M**aximum
LIDAR/lidar	**Li**ght **D**etection **A**nd **R**anging
MCT	**M**ercury **C**admium **T**elluride
MIR	**M**id-**I**nf**r**ared
NEP	**N**oise **E**quivalent **P**ower
NIR	**N**ear-**I**nf**r**ared
OPO	**O**ptical **P**arametric **O**scillator
OSA	**O**ptical **S**pectrum **A**nalyzer
PMT	**P**hoto**m**ultiplier **T**ube
PPLN	**P**eriodically **P**oled **L**ithium **N**iobate
QE	**Q**uantum **E**fficiency
QPM	**Q**uasi-**P**hase **M**atching
RDC	**R**andom **D**uty **C**ycle
SNR	**S**ignal-to-**N**oise **R**atio
UCD	**Up**conversion **D**etector
SPDC	**S**pontaneous **P**arametric **Down**conversion
SRS	**S**pontaneous **R**aman **S**cattering
USPDC	**U**pconverted **S**pontaneous **P**arametric **Down**conversion

Chapter 1

Introduction

I worked as a Ph.D. student in the Optical Sensor Technology Group, DTU Fotonik, Department of Photonics Engineering, Technical University of Denmark between Nov 2015 and Nov 2018. This thesis presents my original research activities that I performed during that period. The theoretical studies and most of the laboratory work were done in DTU Fotonik Risø Campus, Roskilde, Denmark. Another two external research activities were the collaboration with Atmospheric Physics Department in the German Aerospace Center (DLR) in Oberpfaffenhofen, Germany and with the Optical Parametric Oscillators group in ICFO, Barcelona, Spain, separately. The contributions from our external partners will be explicitly addressed along with the experiment details in the corresponding chapters.

My Ph.D. study is one part of the Mid-TECH project, which is funded by the HORIZON 2020 Research and Innovation Program under the grant agreement NO. 642661. The Mid-TECH project comprises 8 European academic/industrial partners. The objective of Mid-TECH is to promote the development of mid-infrared (MIR) technologies with focus on MIR light sources, novel MIR detection (upconversion technology), and new MIR applications. I am ESR 4 in the Mid-TECH project among other 14 Ph.D. students, and my task mainly focuses on the development of an upconversion detector for atmospheric lidar application.

1.1 Structure of the Thesis

This thesis presents both theoretical and experimental investigation of the upconversion technology for IR sensing. In particular, the design of a short-wavelength-pumped, intracavity-enhanced upconversion detector along with its characterization and application will be addressed in detail; the different noise sources originating from the upconversion module and their effects on the performance of the system are investigated. The potential of the upconversion detection technology is explored by measuring the atmospheric CH_4 over a long distance.

Chapter 1 starts with the motivation of this Ph.D. project, i.e. using frequency upconversion for IR detection. Afterwards, the development of nonlinear optics over the past 60 years will be introduced briefly. At last, as a historical background of this project, a short review of frequency upconversion and its application on IR detection will be presented.

Following the introduction on the background of the frequency upconversion, the basic concepts of 2nd order nonlinear optics along with some important formulas will be presented in Chapter 2. Considering that a bulk periodically poled $LiNbO_3$ is used as the $\chi^{(2)}$ material in this project, the basic principle of QPM and the fundamental properties of the PPLN will be discussed in detail. In general, the material in this chapter provides a theoretical framework for further investigation of the frequency upconversion detector.

Chapter 3 begins with the design concept of the 2nd generation of upconversion detector (the 1st generation was developed in a previous Ph.D. project), which is followed by the introduction of the structure of the UCD. Some basic properties of the UCD such as the intracavity pump power, upconversion efficiency and background noise are characterized accordingly. These parameters serve as a reference to evaluate the performance of the UCD in the following experiments.

Chapter 4 focuses on the noise properties of the UCD. First of all, the experimental investigation of the frequency beat noise due to the multi-longitudinal mode beating will be introduced. Based on the frequency analysis of the upconverted signal when an IR signal is amplitude-modulated at different frequencies, the detection bandwidth of the UCD is proved to be larger than 1 GHz. Secondly, three noise sources for the short-wavelength-pumped UCD: USPDC, SHG-SPDC and upconverted thermal noise are studied by measuring the noise of a single-pass upconversion detector working in different conditions. In order to explain the behaviour of those noise sources, theoretical models are built accordingly. In the third part of this chapter, the investigation of the upconverted SRS noise is presented. An intracavity-enhanced, long-wavelength-pumped UCD is built, and its noise power for different detection IR wavelengths is measured. Based on the measurement result and the theoretical analysis, it is concluded that the DCR due to the upconverted SRS noise is larger than 5×10^4/s in the UCD. At last, a discovery on the spatial distribution of the USPDC noise will be introduced. Based on this discovery, a simple method for noise reduction is developed.

An application of UCD for atmospheric gas sensing is demonstrated in Chapter 5. The details of the experiment along with the analysis of the result will be presented. The experimental results confirm that the UCD outperforms a conventional direct IR detector yielding more sensitive DIAL measurement in the long range.

The last chapter of this thesis is the conclusion and outlook. The main findings and outcomes of the project are summarized, and further suggested improvements of the UCD and its potential applications are listed.

1.2 Motivation of the Project

IR sensing and detection have broad applications ranging from the dynamic analysis of a single molecule to the astronomical observation of a galaxy. Benefiting from the emergence of new IR sources such as supercontinuum laser, OPO and QCL, the sensitivity of active-light-source based IR sensing system is experiencing significant advancement recently. However, the improvement of IR source is only a half of the story, the other half depends on the improvement of IR detector, especially for a passive IR detection system. The performance of conventional direct IR detectors is reaching the ceiling, and they cannot be further improved significantly due to their fundamental limit. In order to achieve a breakthrough, researchers start searching for other IR detection technologies that depend on entirely different working principles. In recent years, some new types of IR detectors have been reported and even been commercialized. Among these new-concept IR detection technologies, frequency upconversion is one of the promising ones that shows great potential for IR detection in the future.

Frequency upconversion detection is based on the 2nd order nonlinear SFG process of mixing an IR signal with a high-intensity pump field in $\chi^{(2)}$ material. Instead of measuring the IR signal directly, it is first translated spectrally (i.e. upconverted), and the upconverted signal is measured by a high-performance detector. Figure

1.1 is an overview of the detectivity of direct detectors working at different spec-

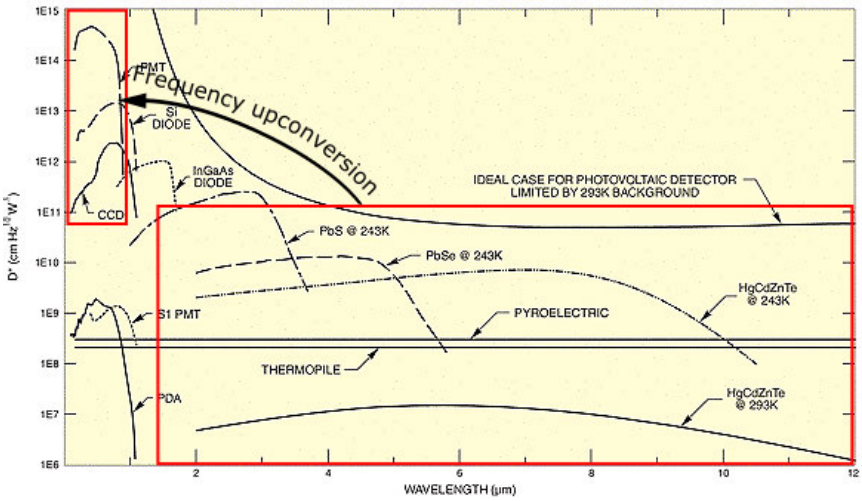

FIGURE 1.1: Detectivity of detectors working at different spectral regions (adapted from [1]).

tral regions. Generally speaking, the Si/InGaAs based detectors working in the VIS and/or NIR regions have higher detectivity in comparison to the ones working in the MIR/FIR region. By choosing a proper wavelength of the pump field, the upconverted signal carrying the same information as the IR signal can be transferred into the VIS or NIR region. Therefore, it is more efficient to measure the upconverted signal with a Si/InGaAs based detector compared with measuring the IR signal with a low-performance IR detector directly. Moreover, the UCD is capable of fast detection (high-bandwidth) and working at the room temperature without a complex cooling system. In contrast, conventional direct detectors for MIR/FIR signal detection usually have a limited detection bandwidth, and they need additional cryogenic cooling systems in order to reduce the thermal noise effectively.

Apparently, it is a two-step process during the upconversion detection. In order to get high total detection efficiency, it is necessary to achieve a high upconversion efficiency in the first step. However, it is challenging to achieve that because the upconversion (or SFG) is a weak nonlinear process in general. Fortunately, benefiting from the emergence of new nonlinear materials with relatively high 2nd order nonlinearity, UCD with high upconversion efficiency becomes possible, and they have already been reported in the literature recently. In this project, bulk PPLN crystals are applied in the UCD, which results in considerably high upconversion efficiency by taking advantage of its relatively larger d_{eff} ($\sim$14 pm/V) in comparison with other crystals as shown in table 1.1. In addition, upconversion with Type 0 phase matching (QPM) condition enables the wavelength tunability in a large spectral range by merely changing the poling period and/or the temperature of PPLN crystal.

	KTP	**BBO**	**LBO**	**CLBO**
d_{eff} **[pm/V]**	3.1	1.94	1.16	1.11

TABLE 1.1: d_{eff} of some commonly used nonlinear crystals [2].

1.3 State-of-the-art Review

As a branch of fundamental optics, nonlinear optics is relatively modern in comparison to the other branches. It became a research highlight in the 1960s, right after the invention of laser. After 20 years of nonlinear optics research work on upconversion detection, scientists generally agreed on that the upconversion efficiency was too low to be used for detection at that time. It was a negative conclusion due to the material and technical limitations back then, but most of the concepts and theoretical frameworks of upconversion detection were established, and these previous works made a full preparation for the future bloom of upconversion detection.

The second research highlight came at the beginning of the 21st century when new nonlinear materials became available. In particular, benefiting from the maturation of periodically poled nonlinear crystal technology, highly efficient IR detection based on frequency upconversion became possible.

All the work discussed in this thesis is based on the contributions of predecessors. In order to get a full picture of upconversion technology, it is necessary to introduce the historical line of the development of upconversion technology briefly.

1.3.1 Pioneers of Frequency Upconversion

As a 2nd order nonlinear process, frequency upconversion (or downconversion) is too weak to be observed in usual conditions. High-intensity optical field is demanded in order to observe nonlinear optical phenomena. Since the laser has high brightness in both spatial and spectral domain, it becomes an ideal tool for nonlinear optics investigations. Thus, Franken et al. [3] achieved the first demonstration of SHG using a pulsed ruby laser in 1962 (2 years after the invention of the first laser).

In the following decade, the theory of 2nd order nonlinear optics was established. The symmetry property of nonlinear crystal and its effects on the intensity of nonlinear interaction were discussed by D. A. Kleinman [4] in 1962. In the same year, a theoretical paper handling the parametric upconversion process was published by Armstrong et al. [5]. The phase matching conditions including the QPM shown in

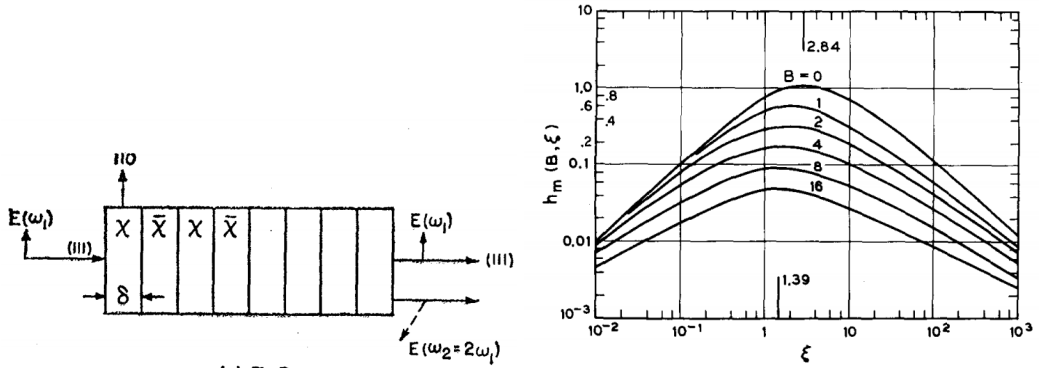

(a) (b)

FIGURE 1.2: (a) Periodic inversion of the nonlinear susceptibility (reproduced from [5]) and (b) focusing optimization for frequency conversion (reproduced from [6]).

figure 1.2a, were discussed under different circumstances. In addition, the idea of IR detection based on upconversion was proposed in that paper first. In 1968, the parametric process involving the Gaussian beam interaction was discussed by Boyd

and Kleinman [6]. They specified the optimal focus conditions for SHG, upconversion and OPO processes, respectively. Figure 1.2b shows the relation between the focusing parameter ξ and the merit function $h_m(B, \xi)$, where parameter B is affected by the double refraction angle.

Along with the progress of theoretical studies, a series of experimental demonstrations of upconversion was achieved. For example, an experiment conducted by Midwinter and Warner [7] achieved more than 1% upconversion efficiency by mixing the Hg emission line at 1.7 µm with a Q-switched ruby laser in a 10-mm long $LiNbO_3$ crystal in 1967. One year later, an upconversion image with 50 lines resolution was achieved experimentally by Midwinter [8] using the similar setup as

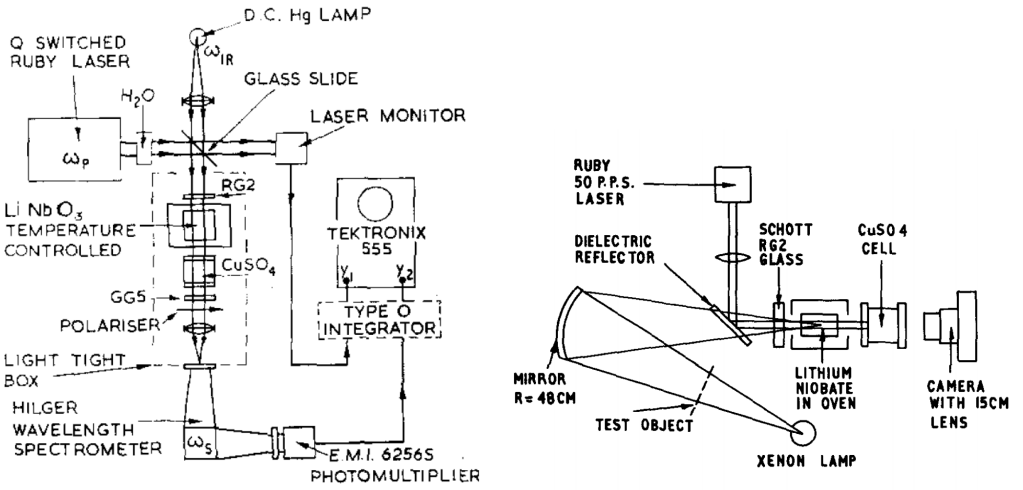

(a) (b)

FIGURE 1.3: Experimental setups for the IR (a) detection (reproduced from [7]) and (b) imaging (reproduced from [8]).

[7] except that the IR wavelength was changed to 1.6 µm. Figure 1.3a and figure 1.3b show the experimental setups used in [7] and [8] for IR detection and imaging, respectively.

The parametric amplification and the parametric fluorescence (SPDC) were observed in 1965 by Patel [9] and by Giordmaine et al. [10], respectively. In 1968, Byer and Harris wrote a theoretical paper [11] analyzing the spectral and the angular distribution of SPDC photon. Meanwhile, Giallorenzi and Tang drew a similar conclusion based on the QED theory [12]. The study of SPDC had little connection with the upconversion, but it is strongly related to the noise generation during the upconversion process, and these early studies on SPDC cleared the pavement for the discovery of upconversion noise, which was found at the very beginning stage of upconversion detection: the unexpected noise was reported in [7], where the NEP of the UCD was $0.1 \sim 0.5$ µW/cm^2. Even though the authors did not confirm the noise source, but they pointed out that the USPDC process could be the possible reason, which was theoretically confirmed by Tang in 1969 [13] using the QED theory. Figure 1.4 shows the Feynman diagrams of SPDC and USPDC processes, respectively.

Astronomical IR observation was one of the main areas where upconversion detection was used. In 1974, Gurski et al. published the first demonstration using an UCD for astronomical application [14]. They used a 1064 nm Nd:YAG laser as the optical pump that had 65 times greater effective duty cycle than the ruby laser,

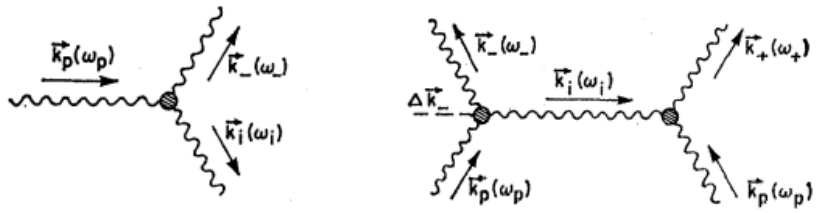

(a) (b)

FIGURE 1.4: Feynman diagrams of the (a) SPDC and the (b) USPDC processes (reproduced from [13]).

which yielded 45 times improvement of SNR. Afterwards, several similar applications emerged before Boyd wrote a review paper stating that the upconversion technology had not been proved to be a useful technology in astronomy. He also pointed out that the unexpected noise source should be inhibited, and a high power laser should be used as a pump in order to achieve high upconversion efficiency [15].

The intracavity-enhanced UCD was first demonstrated by Falk and See in 1977 [16]. Even though the circulating pump power was only several watts due to the high loss of laser cavity back then, it proved the concept of intracavity-enhanced upconversion. More importantly, their work showed another method of achieving effective upconversion for future researchers.

1.3.2 Recent Developments in Upconversion Detection

During 1980-2000, the upconversion technology experienced a decade of slow progress before its second highlight. Meanwhile, the technologies of semiconductors and lasers achieved considerable progress, and these technologies started being widely used in different applications, which gave birth to new experimental apparatuses. In particular, high-quality optical components such as HR coatings and filters became commercially available. These developments supported the reinvigoration of upconversion technology. Most importantly, nonlinear materials with high transparency, high damage threshold and high chemical stability became mature. One of the outstanding representatives is the PPLN crystal either in bulk or waveguide form.

PPLN waveguide-based SHG was demonstrated by Krishnan et al. in 2002 [17]. A 33-mm long PPLN waveguide yielded the highest normalized conversion efficiency of 150 %/Wcm^2 back then. Two years later, Roussev et al. working in the same group published a paper showing another PPLN waveguide-based upconversion detector for single-photon counting with an upconversion efficiency of 86% [18]. From 2006, intracavity-enhanced UCDs based on bulk PPLN crystals started being reported [19–22]. The specific designs of these UCDs differed from each other significantly, but their backbones were all 1064 nm lasers with Neodymium-doped gain media. Moreover, they all tried to upconvert the telecom band IR signal. Two typical setups for single-photon detection are shown in figure 1.5.

Even though these short-wavelength-pumped UCDs could achieve high upconversion efficiency (>90%), they all had a relatively high dark photon rate ($\sim 1 \times 10^5$/s), which limited their application in the field where a low background noise is demanded (e.g. quantum optics). With further investigation, USPDC process was

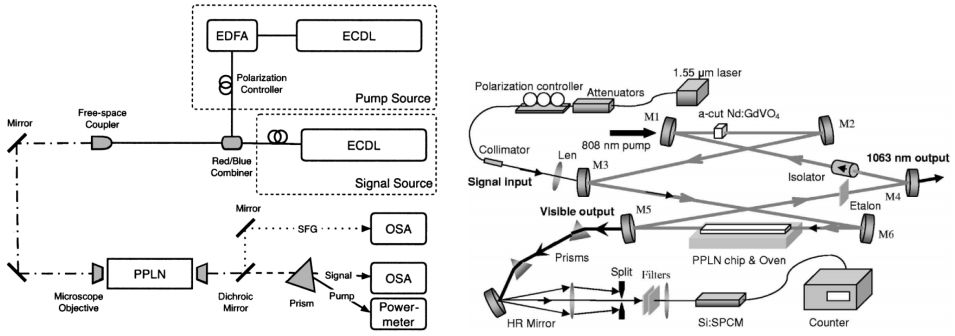

(a) (b)

FIGURE 1.5: (a) Waveguide (reproduced from [18]) and (b) bulk crystal (reproduced from [21]) PPLN-based UCDs for the single-photon counting detection.

pinpointed as the dominant noise source. Pelc et al. clarified the relation between the RDC error and the intensity of parametric noise generation both theoretically and experimentally [23, 24]. In order to remove the USPDC noise of UCD fundamentally, the long-wavelength-pumped UCD was introduced [25, 26]. The 1.55 µm photons mixed with a 1.9 µm pump in a PPLN waveguide yielded >80% upconversion efficiency and $\sim 1 \times 10^2$/s dark-count rate. One example setup using the long-wavelength pump is shown in figure 1.6a.

With the development of different UCDs, they started being used in other applications. For example, by combining with a lidar system, the UCD has been used for

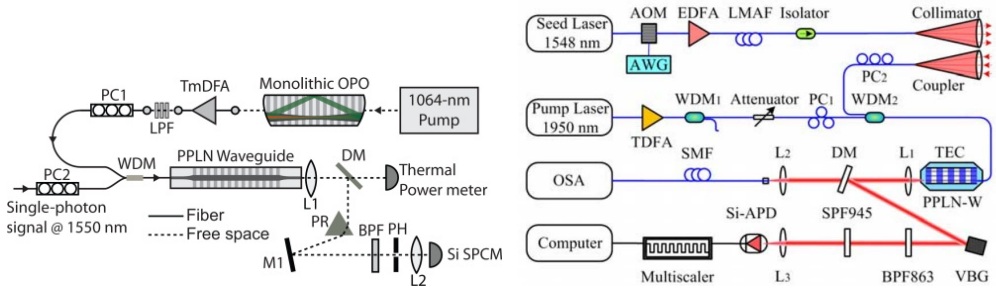

(a) (b)

FIGURE 1.6: (a) Long-wavelength-pumped UCD for single-photon counting (reproduced from [25]), (b) UCD for long-range aerosol lidar (reproduced from [27]).

the long-range aerosol detection [27] as shown in figure 1.6b, also for wind [28] and visibility [29] measurements. Benefiting from the high detectivity of UCD, the SNR of the lidar system was significantly improved. For example, SNR given by the UCD was 2 orders of magnitude larger than that of the InGaAs APD in [27]. Applications of UCD in reflectometry [30] and astronomical observation [31] were also reported.

One of the most important research areas of our Optical Sensor Technology group is to expand the application of upconversion technology. Back in 2010, Dam et al. from our group demonstrated the first high-resolution (more than 200×1000 pixels) upconversion image of thermally illuminated objects [32]. In 2012, another published paper showed single-photon MIR imaging using an intracavity-enhanced UCD with $\sim$ 20% upconversion efficiency [33]. Afterwards, new applications in the fields such as high-resolution spectroscopy [34], hyperspectral imaging [35] and gas sensing [36] started emerging rapidly. Especially after the kick-off of the Mid-TECH

project in 2015, research work on upconversion technology in our group is brought to a new height [37–43].

In 2014, Wong et al. from a NASA research group demonstrated an intracavity-enhanced UCD for a pW-level IR signal detection suggesting the potential of UCD for remote gas sensing [44]. Lasse Høgstedt from our group successfully demonstrated the first UCD based lidar measurements of atmospheric CO_2 in 2016 [45]. Figure 1.7 shows his experimental setup and the measurement result. Even though the UCD did not outperform the InGaAs based detector back then, it showed a great potential for further improvement. Therefore, one of the most important parts of this Ph.D. project is to continue exploring the potential of UCD for remote gas sensing. The detailed comparison between the experiment in [45] and my new work will be presented in Chapter 5 of this thesis.

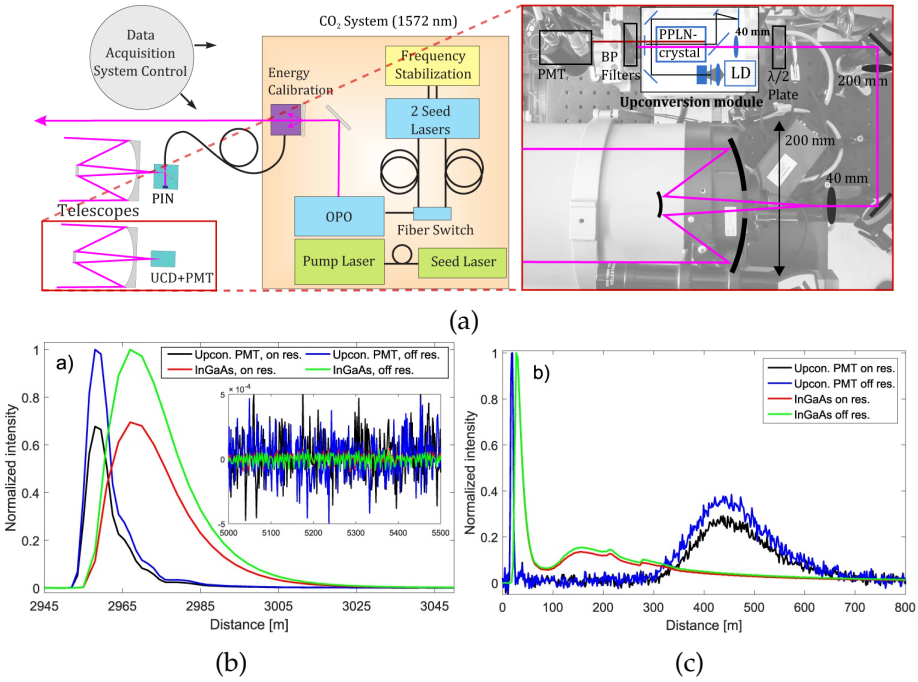

FIGURE 1.7: (a) Experimental setup for long-range atmospheric CO_2 sensing. (b) and (c) are the IPDA and DIAL measurement results given by the UCD and the InGaAs based direct detector, respectively (reproduced from [45]).

1.4 Project Goals

The primary goal of this Ph.D. project is to continue the investigation and development of an UCD for the application of remote gas (CH_4) sensing. In particular, it involves the design and building of the new generation of UCD, using UCD for atmospheric CH_4 sensing and UCD noise properties characterization.

1 Build and design a new intracavity-enhanced UCD using a bulk PPLN crystal as the $\chi^{(2)}$ material. Afterwards, optimize and characterize the performance of the UCD.

2 Perform atmospheric CH_4 sensing combining the IPDA/DIAL lidar system in the German Aerospace Center (DLR) with the new UCD.

3 Theoretical investigation of the UCD noise sources. Characterize the noise properties of the UCD including the spatial distribution of noise photon and the frequency response of the upconversion module.

Chapter 2

Theory of Frequency Upconversion

Before pivoting to the details of the UCD, some fundamental principles and concepts related to the upconversion technology will be introduced in this chapter. These materials will provide theoretical support for the analysis and discussion in the following chapters. At the beginning of this chapter, a physical model of 2nd order nonlinear optical process along with its mathematical description will be introduced. In the second section, phase matching condition will be explicitly addressed. Since PPLN crystal is the $\chi^{(2)}$ material that is used in this project, its properties and the associated optical processes will be discussed in the last section of this chapter.

As mentioned in Chapter 1, the fundamental theory handling the 2nd order nonlinear process has been developed since the 1960s. Instead of showing the details of derivations [46–48], only some important equations and conclusions will be presented directly for the convenience of further discussion. Additionally, the scope of 2nd order nonlinear optics is too large to be covered entirely, hence only the theory associated with the frequency upconversion will be emphasized here.

2.1 Theory of 2nd order Nonlinear Optical Process

In comparison with the common linear optical phenomena such as reflection, refraction and absorption, a nonlinear optical process is usually too weak to be observed in daily life. Most of the time, the nonlinear effect becomes observable only under the condition of high-intensity electromagnetic field. Mathematically, the linear response is just a first-order approximation of the interaction between the electromagnetic field and the material, and the nonlinear process is usually handled by the perturbation theory since the interaction is much weaker than the linear one.

2.1.1 2nd order Nonlinear Susceptibility

Generally, it is unnecessary to study the response of each atom in the material individually. Instead, the susceptibility $\chi^{(i)}$ is used to bridge the response of material and the optical field as shown by equation 2.1.

$$\tilde{P}(t) = \epsilon_0[\chi^{(1)}E(t) + \chi^{(2)}E^2(t) + \chi^{(3)}E^3(t) + \cdots] \tag{2.1a}$$

$$\equiv \tilde{P}^{(1)}(t) + \tilde{P}^{(2)}(t) + \tilde{P}^{(3)}(t) + \cdots, \tag{2.1b}$$

where ϵ_0 is the permittivity of free space. $\tilde{P}(t)$ is the polarization and $E(t)$ is the electric field. $\chi^{(1)}$ is the linear susceptibility that determines the refractive index, absorption and birefringence property of the material. $\chi^{(2)}$ is known as the 2nd order nonlinear susceptibility, which is of great significance in frequency upconversion. $\chi^{(2)}$ is a 3rd-rank tensor having 54 elements. For the case of three-wave mixing, a total of 6 tensors should be considered resulting in 324 elements in general. These

324 elements are not always independent. With several kinds of symmetry considerations, $\chi^{(2)}_{ijk}$ can be replaced by a 2nd-rank tensor d_{il} with only 10 independent elements as shown by equation 2.2.

$$d_{il} = \begin{bmatrix} d_{11} & d_{12} & d_{13} & d_{14} & d_{15} & d_{16} \\ d_{16} & d_{22} & d_{23} & d_{34} & d_{14} & d_{12} \\ d_{15} & d_{24} & d_{33} & d_{23} & d_{13} & d_{14} \end{bmatrix}. \tag{2.2}$$

For a specific nonlinear crystal with a certain symmetry of its crystal lattice, the number of independent elements can be further reduced. For example, the $LiNbO_3$ crystal belongs to the point group of class 3m, and its d_{il} has only 3 independent elements as:

$$d_{il} = \begin{bmatrix} 0 & 0 & 0 & 0 & d_{31} & -d_{22} \\ -d_{22} & d_{22} & 0 & d_{31} & 0 & 0 \\ d_{31} & d_{31} & d_{33} & 0 & 0 & 0 \end{bmatrix}. \tag{2.3}$$

In practice, the propagation directions and the polarization states of the optical fields are forced to fulfil the phase matching condition in order to maximize the efficiency. Thus, d_{il} with a limited number of independent elements can be further simplified as a scalar value of d_{eff}. For example, when the QPM condition is used for the PPLN-based upconversion, only d_{33} in equation 2.3 (25 pm/V) can contribute to the nonlinear interaction.

2.1.2 Coupled-Wave Equations for Sum and Difference Frequency Generation

Different theories can be used to describe the 2nd order nonlinear process mathematically. For example, the quantum field theory can draw a full picture of the nonlinear interaction, and it even becomes the only option when the quantum effect cannot be neglected such as the SPDC process. Pedersen et al. from our group developed a method for modelling the nonlinear interaction of two arbitrary fields inside the nonlinear crystal [49], wherein the absorption of the crystal and the spatial walk-off are considered. This model turns out to be a simple method for handling the nonlinear interaction of two Gaussian beams [43]. In this thesis, the coupled-wave equations derived from the Maxwell equations are used in most of the calculations since plane-wave interaction is a good approximation for most of the experiments performed in this Ph.D. project.

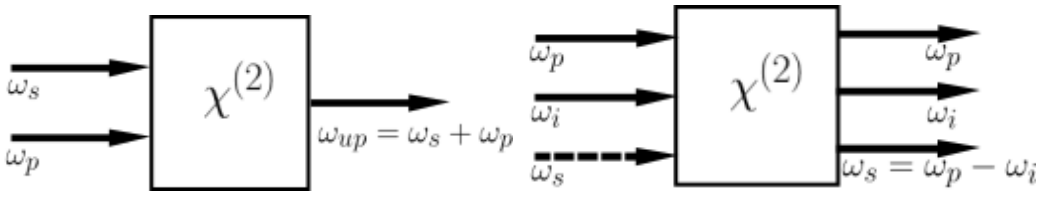

(a) (b)

FIGURE 2.1: Frequency diagrams for (a) sum and (b) difference frequency generation.

Figure 2.1a and figure 2.1b shows the SFG and DFG processes, respectively. In order to make the equations compatible with the following experiments, the subscripts

for each parameter are assigned based on the experimental conditions: up, p, s, i represent upconversion, pump, infrared signal and idler, respectively. These subscripts will be used in this thesis consistently.

The coupled-wave equations for SFG are:

$$\frac{dE_s}{dz} = K_{su} g(z) E_{up} e^{-i\Delta k_{up} z} \tag{2.4a}$$

$$\frac{dE_{up}}{dz} = K_{up} g(z) E_s e^{i\Delta k_{up} z}, \tag{2.4b}$$

where

$$K_{su} = \frac{2iw_s d_{eff}}{n_s c} E_p^*, K_{up} = \frac{2iw_{up} d_{eff}}{n_{up} c} E_p \tag{2.4c}$$

$$\Delta k_{up} = k_p + k_s - k_{up}. \tag{2.4d}$$

The coupled-wave equations for DFG are

$$\frac{dE_s}{dz} = K_{sd} g(z) E_i^* e^{i\Delta k_d z} \tag{2.5a}$$

$$\frac{dE_i}{dz} = K_{id} g(z) E_s^* e^{i\Delta k_d z}, \tag{2.5b}$$

where

$$K_{sd} = \frac{2iw_s d_{eff}}{n_s c} E_p, K_{id} = \frac{2iw_i d_{eff}}{n_i c} E_p \tag{2.5c}$$

$$\Delta k_d = k_p - k_s - k_i, \tag{2.5d}$$

where $g(z)$ is defined as a crystal structure function, which is used to describe the optic axis of the crystal at position z. For example, $g(z) \equiv 1$ for the non-poled crystal. The exact form of $g(z)$ for the PPLN crystal will be discussed in detail in the following section. k_j is the wavenumber defined as $k_j = 2\pi/\lambda_j \cdot n_j$, where n_j is the refractive index, which can be calculated by the Sellmeier equation when λ_j and temperature T are assigned.

Before using equations 2.4 and 2.5 for the further calculation, the following 5 points should be emphasized.

- **Slowly varying amplitude approximation**
  Equations 2.4 and 2.5 are the approximate results of Maxwell's equations including the nonlinear response of the material. The slowly varying amplitude approximation is one of the most important postulations requiring $|d^2E/dz^2| \ll |kdE/dz|$. Therefore, these equations cannot handle the nonlinear effect when an ultra-short pulse is involved.

- **Pump non-depletion**
  It is a three-wave mixing process for both SFG and DFG processes. Hence the differential equation of E_p should also be included in principle. But for the experiments demonstrated in this thesis, the pump field is much stronger than the other ones, and its variation throughout the crystal can be neglected. Therefore, E_p is treated as constant during the interaction.

- **Energy conservation**
  SFG and DFG are parametric processes, i.e. without energy exchange between the optical field and the material. Energy is conserved among these three optical fields: $\hbar\omega_{up} = \hbar\omega_i + \hbar\omega_s$. Moreover, Manley–Rowe relations are also maintained: the rates of photon number change in each of the fields are equal.

- **Momentum conservation**
  The momentum is not necessarily conserved among these three mixing fields. When an unpoled material is used, maximal conversion efficiency can be obtained when the momentum is conserved among three photons: $\hbar\vec{k}_{up} = \hbar\vec{k}_p + \hbar\vec{k}_s$, which is also known as the phase matching condition. In contrast, the impulse-momentum theory should be used when the momentum among the photons is non-conserved. The additional momentum gain (or loss) among the photons are from the impulse applied by the nonlinear material, i.e. the material experiences a force applied by the optical fields.

- **Gaussian beam consideration**
  Equations 2.4 and 2.5 handle the nonlinear processes in the temporal and spatial frequency domain. Therefore, the interaction between plane waves can be solved directly. However, the pump field in the experiment is a Gaussian beam, which should be converted into the spatial frequency domain before using equations 2.4 and 2.5 for the calculation. But for most cases in this thesis, the Rayleigh length of the pump beam is larger than the crystal length. Thus, the Gaussian beam in those cases can still be approximated as a plane wave. It also means the conservation of transverse momentum, thus $\Delta\vec{k}$ becomes a scalar.

2.1.3 SPDC and Vacuum Fluctuation

Figure 2.2 shows the scheme of the SPDC process, which is similar to the DFG process as shown by figure 2.1b except that there is no signal/idler input. Equations 2.5 cannot be used for the calculation of the SPDC process directly since only a trivial solution $E_s(0 < z < L) \equiv 0$ can be obtained considering the initial conditions of $E_s(z = 0) = 0$ and $E_i(z = 0) = 0$. Apparently, this trivial solution is inconsis-

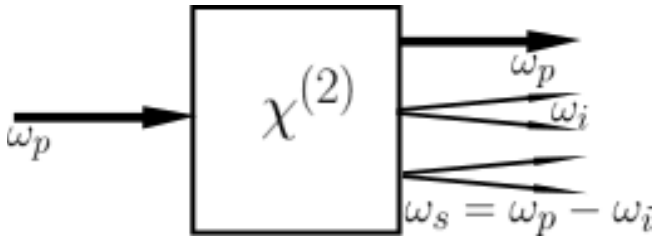

FIGURE 2.2: Frequency diagram of the SPDC process

tent with the experimental result due to the fundamental limitation of the classical electrodynamics.

SPDC process was rigorously modelled by Tang based on the quantum field theory [12]. In this thesis, the SPDC process is described semi-classically by combining equations 2.5 with the quantum effect of vacuum fluctuation.

In the k space of the idler field, the mode density with one single polarization state is $V/(2\pi)^3$, the number of modes dN_i in the k space between ψ and $\psi + d\psi$

with the magnitude between k_i and $k_i + dk_i$ is

$$dN_i = \frac{V}{(2\pi)^3} k_i^2 d\Omega dk_i = \frac{V}{(2\pi)^3} k_i^2 dk_i 2\pi\psi d\psi. \tag{2.6}$$

Assuming each mode has only one photon, the intensity I_{i0} is:

$$I_{i0} = \frac{c\hbar w_i dN_i}{V n_i} = \frac{c\hbar w_i k_i^2 \psi dk_i d\psi}{(2\pi)^2 n_i}. \tag{2.7}$$

Afterwards, I_{i0} is used as the initial condition for equations 2.5. Following the same procedures, the power of SPDC can be calculated (Byer and Harris [11]) as:

$$P_s = (\beta L P_p/|b|)\pi\theta^2,\ \beta = \frac{2v_s^4 v_i d_{15}^2 \hbar n_s}{(2\pi)^2 \epsilon_0^3 c^5 n_i n_p},\ b = \left.\frac{\partial k_s}{\partial \omega_s}\right|_{\omega_s=\omega_{sc}} - \left.\frac{\partial k_{up}}{\partial \omega_{up}}\right|_{\omega_{up}=\omega_{upc}}. \tag{2.8}$$

This result was confirmed by the experiment done by Pearson et al. [50]. In Chapter 4 of this thesis, the calculation of SPDC intensity based on the vacuum fluctuation is performed in order to evaluate the intensity of USPDC noise as a function of parameters such as pump power.

2.2 Phase Matching Condition

In the community of nonlinear optics, phase matching condition is one of the essential concepts, which has been discussed repeatedly. The formula of phase matching is elegant, and the principle of momentum conservation behind the formula is also crucial. Especially for experimental physicists, the maximal conversion efficiency can only be achieved with the condition of phase matching (or quasi-phase matching). Phase matching condition is usually met by temperature or angular tuning of birefringence of the crystal. The classification of phase matching type and its relation with the properties of the material were discussed by Midwinter and Warner [51] in 1965.

2.2.1 Phase Matching Condition and Upconversion Efficiency

When the unpoled $\chi^{(2)}$ material is used for upconversion, $g(z) \equiv 1$. With the initial condition of $E_z = 0$, equation 2.4a can be solved as:

$$I_{up}(L) = I_s(0)\frac{n_{up}}{n_s}|K_{up}|^2 L^2 sinc^2(\gamma L), \tag{2.9a}$$

where

$$\gamma = [-K_{su}K_{up} + (\Delta k_{up}/2)^2]^{1/2}. \tag{2.9b}$$

The upconversion efficiency is

$$\eta_{up} = \frac{I_{up}(L)/\hbar\omega_{up}}{I_s(L)/\hbar\omega_s} = \frac{2\omega_{up}\omega_s d_{eff}^2 L^2 I_p}{n_p n_s n_{up} c^3 \epsilon_0} sinc^2(\gamma L). \tag{2.10}$$

In the case of phase matching $\Delta k_{up} = 0$, the upconversion efficiency becomes

$$\eta_{up} = sin^2(\sqrt{\frac{P_p}{P_{max}}}\frac{\pi}{2}), \tag{2.11a}$$

where

$$P_{max} = \frac{\pi^2 n_p n_s n_{up} c^3 \epsilon_0 A}{8\omega_{up}\omega_s d_{eff}^2 L^2}. \tag{2.11b}$$

Equations 2.11 is used for the calculation of upconversion efficiency when signal depletion cannot be neglected. Figure 2.3a shows the upconversion efficiency with different pump power. Theoretically, a unity upconversion efficiency η_{up} is obtained when $P_p = P_{max}$, and it starts decreasing when P_p becomes larger than P_{max}, which indicates that the upconverted photons start downconverting back to the IR signal.

When the upconversion efficiency is low ($P_p << P_{max}$) and the depletion of the signal can be neglected,

$$\eta_{up} \approx \frac{2\omega_{up}\omega_s d_{eff}^2 L^2 I_p}{n_p n_s n_{up} c^3 \epsilon_0} sinc^2(\Delta k_{up} L/2). \tag{2.12}$$

According to equation 2.12, the upconversion efficiency is proportional to the square of crystal length L^2 times the intensity of the pump field I_p. These two parameters can be specified in the design of the UCD. Figure 2.3b shows the normalized up-

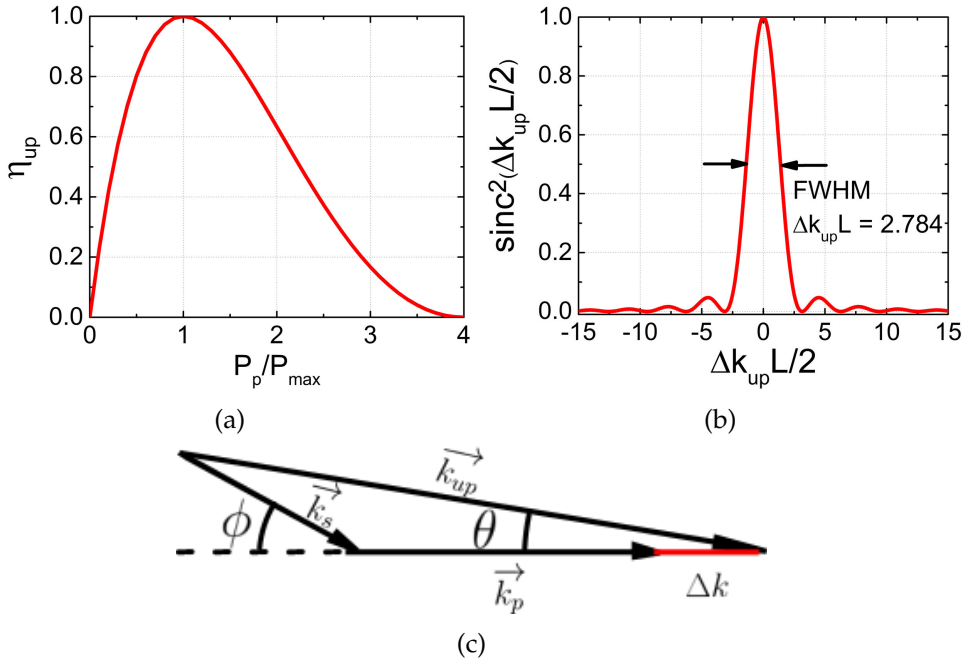

FIGURE 2.3: (a) Upconversion efficiency as a function of normalized pump power, (b) sinc^2 function of the phase mismatch and (c) wave vectors of the three mixing fields.

conversion efficiency as a function of phase mismatch. The maximal η_{up} is expected when the phase matching condition $\Delta k_{up} = 0$ is fulfilled. The full width at half maximum (FWHM) is specified as a function of phase mismatch Δk_{up} and crystal length L. Figure 2.3c illustrates the wave vectors of the three mixing fields with the non-collinear phase mismatching condition. With small angle approximation of $\phi \ll 1$,

phase mismatch Δk_{up} can be approximated as:

$$\Delta k_{up} = k_{up}\cos(\theta) - k_s\cos(\phi) - k_p \tag{2.13a}$$
$$\approx k_{up} - k_s - k_p + k_s/2(1 - k_s/k_{up})\theta^2, \tag{2.13b}$$

where

$$k_s\phi = k_{up}\theta. \tag{2.13c}$$

When $\Delta k_{up} \neq 0$, the coherence length can be defined as

$$L_c = \frac{2\pi}{\Delta k_{up}}. \tag{2.14}$$

For the upconversion process with the condition of phase mismatching $\Delta k_{up} \neq 0$, the energy in each fields exchanges with others periodically along the propagation direction, and the period is $2L_c$. The maximum upconversion efficiency is obtained at distance of L_c. Afterwards, the energy stored in the upconverted field flows back to the pump and the IR signal fields.

For the upconversion process with the phase matching condition of $\Delta k_{up}(\lambda_{sc}, \phi_c, T_c) = 0$, the acceptance parameters of the upconversion are:

$$\Delta\lambda_s = \Delta k_{FWHM} \Big/ \left.\frac{\partial \Delta k_{up}}{\partial \lambda_s}\right|_{\lambda_s=\lambda_{sc}} \tag{2.15a}$$
$$\Delta\phi = \Delta k_{FWHM} \Big/ \left.\frac{\partial \Delta k_{up}}{\partial \phi}\right|_{\phi=\phi_c} \tag{2.15b}$$
$$\Delta T = \Delta k_{FWHM} \Big/ \left.\frac{\partial \Delta k_{up}}{\partial T}\right|_{T=T_c}, \tag{2.15c}$$

where $\Delta k_{FWHM} = 2.784/L$. $\Delta\lambda_s$, $\Delta\phi$ and ΔT are the acceptance bandwidth, angle and temperature, respectively. These three parameters can be calculated numerically when the Sellmeier equation for the material is specified. These three acceptance parameters are widely used in both theoretical and experimental study of the UCD. For example, the acceptance bandwidth $\Delta\lambda_s$ decides the spectral range of detection, the acceptance angle $\Delta\phi$ decides the field of view of the detector and the acceptance temperature ΔT is the maximal tolerance of temperature detune.

2.2.2 Quasi-Phase Matching

Angular and temperature tuning are two most common methods of achieving phase matching condition when an unpoled birefringent crystal is used for the upconversion. However, this scheme has the following disadvantages: 1) Angular and temperature tuning have a limited spectral range, i.e. the phase matching condition cannot be achieved for some arbitrary combinations of pump and signal wavelengths. 2) The d_{eff} in this scheme is much smaller than the diagonal terms d_{33}, and smaller d_{eff} indicates lower upconversion efficiency. For example, the d_{eff} is usually smaller than 5 pm/V when an unpoled $LiNbO_3$ crystal is used for the upconversion, but d_{33} of $LiNbO_3$ is 25 pm/V. 3) One of the three mixing fields has a different polarization state than the others, the spatial walk-off (for the critical phase matching) between the extraordinary and the ordinary beams can reduce the efficiency significantly.

Quasi-phase matching (QPM) is one of the technologies that can overcome the limitations that mentioned above. This technique was first proposed by Armstrong et al. [5]. More detailed calculations were given in other studies [52–54]. At that time, the technologies such as periodically poling and orientation patterning were not invented, hence QPM could only be achieved by using the stack of plates experimentally, which is shown in figure 1.2a. Apparently, it was not ideal considering the relatively high transmission losses during the propagation.

As shown by the cyan line in figure 2.4, the energy in the upconverted field changes periodically. In the first coherence length L_c, the energy in the upconverted field builds up, but the energy flows back to the signal and the pump fields due to the phase destruction in the second L_c. However, the energy can continue building

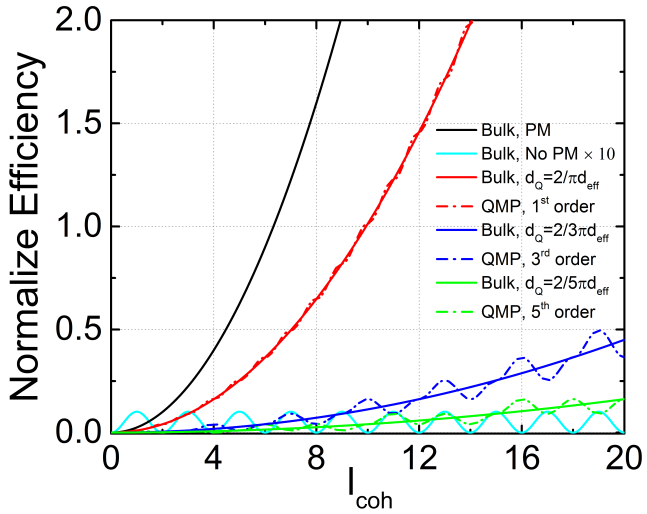

FIGURE 2.4: Normalized upconversion efficiency at different positions with the condition of normal phase matching, phase mismatching, 1_{st} , 3_{rd} and 5_{th} order of QPM.

up if the phase of polarization is shifted by π after each coherence distance L_c, which is known as the QPM. The black line in figure 2.4 is the conversion efficiency with the usual phase matching condition, which is larger than the one given by the QPM (red line). But in practice, the larger term of the nonlinear susceptibility can be accessed through QPM, which always leads to a higher conversion efficiency in comparison with the angular-tuned phase matching. Comparing the PPLN crystal and the unpoled $LiNbO_3$ crystal, the effective nonlinear coefficient of QPM $d_Q = 2/\pi d_{33} \approx 16\,\mathrm{pm/V}$, which is around 3.6 times larger than that of angular-tuned phase matching $d_{eff} \approx d_{31} = 4.4\,\mathrm{pm/V}$. Assuming all the other parameters are the same, the conversion efficiency is improved by a factor of 14 by using a PPLN crystal instead of an unpoled $LiNbO_3$.

Equations 2.4 and 2.5 can still be used for the calculation of QPM-based frequency conversion processes. In this case, the crystal structure function $g(z)$ becomes

$$g(z) = \begin{cases} 1, \text{ odd domain} \\ \text{-1, even domain.} \end{cases} \tag{2.16}$$

The red, blue and green dash lines in figure 2.4 are the numerical results of equations 2.4 with 1st, 3rd and 5th order QPM. The conversion efficiency becomes larger with the increase of propagation distance, but the periodic fluctuation due to the phase mismatching is still visible. Equations 2.4 can be simplified by replacing d_{eff} and

Δk_{up} with d_Q and Δk_Q, respectively.

$$d_Q = d_{eff} G_m \tag{2.17a}$$
$$\Delta k_Q = k_{up} - k_s - k_p - k_m, \tag{2.17b}$$

where

$$k_m = \frac{2\pi}{\Lambda} m,\ G_m = \frac{2}{m\pi} sin(m\pi/2),\ m = 1, 2, 3 \ldots. \tag{2.17c}$$

The red, blue and green solid lines are the results of simplified equations 2.4. These lines are the first order approximation of the dash lines. Therefore, they have no fluctuation at all. The 1st order QPM is preferred in frequency conversion since it can provide the highest efficiency compared with the other higher orders. However, due to the limitation of fabrication technology, the poling period cannot be made unlimitedly small. For example, the fabrication of PPLN with a poling period smaller than 5 µm can be very challenging. Therefore, a higher-order QPM is used at the compromise of the conversion efficiency when the 1st order QPM is not possible.

2.2.3 Super-Phase Matching

During the operation of upconversion detection, a pump field with high intensity always leads to a phase mismatched SPDC process, and the photon generated by the SPDC process can be further upconverted. These two steps together are defined as the USPDC process. Its Feynman diagram and spectral scheme are shown in figure 1.4b and figure 2.5, respectively.

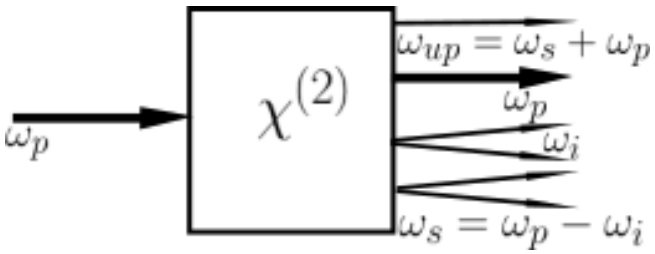

FIGURE 2.5: Frequency diagram of the USPDC process.

Generally, the system is phase-matched for the upconversion process in order to optimize the upconversion efficiency. Thus, the SPDC process is usually phase mismatched, which results in a low intensity of USPDC. For the applications of OPO and OPA system, the USPDC process can be neglected. But for a short-wavelength-pumped upconversion detection system applied particularly to measure weak IR signals, the USPDC process can be one of the primary noise sources. Therefore, a thorough investigation of USPDC process is necessary in order to comprehend the noise properties of the detector completely.

Under special conditions, the phase matching conditions for both upconversion and SPDC processes can be fulfilled simultaneously, which is known as super-phase matching. Andrews et al. first reported this two-step nonlinear interaction in ammonium dihydrogen phosphate pumping with a 530 nm laser [55]: for the SPDC process: $\omega_p^e = \omega_s^o + \omega_i^e$, for the upconversion process: $\omega_p^o + \omega_s^o = \omega_{up}^e$. The superscripts o, e represent the ordinary and extraordinary polarization, respectively. Similar demonstrations can be found in the literature [56–58]. This technology provides a unique way of upconversion without any direct IR input. However, the

SPDC and the upconversion processes are not entangled strictly since the pump (or the signal) fields in these experiments had different polarization states in these two parametric steps. Theoretically, the super-phase matching condition with the same

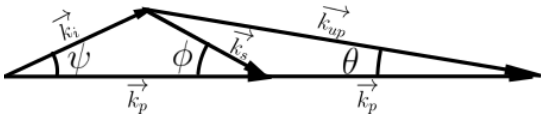

$$\vec{k}_{up}(\lambda_{up},\theta) - \vec{k}_s(\lambda_s,\phi) - \vec{k}_p = 0 \quad (2.18a)$$
$$\vec{k}_p - \vec{k}_s(\lambda_s,\phi) - \vec{k}_i(\lambda_i,\psi) = 0 \quad (2.18b)$$
$$\frac{1}{\lambda_{up}} = \frac{1}{\lambda_s} + \frac{1}{\lambda_p}, \frac{1}{\lambda_s} = \frac{1}{\lambda_p} - \frac{1}{\lambda_i}. \quad (2.18c)$$

FIGURE 2.6: wave vectors for the super-phase-matched USPDC process.

pump and signal polarization state can be achieved. According to the principle of momentum and energy conservations, the system fulfils the super-phase matching condition has relations of equations 2.18, and its wave vector diagram is shown in figure 2.6. Equations 2.18 contains 6 variables and 6 restrictions when the pump field $\vec{k}_p$ is fixed. Generally, it can be solved mathematically.

In practice, $\vec{k}_p$ cannot be chosen arbitrarily since it is restricted by the dispersion of the material. Figure 2.7 shows the solutions of equations 2.18 when a BBO crystal is used. The polarization states of each field are: SPDC process: $\omega_p^e = \omega_s^o + \omega_i^o$, up-conversion process: $\omega_p^e + \omega_s^o = \omega_{up}^e$. The pump and the signal fields have the same

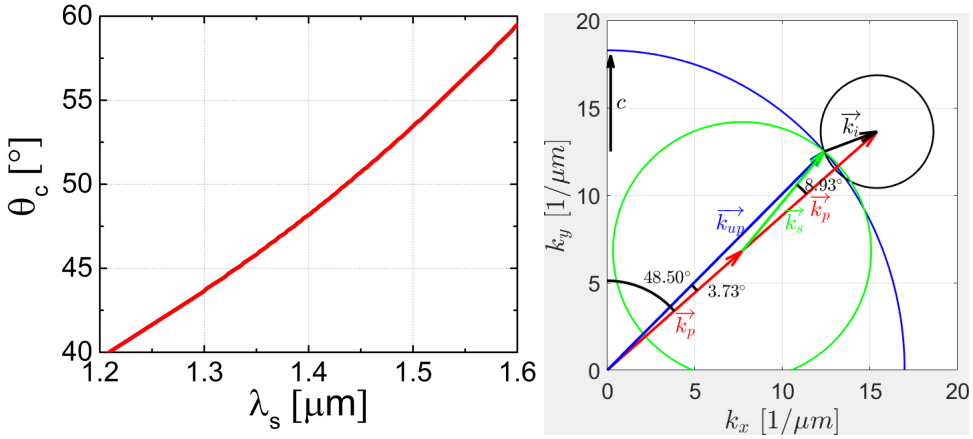

(a) (b)

FIGURE 2.7: (a) Angle θ_c (between the direction of $\vec{k}_p$ and the optic axis c) as a function of the signal wavelength λ_s, (b) an example solution with wave vectors plotted in the crystal coordinate system. The Sellmeier equation at room temperature [59] is used for the refractive index calculation.

polarization state in those two processes. Figure 2.7a shows the relation between angle θ_c and the signal wavelength λ_s when the wavelength of the pump is fixed $\lambda_p = 532\,\text{nm}$. Figure 2.7b shows the wave vectors of one specific solution when $\theta_c = 48.5\,°$: $\vec{k}_p$ is fixed since $\theta_c = 48.5\,°$; the point of intersection between the black circle and the blue ellipsoid represents the solution of the SPDC process: $\vec{k}_s + \vec{k}_i = \vec{k}_p$; the point of intersection between the green circle and the blue ellipsoid represents the solution of the upconversion process: $\vec{k}_{up} - \vec{k}_s = \vec{k}_p$. Therefore, when two points

merge into one (i.e. the black, green circles and the blue ellipsoid has one common point), super-phase matching condition is met.

2.3 Periodically Poled $LiNbO_3$

As the matrix of PPLN, $LiNbO_3$ crystal was first synthesized in a single crystal form at Bell Laboratories [60]. Afterwards, it became widely used in various optical and electrical applications benefiting from its large pyroelectric, piezoelectric, electro-optic and photoelastic coefficients. Meanwhile, the potential of $LiNbO_3$ for the application of frequency conversion was not fully explored until its optical damage threshold was significantly improved by MgO doping [61]. As shown in the last section, the largest element of nonlinear susceptibility d_{33} was not utilized until the invention of PPLN. Since bulk PPLN is the nonlinear material used in this project, it is necessary to briefly introduce its fabrication procedure and some of its important properties.

2.3.1 Fabrication of PPLN and the Poling Errors

$LiNbO_3$ is a kind of ferroelectric crystal whose electrical polarization can be controlled by applying an electric field externally. Therefore, it is possible to have a periodically poled structure by applying a periodically changed electric field. Barry et al. specified the necessary procedures for the fabrication of PPLN [62], which is summarized in figure 2.8.

FIGURE 2.8: Four main steps for bulk PPLN fabrication.

The poling error is unavoidable due to the practical limitation of the poling technique. The position of the electrode can be precisely controlled by photolithography, which induces very little error. However, the process of domain reversal (step 3 in figure 2.8) is strongly affected by the properties of the wafer and the poling conditions. Thus, the errors are mainly created during this step. It becomes extremely challenging to fabricate a PPLN crystal with a small poling period and a large thickness [63]. Commercially available PPLN crystals with $\Lambda < 5\,\mu m$ and thickness $d > 5\,mm$ are very rare.

A cornerstone addressing the effect of boundary error on the conversion efficiency in the QPM devices was placed by Fejer et al. in 1992 [64]. In their paper, different types of error (missing reversals, random period error, random duty cycle error and linear taper of period) were discussed in detail. These errors all affect the frequency conversion to some degree, but in this thesis, only the random duty cycle (RDC) error will be considered because it is believed to be the main reason for the efficiency degradation and the noise generation. The effects caused by the other errors can be neglected. In particular, the random period error mainly exists in the QPM devices made of a stack of slabs. For the PPLN structure, the poling period is precisely defined by the electrode pattern, the random period error can be assumed zero. The missing reversal (or domain merging) and the offset error can be treated as a reduction of crystal length. In addition, the microscopic image of the PPLN crystal

confirms that the number of the missing domain reversal is much smaller than the total number of domains in the crystal.

The comparison between the perfect structure (1) and the one with the RDC error (2, 3) is shown in figure 2.9. For the PPLN crystal with the RDC error, the boundary

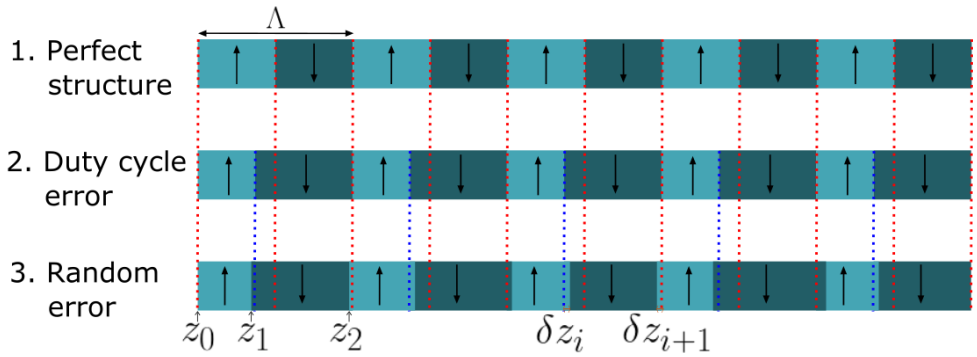

FIGURE 2.9: PPLN poling structure with and without RDC error.

of the domain is labelled as z_i. The RDC error contains two parts: first, the duty cycle of the structure is not perfectly 50/50. In the process of fabrication, the 50/50 duty cycle is not always the top optimization item, and small duty cycle is chosen intentionally in order to avoid critical damage such as domain merging in large scale. Second, the final boundary position has a random error, δz_i, which is assumed to follow a Gaussian distribution. At the beginning of the poling process, the region close to the electrode (top surface in figure 2.8) is reversed at first, then reversing goes deeper until reaching the bottom. The growing process is similar to a random walk, and the poling error in the region close to the top surface is smaller than that close to the bottom.

2.3.2 Incidental Parametric Processes in PPLN

The RDC error not only degrades the conversion efficiency but also introduces incidental parametric processes. Especially when a high-intensity field is applied in the PPLN crystal, the intensity of parametric processes can be considerably high even though it may not be phase matched. Taking the short-wavelength-pumped upconversion detection system as an example, the typical noise count due to the USPDC process is at the level of 1×10^5/s, which limits the NEP of the detector strongly. Theoretically, the type of incidental parametric process in PPLN is unlimited, because photons with different wavelengths can be either upconverted, frequency doubled or downconverted. Meanwhile, a parametric process with multiple steps is also possible, which makes the process even more complicated. However, it is unnecessary and impractical to analyze all these parametric processes individually since most of these processes are extremely weak. Only the processes that can potentially affect the upconversion detection will be discussed here.

- **SPDC**
  The SPDC process in an unpoled crystal was discussed in section 2.1.3 already. The power of phase-matched SPDC is also given by equation 2.8. The pump-induced SPDC in PPLN crystal has the same Feynman diagram as shown in figure 1.4a, but it is phase mismatched. Additionally, it has a much stronger intensity and broader spectrum in comparison with the phase mismatched SPDC in the unpoled crystal. This high-intensity, broadband SPDC is caused by the

pedestal effect due to the existence of RDC error in the PPLN crystal [24]. If the poling structure of PPLN is defined, the intensity of SPDC can be calculated using equations 2.5 and 2.7 together.

- **USPDC**
  Following the SPDC process, the downconverted photon can be further upconverted as shown in figure 1.4b. Since the SPDC is relatively broadbanded, only the SPDC photons within the acceptance bandwidth of the upconversion can be upconverted efficiently with the QPM condition. It is worth pointing out that the USPDC photon has a similar wavelength of the upconverted signal. Thus, it is difficult to remove it by using spectral filters.

- **SHG**
  The Feynman diagram of the SHG process is shown in figure 2.10a. Similar to the SPDC process in the PPLN crystal, the SHG process is also phase mismatched. Its bandwidth is decided by the linewidth of the pump field. Usually, a laser with a narrow linewidth is used as the pump. Thus, the bandwidth of the SHG is very narrow as well. In addition, according to the principle of the SHG, the intensity of the SHG is proportional to the square of pump intensity. Therefore, the spectral brightness of the SHG is much stronger than that of the SPDC. The actual intensity of the SHG is also dependent on the specific RDC error of the PPLN. In general, a larger error leads to a higher SHG intensity. A typical power of the SHG is between the µW and the mW level when a 25-mm long PPLN crystal is pumped by a $\sim$ 150 W 1064 nm laser.

- **SHG-SPDC**
  Similar to the USPDC process, SHG-SPDC also contains two steps: SHG process triggers the SPDC process as shown in figure 2.10b. The intensity of the SHG field is very weak compared with the pump field, therefore, the intensity of the phase mismatched SPDC photons due to the SHG field is also very weak. However, some particular SPDC process can fulfil the QPM condition, which leads to a spike in its SPDC spectrum.

Essentially, only the single step process (upconversion, SPDC and SHG), and the two-step process (USPDC and SHG-SPDC) with one step fulfilling the QPM condition should be considered. From the perspective of upconversion detector, the USPDC and the SHG-SPDC should be considered only when a short-wavelength pump is used. More theoretical and experimental investigations of these two processes will be discussed in detail in Chapter 4.

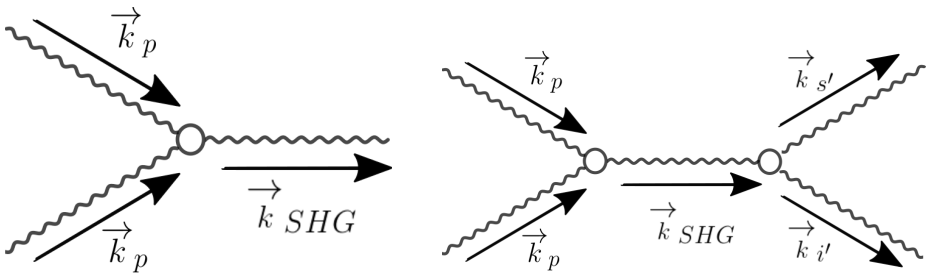

(a) (b)

FIGURE 2.10: Feynman diagrams for (a) SHG and (b) SHG-SPDC processes.

Chapter 3

Detector Configuration

This chapter focuses on the design and the characterization of an UCD for atmospheric lidar application. Ideally, a detector with high detection efficiency, low background noise and short response time is preferred. But in reality, these parameters are limited by either the properties of materials or its basic working principle. Different compromises have to be made in order to achieve better performance for a specific application. Based on the requirements of atmospheric lidar measurements, a UCD based on a short-wavelength pump with intracavity enhancement is chosen. In the first section of this chapter, the reason for choosing this specific design will be explained in detail. The second section is about the characterization of UCD. The procedures and result of measuring the intracavity-pump power, upconversion efficiency and background noise will be introduced sequentially. Afterwards, the UCD is pre-tested by measuring a weak IR signal. In the last section, the signal-to-noise of the system is analyzed.

3.1 Short-wavelength-pumped UCD with Intracavity Enhancement

A former member of our research group, Lasse Høgstedt, designed and built our first UCD for atmospheric lidar application [45]. His measurement results confirmed that the UCD could be applied for weak NIR signal detection, and it has a great potential for further improvement. One of the goals of this Ph.D. project is to continue his research work: design and build the 2nd generation of UCD and continue using it for atmospheric gas sensing.

3.1.1 UCD Design

The performance of the first UCD did not outperform the conventional InGaAs based detectors in the experiment of atmospheric CO_2 sensing. Two main reasons were identified: first, the upconversion efficiency was relatively low due to the low pump power. Second, the small étendue of the detector strongly limited its ability for IR signal collection. Therefore, during the design process of the 2nd generation UCD, a lot of effort is dedicated to the improvement of upconversion efficiency and to the enlargement of étendue.

Pumping with a high-intensity optical field is one of the most important methods to increase the upconversion efficiency, and it is usually achieved by pumping with short optical pulses, pumping in a waveguide or pumping inside a high-Q cavity. However, only the intracavity pumping has the ability of continuous measurement with a relatively large étendue. Therefore, the 2nd generation UCD is still based on

the scheme of intracavity enhancement but applies a ring cavity instead of a linear cavity.

In the 1st generation UCD, the USPDC noise was identified as the primary noise source. In principle, it can be fundamentally removed by using a long-wavelength-pumped scheme. However, a short-wavelength (1064 nm) pump is still used in the new UCD for the following four reasons: 1) The long-wavelength-pumped UCDs demonstrated in [25, 26] were all based on waveguide PPLN, high upconversion efficiency can be easily achieved by applying a small pump power ($\sim$ 100 mW). On the contrary, it is impractical to achieve a high-intensity pump for the intracavity-pumped scheme if the wavelength is larger than 2 µm; 2) the upconverted signal given by a long-wavelength-pumped UCD may end up outside the sensitive spectral region of Si based detector; 3) the long-wavelength-pumped UCDs can only work in the region where the IR signal has a shorter wavelength compared to the pump, but for the short-wavelength-pumped UCD, the spectrum of detection is only limited by the transmission region of the nonlinear material [40]. 4) The upconverted spontaneous Raman scattering noise is the primary noise source for the long-wavelength-pumped UCD, its DCR in [25, 26] is at the level of $\sim 1 \times 10^2$/s with a pump power of $\sim$ 100 mW. Since the SRS noise is proportional to the pump power, the DCR is expected to be $\sim 1 \times 10^4$/s with the pump power of $\sim$ 10 W for an intracavity-pumped UCD. In comparison with the DCR of a short-wavelength-pumped UCD, the improvement in noise reduction is limited.

Similar to the 1st generation UCD, a Neodymium-doped Yttrium Vanadate (Nd:YVO_4) crystal is used as the gain material for a solid-state laser at 1064 nm. However, a ring cavity, instead of a linear one, is chosen as the backbone of the UCD. These two kinds of cavity have their own properties. For instance, the laser with a linear cavity is easier to operate compared to the ring-cavity one. The thermal lensing effect can be compensated by changing the length of cavity easily when it is a linear-cavity laser. The 1064 nm laser beam goes through twice of the gain material in the linear cavity, which provides twice of the gain in comparison with the ring-cavity laser if two lasers are pumped under the same conditions. However, the laser with the linear cavity suffers a higher loss because the laser beam refracts and/or reflects twice on each working surface in the linear cavity. For example, one of the main cavity losses in the UCD is due to the AR coating on the PPLN crystal with a reflectivity around 0.6 %, the total loss is around 2.4 % when the laser beam goes through twice for each of the two surfaces in the linear cavity. In contrast, the loss due to bad AR coating on the PPLN crystal becomes 1.2 % for the ring cavity since the laser beam goes through the PPLN crystal just once. The linear cavity suffers an even higher loss if the scattering effect in the PPLN crystal is involved. However, it should be mentioned that the ring cavity has an additional loss due to the isolator consisting of a Faraday rotator (TGG crystal) and a half-wave plate. In addition, a solid-state laser based on the ring cavity has no spatial hole burning effect, which enables a single-longitudinal-mode operation. On the contrary, the multi-longitudinal-mode pump is unavoidable for a UCD with a linear-cavity laser, which can reduce the upconversion efficiency and induce additional beat noise. The details of upconversion with multi-mode pump will be discussed in Chapter 4.

Figure 3.1 and figure 3.2 show the computer-generated photograph and the top view of the UCD, respectively. A fibre-coupled laser diode (808nm-mm-hhl-fiber-10w, λ = 808 nm, core diameter = 200 µm, N.A. = 0.22, $P_{808,max}$ = 10 W, Laser Components) with a maximum 10 W output power at 808 nm is used as the optical pump for the 1064 nm laser. The output from the fibre tip is circularly symmetric, which makes the laser alignment easier compared to using an LD with an elongated

output shape. The laser crystal Nd:YVO_4 is a-cut with 0.5% Nd-doped (3 mm × 3 mm × 8 mm). The laser cavity consists of four mirrors (M1, M2, M3 and M4) with high reflectance (>99.9%) at 1064 nm for the s-polarization state. M1 is a concave

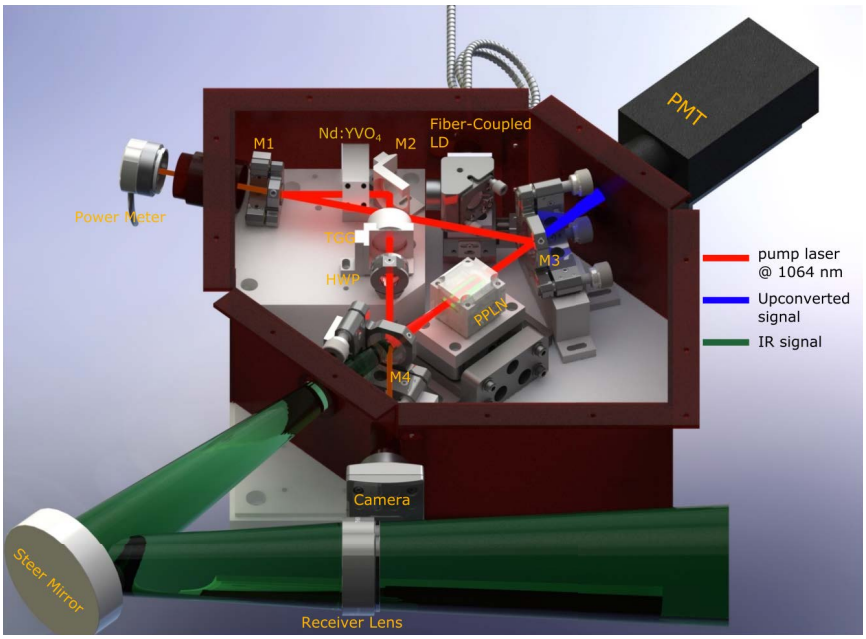

FIGURE 3.1: CG photograph of the 2nd generation UCD. The optical path for the IR signal, the 1064 nm pump and the upconverted signal are assigned with the colour of green, red and blue, respectively.

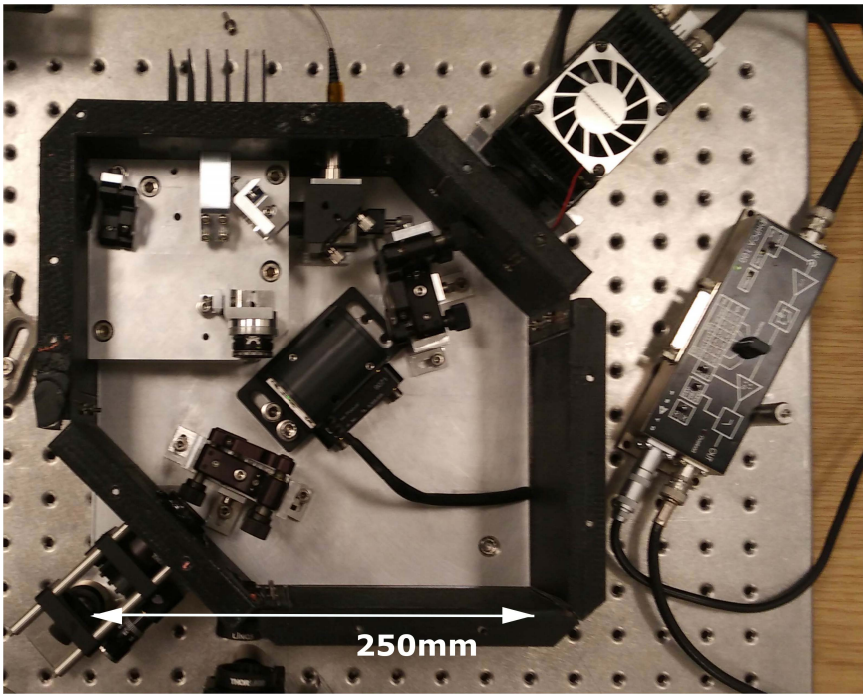

FIGURE 3.2: Top view of the 2nd generation UCD. All components are mounted on a 238 mm×250 mm×25 mm aluminium board. The ambient light is blocked by walls that are 3D printed with black plastic. The aluminium roof is not shown in the picture.

mirror with a radius $R = 350$ mm, M2, M3 and M4 are plane mirrors. M4 and M3 are

used as an IR signal coupling mirror and an upconverted signal decoupler mirror, respectively. The optical isolator between M2 and M4 consists of a terbium gallium garnet crystal (TGG, $L \times R = 10\,\text{mm} \times 2.5\,\text{mm}$) mounted in a ferromagnetic ring and a half wave plate (HWP). Since the mirrors have higher reflectance for the s-polarization state than for the p-polarization state at oblique incidence, the 1064 nm pump is capable of propagation in a single direction. A PPLN oven (PV40, Covesion Ltd) is placed between M3 and M4, which is also the position of the beam waist of the 1064 nm laser. The oven can control the temperature of PPLN crystal in the range of $30 \sim 200\,°\text{C}$ with an error of $\pm 0.1\,°\text{C}$. The 1064 nm beam waist radius ω_0 in the PPLN crystal is $\sim 200\,\mu\text{m}$.

3.1.2 Characterization of PPLN Crystals

Several pieces of PPLN crystals with different lengths and poling structures are used in this project, they were fabricated by HC Photonics Corp. [65] and Covesion Ltd. [66]. Each crystal contains several channels with different poling periods, which are designed for upconversion of IR signals at different spectral ranges. Figure 3.3 shows the temperature T and the acceptance bandwidth $\Delta\lambda_s$ as a function of the wavelength of the IR signal. The Sellmeier equation used for the refractive index calculation is given by [67]. The actual temperature applied in the experiment has an offset ($< 5\,°\text{C}$) compared to the theoretical one, which is mainly due to the inaccuracy of the Sellmeier equation.

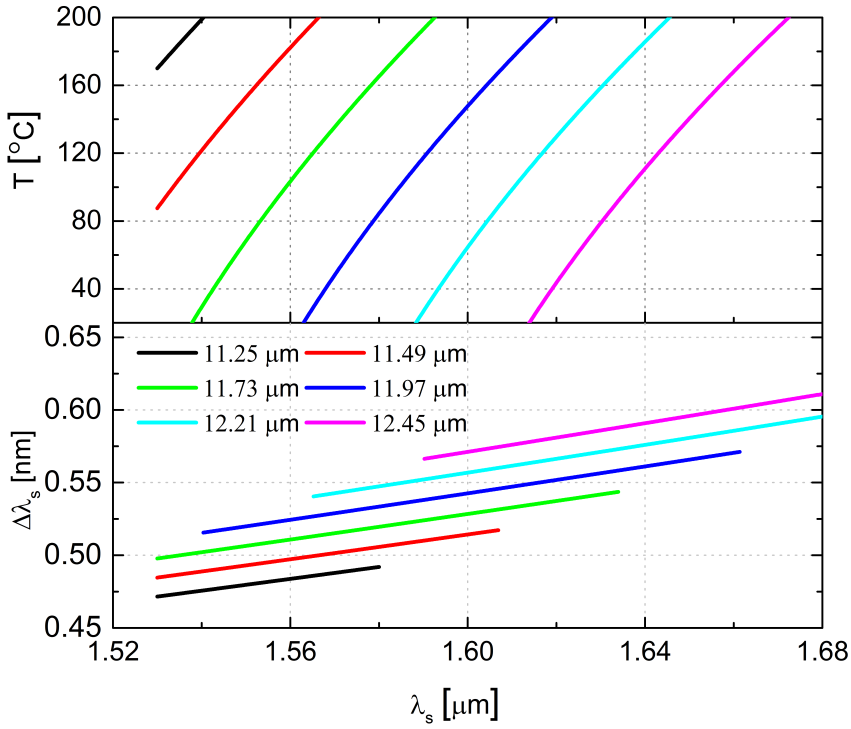

FIGURE 3.3: (a) Temperature T and (b) corresponding acceptance bandwidth $\Delta\lambda_s$ as a function of wavelength λ_s for the collinear QPM condition. The wavelength of pump λ_p = 1064.3 nm. The crystal contains 6 different poling periods as specified by the legend.

As mentioned in Chapter 2, the RDC error of PPLN crystal enhances the unintended parametric processes, which can induce additional noise for upconversion detection. In order to estimate the intensity of the noise, it is important to obtain the position of domain boundaries inside the crystal. Therefore, the surface of the

PPLN crystal that is used in experiments is pictured by a microscope. A portion of the crystal is shown in figure 3.4, from which the position of the boundaries between the adjacent domains can be measured directly. Meanwhile, it is worth pointing out that the boundaries are tapered through the crystal, the actual domain widths are different from the ones that are measured from the picture because only the top of the crystal is imaged. The data presented here is used to estimate the RDC error and the average duty cycle only.

The width of each domain is calculated based on the position of peaks in figure 3.4. The histogram of domain width is shown in figure 3.5. The histogram for the

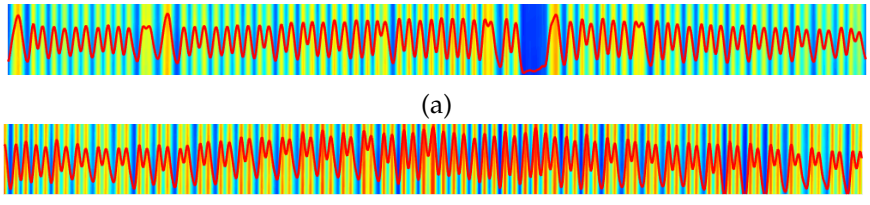

(a)

(b)

FIGURE 3.4: Images of two PPLN crystals from (a) Covesion Ltd. with $\Lambda = 12\,\mu m$ and from (b) HC Photonics Corp. with $\Lambda = 11.97\,\mu m$, respectively. The images are contrast enhanced. The red curves on top of the image are the relative intensity. The peaks of the red curves represent the position of domain boundaries.

HC Photonics crystal has two peaks, which indicates a non-50/50 duty cycle. The average duty cycle and the RDC error of the crystal are calculated by fitting the histogram with a Gaussian distribution. The fitting results are listed in table 3.1.

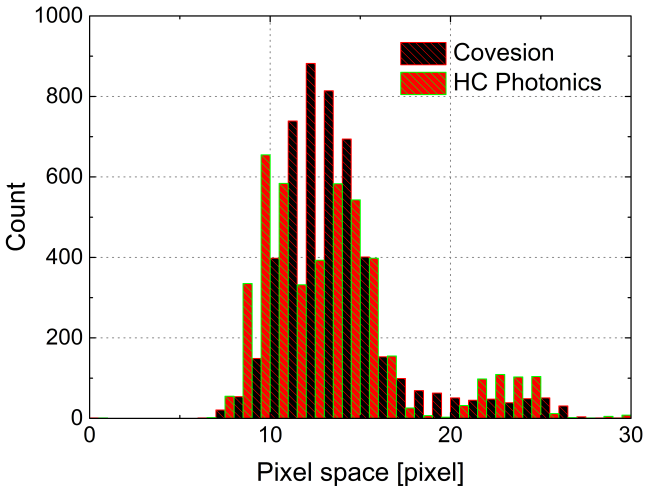

FIGURE 3.5: Histogram of the domain width for two crystals as shown in figure 3.4. The width for each domain is given by the difference of adjacent peaks of the red curve.

Manufacturer	**Duty cycle** [%]	**RDC** [%]
HC Photoncs	41.3/58.7	6.3
Covesion	45/55	7.5

TABLE 3.1: Average duty cycle and RDC error of two PPLN crystals used in this work.

In equations 2.4, function $g(z)$ is used to describe the structure of crystal in the space domain. For the PPLN crystal, $g(z)$ has the form of equation 2.16, which can also be represented in the spatial frequency domain as $\widetilde{g}(\Delta k)$. In particular, it is more convenient to discuss the RDC error in the spatial frequency domain since the value of $|\widetilde{g}(\Delta k)|^2$ is strongly correlated with the intensity of parametric process with a phase mismatch of Δk. The relation between the intensity of SPDC and the RDC error will be discussed further in Chapter 4 when the noise properties of UCD are explicitly addressed.

By analyzing the picture of the crystal, only the statistical parameters such as the RDC error can be estimated. The accurate $g(z)$ cannot be measured precisely due to technical restriction. Therefore, $|\widetilde{g}(\Delta k)|^2$ is not available. But the assembly average $< |\widetilde{g}(\Delta k)|^2 >$ can be calculated using equation 3.1 when the average duty cycle and the RDC error are known. The details of derivation can be found in Appendix A.

$$\begin{aligned} < |\widetilde{g}(\Delta k)|^2 > = & \frac{2L}{\Delta k^2 \Lambda}[1 - exp(-\Delta k^2 \sigma_z^2)] \\ & + \frac{4}{\Delta k^2} exp(-\Delta k^2 \sigma_z^2) \frac{(1 - cos\frac{\Delta k L}{2})\{1 - cos[\Delta k \Lambda (1 - D)]\}}{sin^2 \frac{\Delta k \Lambda}{2}}, \end{aligned} \tag{3.1}$$

where σ_z is the standard deviation of boundary position, D is the average duty cycle.

The intensity of parametric process with a phase mismatch of Δk is proportional to the value of $|\widetilde{g}(k)|^2$. Therefore, the parametric process like SPDC is expected to have higher intensity when the RDC error is larger. Figure 3.6 shows an example of $|\widetilde{g}(\Delta k)|^2$ with assigned RDC parameters. The pedestal of the curve is elevated with the increase of RDC error and some additional peaks appear at $\Delta k = 2j \cdot 2\pi/\Lambda$ (j is an integer) when $D \neq 50\%$.

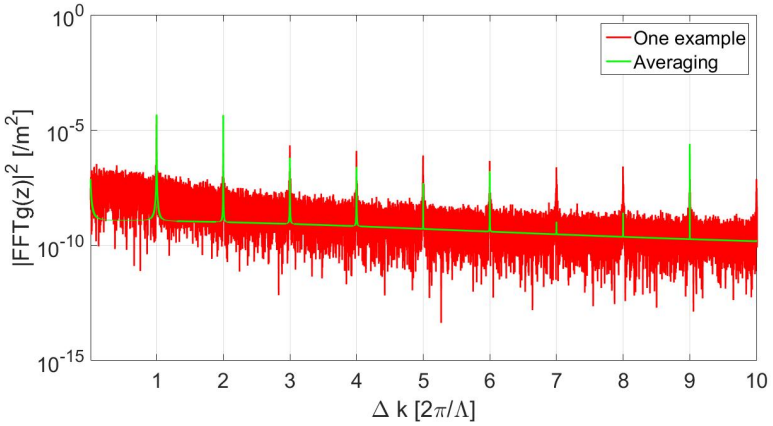

FIGURE 3.6: $|\widetilde{g}(\Delta k)|^2$ as a function of Δk. The RDC error is 6.3%, the duty cycle is 41.3% and the poling period Λ = 11.97 µm.

3.2 Characterization of the UCD

The detection efficiency and the background noise are the two most important parameters of UCD since these parameters decide the detectivity of the system eventually. With those two parameters, the SNR of the detection can also be calculated if the power of the IR signal is specified. These two parameters are all related to the pump power, i.e. the upconversion efficiency and the background noise all increase

when a higher power is used (for $P_p < P_{max}$). Therefore, it is not practical to improve the performance of UCD by merely increasing the pump power. In this section, the effect of pump power on the upconversion efficiency and the background noise are investigated in detail.

3.2.1 Intracavity Power

The backbone of the UCD is a ring laser operating at 1064 nm with a Nd:YVO_4 crystal as the gain material, which is optically pumped by an 808 nm LD. In order to achieve a high intracavity pump power, all the cavity mirrors are highly reflective ($R > 99.9\%$) at 1064 nm. But in order to evaluate the performance of the system, a ring laser is built by removing the PPLN crystal and replacing mirror M4 with a decoupler ($R = 80\%$ at 1064 nm). Figure 3.7 shows the relation between the output power of the ring laser and the absorbed 808 nm pump power. The slope efficiency of the laser is 48%, which is smaller than the value in the literature [68], but it can be improved by putting the PPLN crystal back inside the laser cavity because of the better overlap between the two beams (the 1064 nm laser and the 808 nm pump) inside the Nd:YVO_4 crystal. When the power of 808 nm pump is greater than 10 W, the degradation of beam quality due to the thermal lensing effect is observed, and the output power of the laser can no longer increase linearly with respect to the 808 nm pump power.

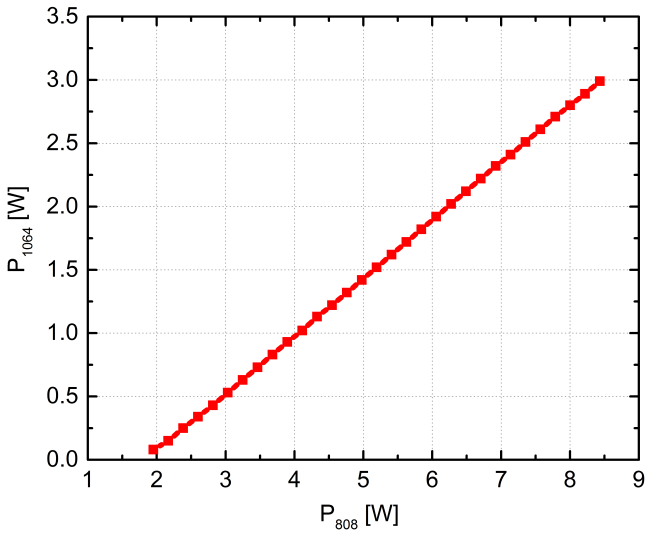

FIGURE 3.7: The output power of 1064 nm ring laser as a function of the absorbed 808 nm pump power.

The maximum output power of the ring laser is around 3 W. Compared to the transmission loss of the decoupler (T = 20%), the rest losses due to the other components can be neglected. Therefore, the total loss of the laser cavity can be assumed around 20%. Thus, the intracavity power is around 3 W/20% = 15 W. For the upconversion detection, the decoupler is replaced by a high-reflectivity mirror. The cavity loss can be estimated as $1 - 0.998^{12} \approx 2\%$ by assuming the average reflectivity of 12 working surfaces is 99.8%. Therefore, the maximum circulating pump power is around 3 W/2% = 150 W.

In the experiment, the intracavity power of the 1064 nm laser is monitored by measuring the leakage power $P_{leakage}$ from M1, whose transmission ($T_{M1} = 0.0117\%$) is characterized before applied in the measurement. The intracavity power can be

estimated by $P_p = P_{leakage}/T_{M1}$. Note that the transmission of M1 $T_{M1} = 0.0117\%$ accounts for the transmission of two surfaces. Thus, it is smaller than the transmission of the front surface since the rear surface of M1 is not AR coated.

3.2.2 Upconversion Efficiency and Background Noise

The upconversion efficiency and the background noise of the UCD are characterized when the system is optimized for the detection of the IR signal at 1575 nm. The linear polarized IR signal coming out of a fibre tip is focused by an f = 11 mm lens into a 25-mm long PPLN crystal with a poling period of Λ = 11.97 µm. The diameter of the focus spot is estimated around 300 µm. The direction of the IR beam is carefully adjusted until it is fully overlapped with the 1064 nm pump beam. The temperature of the PPLN crystal is maintained at 67.3 °C at which the power of the upconverted signal is maximized. M4 and M3 in figure 3.8a serve as the IR signal coupler and the upconverted signal decoupler during the detection. Their transmissions are measured as $\sim$ 89% at 1575 nm and $\sim$ 80% at 635 nm, respectively. A fW-detector is used for the background noise measurement. The result is shown in figure 3.8b, where η_{up} is the internal upconversion efficiency given by $P_{635}\lambda_{635}$ / $P_{1575}\lambda_{1575} \cdot 1$ / $T_{M3,M4}$. In this experiment, the maximum 1064 nm pump power is around 170 W and the maximum internal upconversion efficiency is $\eta_{up} \approx 50\%$.

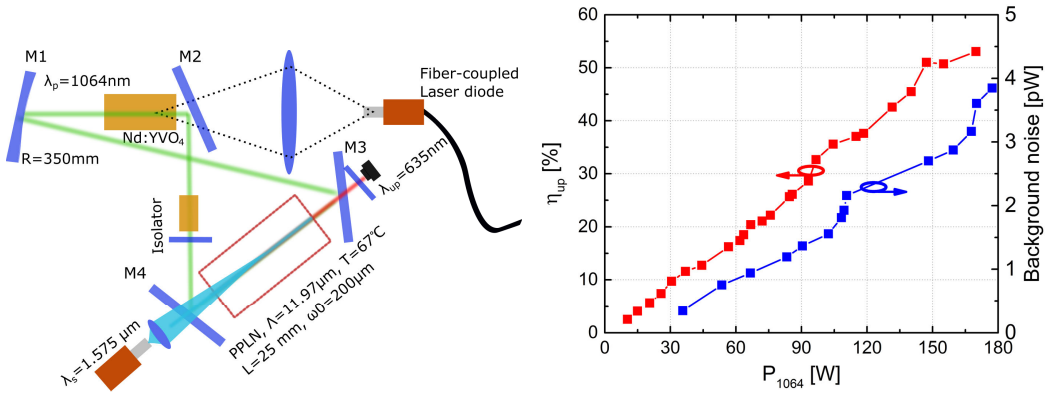

(a) (b)

FIGURE 3.8: (a) Experimental setup and (b) the results for the upconversion efficiency η_{up} and the background noise. A bandpass filter with λ_c = 635 nm, and λ_{FWHM} = 10 nm is placed in front of the detector.

3.3 UCD for Weak Signal Detection

The power of the backscattered signal in a typical atmospheric lidar application is very small (estimated at the level of $\sim$ 1 nW). Therefore, a detector with a low background noise is preferred for weak signal detection (i.e. received power in the order of 1 nW or less). In order to evaluate the performance of the UCD before using it for atmospheric lidar measurement, a weak signal is measured, and the effect of pump power on the SNR is analyzed accordingly.

3.3.1 Experimental Setup and Results

The experimental setup for the weak signal detection is shown in figure 3.9a. Instead of focusing the IR signal into the PPLN channel directly as shown in figure 3.8a,

the output of the fibre laser at 1575 nm is focused onto a rotating diffuser that is placed ~ 5 m away from the UCD. A 3″ lens with a focal length of 300 mm is used to collect and to focus the backscattered signal into the PPLN crystal. The optical field of the IR signal in front of the lens can be approximated as a plane wave, and the wavefront of the input field after the focusing lens becomes a converging spherical wave. Therefore, the $I_s(\phi)$ can be assumed constant for different input angle ϕ.

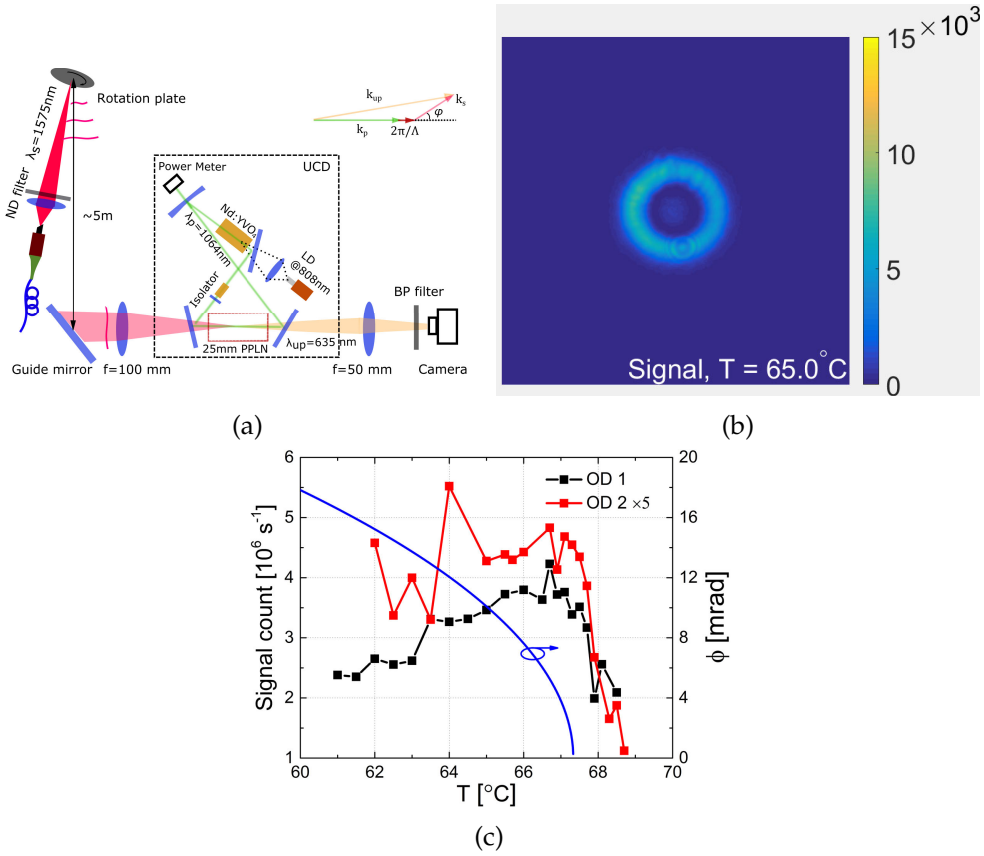

FIGURE 3.9: (a) Experimental setup for the backscattered signal measurement. (b) An example of the ring structure taken by the camera. (c) Angle ϕ for the noncollinear QPM and the upconverted photon count given by the camera as a function of the temperature of the PPLN crystal.

The output power of the fibre laser is 3 mW. Two ND filters with OD = 1, 2 are applied separately in order to attenuate the IR signal power. The bandpass filter shown in figure 3.8a is still used here to reduce the noise. The upconverted signal is measured by an EM-CCD camera (Luca S 658M, Andor) with an integration time of 3 s. Figure 3.9b shows a typical ring structure given by the upconversion signal with the noncollinear QPM condition. The speckle effect due to the interference is reduced by the rotating diffuser. After the background subtraction, the sum of the electron number in each pixel on the whole image is used to characterize the power of the upconverted signal. Figure 3.9c shows the upconverted photon count at different temperatures. Apparently, the collinear upconversion is achieved when the temperature is around 67 °C. With decreasing temperature, the QPM angle ϕ increases, which results in two effects on the detection efficiency: first, the upconversion efficiency decreases due to the decrease of interaction length between the IR signal and the pump field; second, the solid angle from which to collect the IR

signal increases since the acceptance angle is almost a constant in this range. In general, these two opposite effects counteract each other to some degree. Therefore, the efficiency has little change in the temperature interval between 64 °C and 67 °C. The efficiency plunges significantly when the temperature is larger than 67 °C due to phase mismatching. In addition, it is difficult to conclude that the collinear QPM gives the maximal detection efficiency. The noise count rate is $\sim 1 \times 10^4$/s.

3.3.2 Signal-to-Noise Ratio

SNR is commonly used to evaluate the performance of a detection system. It is necessary to build a model for the SNR estimation when a UCD is used for IR detection. For a telecom band IR detection, the USPDC process is the primary noise source, and its power is roughly proportional to the square of the pump power. When the USPDC noise dominates all other noise sources in excess of optical shot noise, the SNR of the UCD can be derived from a similar analysis in [69]:

$$SNR = \frac{P_s \omega_{up} \eta_{up}}{\omega_s \sqrt{2B\hbar\omega_{up}(P_s \omega_{up} \eta_{up}/\omega_s + P_{USPDC})}}, \tag{3.2}$$

where η_{up} is the upconversion efficiency that can be calculated using equation 2.12. The loss due to the reflection of mirrors is neglected. P_s is the power of the IR signal, B is the detection bandwidth, $\hbar$ is the reduced Plank's constant, ω is the angular frequency, P_{USPDC} is the average power of USPDC noise, which can be estimated as $P_{USPDC} = \alpha P_p^2$, α is a fitting parameter.

Based on equation 3.2, the SNR as a function of the input power of IR signal can be calculated when the 1064 nm pump power is specified. The value of α is the fitting result of the measured noise power in figure 3.8b. For comparison, the SNR of an InGaAs APD (Thorlabs, APD110C) is also calculated.

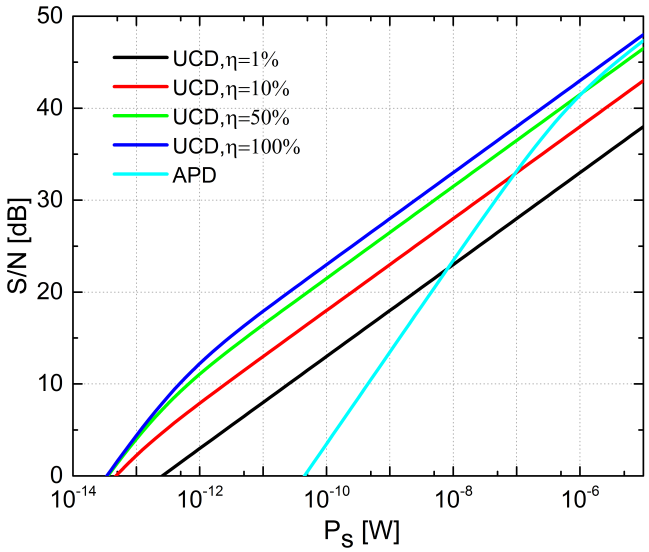

FIGURE 3.10: SNR of the UCD and the InGaAs APD as a function of the IR power P_s. The APD has a responsivity of 10 A/W, noise figure of 10 and noise equivalent power of 0.46 pW/$\sqrt{\text{Hz}}$. The bandwidth of detection here is assumed 10 kHz.

Figure 3.10 shows that the UCD has a better performance than the APD when the IR signal power $P_s < 1$ nW. The SNR of the UCD can be improved by increasing

the upconversion efficiency (i.e. increasing the pump power), but at the compromise of a higher value of P_{USPDC}. Therefore, the SNR for a very weak signal ($P_s < 0.1$ pW) detection cannot be further improved by simply increasing the pump power because it reaches a point where the USPDC noise dominates the shot noise. In order to circumvent the USPDC noise and thereby improve the SNR further for weak IR signal detection, strategies for noise reduction should be implemented.

In equation 3.2, only the effect of the upconversion process is considered. But in the practical measurement, the SNR is also affected by the performance of the detector that is used to measure the upconverted signal. Therefore, the formula for the SNR varies with the properties of the specific detector used in the experiment. In Chapter 5, a formula for the SNR calculation when a PMT is used will be presented.

Chapter 4

Noise Properties of the Upconversion Detector

This chapter provides both experimental and theoretical study on the noise properties of upconversion detectors. A frequency beat noise that originates from the pump beam's longitudinal mode beating will be discussed first. The principle of beat noise and its effect on the frequency response of UCD will be explained in detail. Furthermore, the 2nd generation UCD with the backbone of a ring laser is optimized to possess the property of being free from beat noise, which provides a flat frequency response over ~ 1.0 GHz bandwidth for IR detection. Secondly, the principle of noise photon generation due to USPDC, SHG-SPDC, upconverted thermal radiation and upconverted spontaneous Raman scattering process will be explicitly addressed. In particular, experiments of noise measurement along with the theoretical model for the noise calculation will be presented. In the last section of this chapter, a discovery of the spatial (along with spectral) distribution of the USPDC noise photon and its physical principle will be presented. According to this newly discovered phenomena, a method for noise reduction based on spatial filtering is proposed, which results in a 14 dB dark-count rate reduction for the UCD in a single-photon counting measurement.

4.1 Frequency Beat Noise

Increasing the upconversion efficiency and lowering the background noise are the two most important tasks for UCD development, and they were discussed repeatedly in the literature. Meanwhile, the discussion about the frequency response of a UCD is relatively rare. However, a flat (or uniform) frequency response is also an essential parameter for a UCD, especially when it is used for high-bandwidth detection such as high-speed, free-space optical communications. In this section, the frequency response of a UCD is discussed, and an experiment of measuring an amplitude modulated IR signal over a wide bandwidth (up to frequencies in excess of 1 GHz) via the UCD is demonstrated. It is worth pointing out that the amplitude modulated IR signal is produced by combining beams from two 1547 nm narrow-linewidth lasers in a fibre coupler while tuning their wavelength difference down to 10 pm or less. The measured Fabry-Pérot spectrum of the UCD at 1064 nm confirms the enhanced spectral stability from multiple to single longitudinal mode pumping condition. The deleterious effects of using a multimode pump to the high-bandwidth RF spectrum of the 630 nm are described analytically and demonstrated experimentally. Moreover, after changing the PPLN crystal and replacing the IR coupling mirror of the UCD, the output of a He-Ne laser at 3.39 μm is upconverted by the UCD, the experimental result further prove that the GHz-bandwidth UCD can

be extended to the MIR ($2 \sim 5\,\mu m$) range as an alternative to cooled low-bandgap semiconductor detectors.

It is necessary to point out that most of the material present in this section (Section 4.1) has already been discussed in paper [70] except for the experiment of upconverting the 3.39 µm IR signal with multi and single longitudinal-mode pump.

4.1.1 Introduction

Based on the scheme of UCDs, they can be classified as either single-pass pumped or cavity-enhanced. In single-pass type UCDs, both the IR signal and the pump transmit through the nonlinear crystal only once. High-intensity single-pass (non-resonant) pumping – therefore, high conversion efficiency – is usually achieved by using a waveguide nonlinear crystal [18] wherein the upconversion process can be strongly confined in a single spatial mode. A maximum internal conversion efficiency exceeding 90% and an overall detection efficiency of 46% have been achieved in a single-pass UCD for 1560 nm signal using a 50 mm PPLN waveguide and a 1064 nm pump with power in the order of 100 mW [71]. On the other hand, UCDs with cavity enhancement achieve high pump intensities by incorporating a bulk nonlinear crystal inside a resonant cavity, for example, inside an Nd:YVO_4 laser resonator (i.e. intracavity UCDs) [19]. In this way, high circulating pump powers of several tens (or hundreds of watts depending on pump beam waist size) allow for the upconversion of the single-pass IR signal with the maximum possible conversion efficiency. Pan and Zeng [19] have achieved an internal conversion efficiency of 74% with 80.5 W of circulating pump. An internal conversion efficiency of 90% (overall efficiency of 59%) has also been achieved for another UCD in which the 1064 nm pump laser is external to the resonant cavity, at a circulating power of 23 W [72].

Intracavity UCDs relying on a linear Nd:YVO_4 cavity have been observed to operate in multilongitudinal pump modes [19]. It has been previously proposed that, instead of a linear cavity, the use of a ring cavity with a non-reciprocal element (e.g. an optical isolator) can force the 1064 nm pump to propagate unidirectionally [20, 21]. This results in a more spectrally stable pump since the spatial hole burning in the Nd:YVO_4 crystal is significantly suppressed. A higher maximum conversion efficiency and a lower standard deviation of the SFG output intensity was experimentally observed for the ring cavity system than for the linear cavity [21]. However, no sufficient data were presented in these previous studies to establish that the circulating pump operated in a single longitudinal mode even with a ring cavity. In [20], Pan et al. were unable to observe any significant effect to the SFG output even if the ring cavity 1064 nm pump was made to run in an increased number of longitudinal modes. This is likely due to their detector sampling rate being too low compared to the pump beat frequencies. Pan and co-authors [20] also proposed a model to describe the interaction between a quantum signal and the multimode pump, but it failed to account for temporal fluctuations of the instantaneous pump intensity due to the beating of the oscillating modes. This model was later amended in the work of Pelc et al. [73] which demonstrated that a penalty of using a multimode pump (versus single mode) is the reduction of the maximum achievable average conversion efficiency. Pelc and co-authors used an unmodulated (or DC) IR signal and only measured the RF spectrum of the unconverted part of this IR signal, which was found to inherit the beat frequencies associated with the pump.

Here the investigation is extended to study the properties of a high-bandwidth intracavity upconversion detector that uses a bulk PPLN inside a 1064 nm Nd:YVO_4 unidirectional ring cavity – comparing single mode versus multilongitudinal mode

operation. The UCD is described by a transfer function, which characterizes the capacity of the detector to transfer the fast modulation of the input IR signal, at a given frequency, to the SFG output. In this study, the transfer function is examined over a wide range of frequencies (up to GHz level) using FFT spectral analysis. This allows us to characterize the performance of the UCD for high-speed, i.e. high-bandwidth, detection applications. Simultaneous FFT analyses of the GHz-sampled instantaneous powers of the input IR signal, the SFG output, as well as the small 1064 nm pump leakage through a cavity mirror allow us to quantitatively demonstrate the UCD's performance and how it is influenced by the pump operating in multilongitudinal mode versus single mode. Furthermore, the optical spectrum of the 1064 nm pump that leaks out of another cavity mirror is also monitored using a high-finesse scanning Fabry-Pérot interferometer (FPI) to directly track the number of longitudinal modes. The improved single longitudinal mode pump operation achieved with a unidirectional ring cavity design enables the UCD to be useful over a wide range of frequencies free from undesirable effects of the 1064 nm mode beating. In other words, the SFG output has a Fourier spectrum that closely mimics that of the original IR signal. Some applications of the GHz-bandwidth upconversion detector, when extended to $2 \sim 5\,\mu m$, are free-space optical communications [74, 75], pulse laser temporal profiling (e.g. accurate rise-time and fall-time measurements) [76] or modulation frequency response characterization [75] of MIR quantum-cascade lasers and optical parametric oscillators, and IR heterodyne detection [77].

4.1.2 Theory

The upconversion efficiency η is normally considered as a constant in upconversion detection if the average pump power is stable. Obviously, this is a good assumption for the weak and low-bandwidth signal detection. But in the general case (especially at sufficiently short temporal scales), η may fluctuate over time due to variations in the instantaneous pump power $P_p(t)$, for example, when the pump is lasing with multilongitudinal modes. If the frequency components of the pump fluctuation are comparable to the signal frequency, it will induce extra noise for the detection and thereby degrade the SNR. Before applying the upconversion detector for high-bandwidth IR signal detection, a model is developed to calculate the transfer function of the UCD and investigate the effects of multimode pumping on the spectrum of the SFG output.

Derivation of the Transfer Function of the High-bandwidth UCD

The physical model handling the high-bandwidth UCD is derived from equations 2.4. The amplitude of the interaction fields is a function of position z and time t. More specific, an IR input signal field $a_s(t)$ with frequency ν_s interacts with a strong pump field $a_p(t)$ with frequency ν_p in a periodically poled nonlinear crystal of length L. The upconversion process results in an SFG output field $a_{up}(t)$ with frequency $\nu_{up} = \nu_s + \nu_p$. The assumptions of plane-wave interaction and non-depletion of the optical pump are assumed valid. Moreover, the interaction time of the three fields in the crystal is assumed to be much shorter than the time scales associated with (i) the pump power fluctuation [73], and (ii) the IR signal (and SFG output) modulation.

The coupled equations for $a_s(t)$ and $a_{up}(t)$ are given by:

$$\frac{\partial a_s(z,t)}{\partial z} = -i\kappa a_p^*(t) a_{up}(z,t) e^{-i\Delta k z} \tag{4.1a}$$

$$\frac{\partial a_{up}(z,t)}{\partial z} = -i\kappa a_p(t) a_s(z,t) e^{i\Delta k z}. \tag{4.1b}$$

The phase mismatch of the SFG process Δk is given by equation 2.17b. a_j is a normalized field such that $|a_j|^2$ gives the photon rate. The coupling coefficient κ:

$$\kappa = 2\pi\epsilon_0 d_{eff}\Theta\left[2h\nu_s\nu_{up}\nu_p Z_0^3/(n_s n_{up} n_p)\right]^{1/2}, \tag{4.2}$$

where d_{eff} is the PPLN's effective nonlinear coefficient, n_j is its refractive index, Θ is the mode-overlap integral, h and $Z_0 = \sqrt{\mu_0/\epsilon_0}$ are the Planck constant and the vacuum permittivity, respectively (where μ_0 is the vacuum permeability).

If the QPM condition is fulfilled with $\Delta k = 0$, the solutions to equations 4.1 take the following form:

$$a_s(L,t) = a_s(0,t)\cos\left[\kappa|a_p(t)|L\right] + a_{up}(0,t)\sin\left[\kappa|a_p(t)|L\right] \tag{4.3a}$$

$$a_{up}(L,t) = -a_s(0,t)\sin\left[\kappa|a_p(t)|L\right] + a_{up}(0,t)\cos\left[\kappa|a_p(t)|L\right]. \tag{4.3b}$$

For the case of IR signal detection, in which $a_{up}(0,t) = 0$, the field amplitude of the upconversion (SFG output) signal can be simplified as:

$$a_{up}(L,t) = -a_s(0,t)\sin\left[\kappa|a_p(t)|L\right]. \tag{4.4}$$

The time-dependent conversion efficiency can then be written as:

$$\eta(t) = |a_{up}(L,t)|^2/|a_s(0,t)|^2 = \sin^2\left[\kappa|a_p(t)|L\right]. \tag{4.5}$$

Let the normalized frequency spectra of the photon rates $|a_s(0,t)|^2$ and $|a_{up}(L,t)|^2$ be:

$$\tilde{N}_s = b_1\mathscr{F}\{|a_s(0,t)|^2\} \tag{4.6a}$$

$$\tilde{N}_{up} = b_2\mathscr{F}\{|a_{up}(0,t)|^2\}, \tag{4.6b}$$

where $\mathscr{F}\{\}$ denotes the Fourier transform, and b_1 and b_2 are constants upon normalization of the spectra by their respective zero-frequency components. In this study, the detector system is described by a normalized transfer function $\tilde{H}(f)$ such that:

$$\tilde{N}_{up}(f) = \tilde{H}(f)\tilde{N}_s(f). \tag{4.7}$$

Combining equations 4.5 to 4.7, the modulus of the transfer function is:

$$|\tilde{H}(f)| = \frac{|b\mathscr{F}\{|a_s(0,t)|^2\} \circledast \mathscr{F}\{\eta(t)\}|}{|\mathscr{F}\{|a_{up}(0,t)|^2\}|}, \tag{4.8}$$

where $\circledast$ is the convolution operator and b is a constant such that $|H(0)| = 1$.

When the UCD is pumped with a single longitudinal mode laser, $a_p(t)$ is essentially constant, and so is $\eta(t)$, for temporal scales greater than or equal to the inverse of the detector bandwidth. If η is independent of time, then $|\tilde{H}(f)|$ is unity within the detector bandwidth. However, when the pump operates in multilongitudinal

mode, its instantaneous power P_p will fluctuate leading to a more complicated frequency response of the UCD.

The Case of Two Longitudinal Pump Modes

For the case of two-mode pumping, the instantaneous pump power is no longer constant:

$$P_p(t) = P_{ave}\Big[1 + \alpha\cos(2\pi\Delta f t + \phi)\Big], \tag{4.9}$$

where $P_{ave} = h\nu_p < |a_p(t)| >^2$ is the average pump power, α is the contrast of the sinusoidal power variation due to mode-beating, Δf is the mode frequency spacing, and ϕ is an arbitrary phase. From equations 4.5 and 4.9, $\eta(t)$ can be expressed (for the two-mode case) as:

$$\eta(t) = \sin^2\left[\pi/2\sqrt{P_{ave}/P_{max}[1 + \alpha\cos(2\pi\Delta f t\varphi)]}\right], \tag{4.10}$$

where $P_{max} = \pi^2 h\nu_p/(4\kappa^2 L^2)$. Examples of instantaneous pump power fluctuations are shown in figure 4.1a. The corresponding conversion efficiency $\eta(t)$ and the magnitude of its spectrum $\mathscr{F}\{\eta(t)\}$ are shown in figure 4.1b and figure 4.1c, respectively. Figure 4.1c reveals that the spectrum of η for the dual mode case may have several frequency components at $f = m\Delta f$ $(m = 0, 1, 2, \dots)$ and not only limited to components at $f = 0$ and $f = \Delta f$.

The red curve in figure 4.1 shows the case of $P_{ave} = P_{max}$ and unity contrast. It is characterized by the presence of strong higher order peaks in its conversion efficiency Fourier spectrum. The green curve is also for $\alpha = 1$ but lower $P_{ave} = 0.25P_{max}$. The blue curve is for $\alpha = 0.05$ and $P_{ave} = 0.25P_{max}$, which corresponds to $\eta_{ave} = 50\%$ or close to the operating point in the experiment. Apparently, the non-zero frequency components become weaker with decreasing α (with $\alpha = 0$ resulting in the single mode case). The black curve simulates the case of $\alpha = 0.5$ and a relatively low average conversion efficiency obtained at $P_{ave} = 0.009P_{max}$, i.e. $\eta_{ave} = 20\%$, like those obtained with the upconversion system described in a previous work [33]. It shows that the component at $f = 2\Delta f$ is 17 dB lower than the component at $f = \Delta f$. This implies that higher order effects or frequency components larger than Δf are also reduced when operating at relatively low average conversion efficiency.

4.1.3 Experimental Setup

In order to achieve high-bandwidth IR signal detection with frequency upconversion, a unidirectional ring cavity configuration is chosen for the UCD. In comparison to the linear cavity, the unidirectional ring cavity design is more capable of stable lasing at a single longitudinal mode due to the inhibition of spatial hole burning [21, 78]. The schematic diagram of the UCD is shown in figure 4.2a.

The design of the UCD has been introduced in Chapter 3, its details can be found on page 27. But it is necessary to specify that a 25-mm long bulk PPLN with a poling period $\Lambda = 11.73\,\mu m$ is used here (placed between M3 and M4), and its temperature is kept at $T = 58\,^{\circ}C$ to maximize the conversion efficiency.

Figure 4.2b shows the schematic diagram of the modulated IR signal generator. Two identical fibre-coupled narrow-linewidth laser diodes (LD1 and LD2) with a central wavelength around 1547 nm are combined through a polarization-maintaining fibre splitter/combiner (50:50 split ratio). One fibre coupler output is

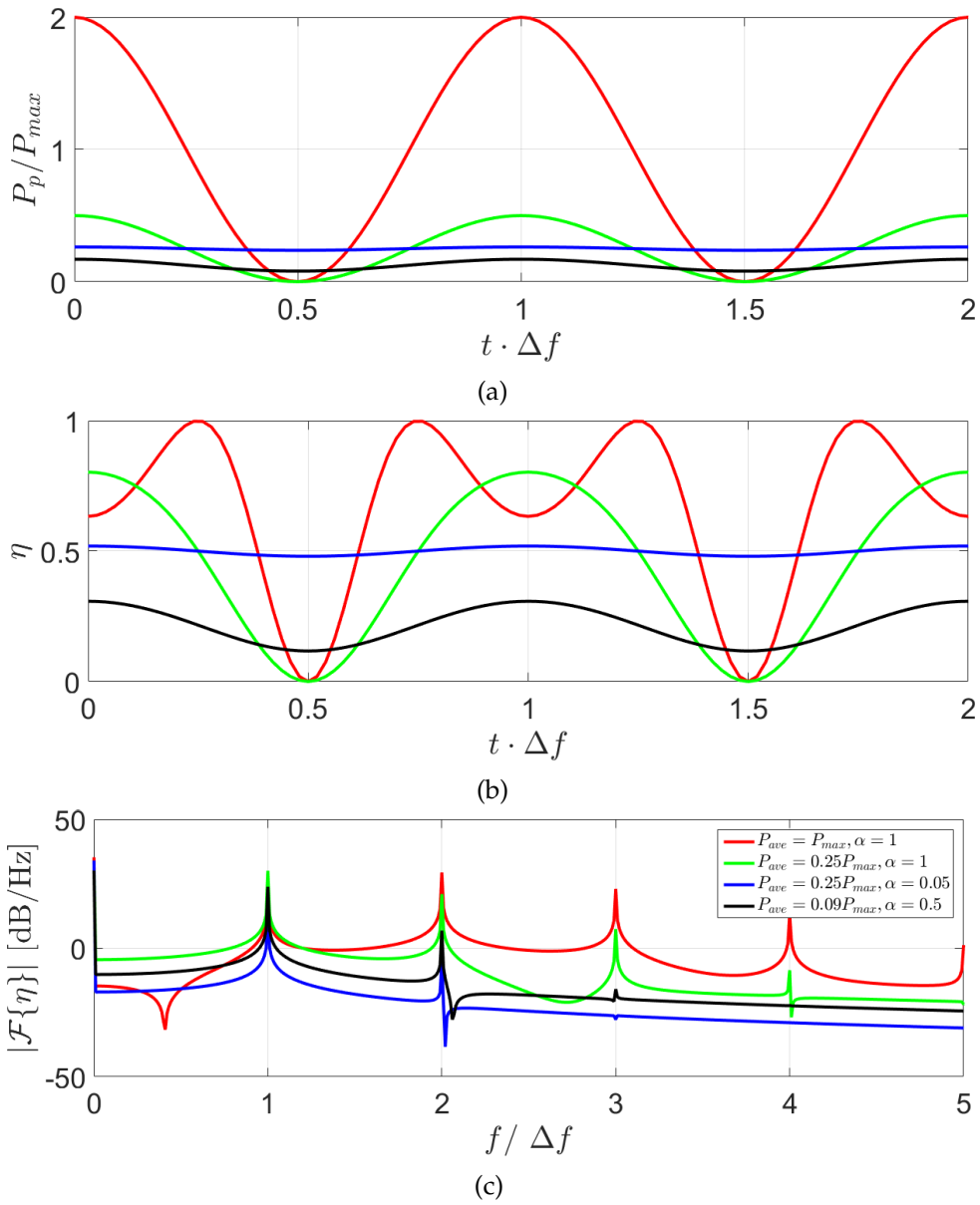

FIGURE 4.1: (a) Instantaneous pump power P_p (normalized by P_{max}) versus time (normalized by the inverse of the mode frequency spacing Δf) for four different combinations of average pump power and contrast that describe the beating of two pump axial modes, (b) corresponding instantaneous conversion efficiency given by equation 4.10, and (c) magnitude of the FFT of conversion efficiency curves shown in (b).

used to monitor the IR signal directly with a fast detector and/or connected to an optical spectrum analyzer (OSA) for coarse-tuning of the wavelength difference. The other output serves as the IR signal of the UCD in figure 4.2a. The modulation frequency f_M (proportional to the wavelength difference of LD1 and LD2) can vary from near-zero to $\sim$ 1.0 GHz, with a stability of a few MHz, by tuning either the temperature or the drive current of the two laser diodes. The interferometric contrast is also maximized by balancing the output power of the two lasers. To minimize both insertion loss and optical feedback, polarization controllers (PC1 and PC2) and fibre isolators (ISO1 and ISO2) are attached to the laser diodes. This setup is also able to create challenging modulation frequencies extending to 10 – 100 GHz, relevant for high-speed communications.

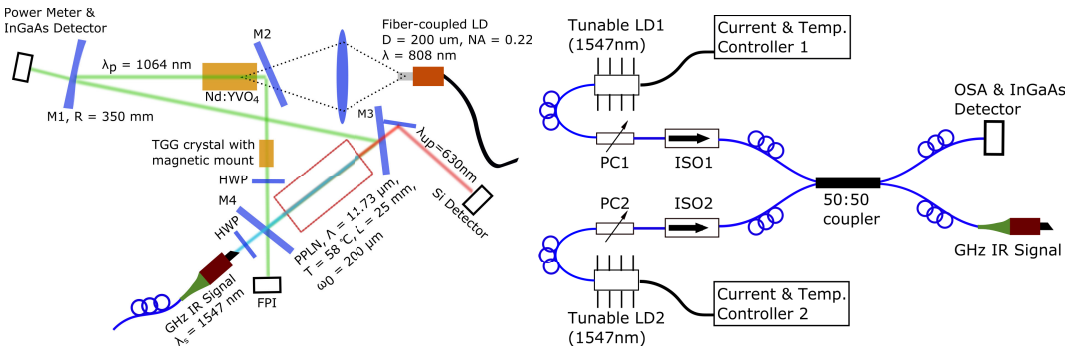

(a) (b)

FIGURE 4.2: (a) High-bandwidth IR UCD based on a unidirectional ring cavity and (b) modulated signal generator with a central wavelength of 1547 nm and modulation frequency tuning up to GHz.

4.1.4 Results

During the experiment, the 808 nm laser diode is set at an output of 6.5 W, which can maintain a 1064 nm intracavity circulating pump power of 147 W. The average power of the 1547 nm signal used is 2.1 mW and the resulting average power of the 630 nm SFG signal coming out of the UCD is 2.17 mW. Considering 80% total transmission at 630 nm through M4 and a bandpass filter, the average internal conversion efficiency $\eta_{ave} = 52.7\%$. The cavity alignment has been optimized to achieve a single transverse mode profile for the 1064 nm pump with a relatively high 147 W pump power operating point. At some other pump power values, the 1064 nm pump tends to operate at multiple transverse modes – making it difficult to reliably measure the dependence of the conversion efficiency on pump power.

The number of longitudinal modes of the 1064 nm pump is monitored with a scanning Fabry-Pérot interferometer (FPI). The FPI spectra are shown in figure 4.3

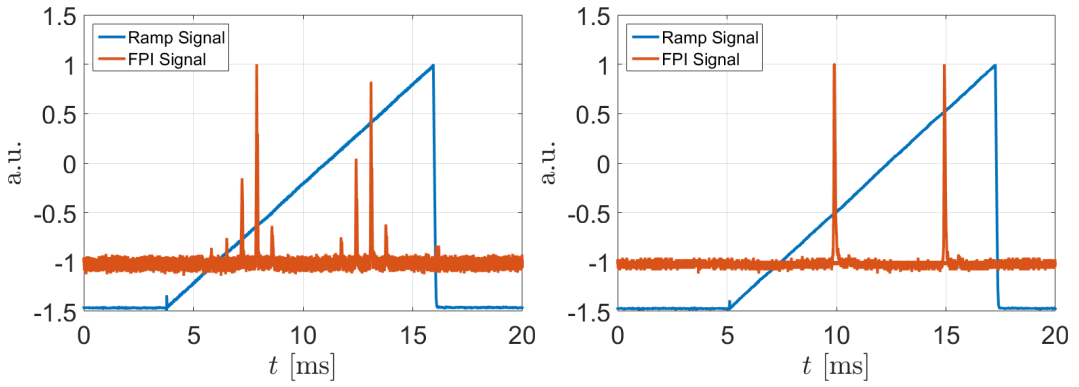

(a) (b)

FIGURE 4.3: Scanning FPI spectrum of the 1064 nm pump in (a) multiple and (b) single longitudinal mode operation. The spectra are stable for durations longer than the typical measurement time.

for the case of multiple and single longitudinal mode lasing. The UCD can be optimized for single frequency pump operation by aligning the cavity mirrors and the rotational position of the HWP.

To evaluate the performance of the UCD, the 1547 nm signal and the 1064 nm pump are measured with two InGaAs detectors (Thorlabs DET08CFC/M and DET08CL/M),

the 630 nm SFG signal is measured with a Si detector (Thorlabs DET025AFC/M). All three detectors have bandwidths exceeding 2 GHz. Output voltages of the detectors are simultaneously monitored by an oscilloscope (LeCroy 104MXs-B, 3-dB bandwidth = 1 GHz).

The Fourier spectra of the photon rates (or power) of all three interacting waves are obtained by taking the FFT of their respective detector signals which are sampled by the oscilloscope at 5 GS/s for 5 µs. Figures 4.4a to 4.4f compare the magnitude of all normalized spectra when the pump operates in multimode and single longitudinal mode. Figure 4.4c shows that when the 1064 nm pump runs in multilongitudinal mode (for example, when M3 is slightly misaligned and/or the HWP is at a suboptimal position that degrades optical isolation), it exhibits several beat frequencies at $f = m\Delta f$ (for $m = 1, 2, 3, \ldots$), where $\Delta f = 603.6$ MHz. The free spectral range (FSR) of the ring cavity is given by:

$$FSR = c/\sum_i n_i l_i, \tag{4.11}$$

where n_i and l_i are the refractive index and the length of the i_{th} medium along the path of the pump in a round-trip. According to equation 4.11, the calculated FSR of the cavity is 616 ± 25 MHz, which is in good agreement with the observed Δf. It validates that the multilongitudinal mode lasing is the main reason for the fluctuation of the 1064 nm pump power shown in figure 4.4c.

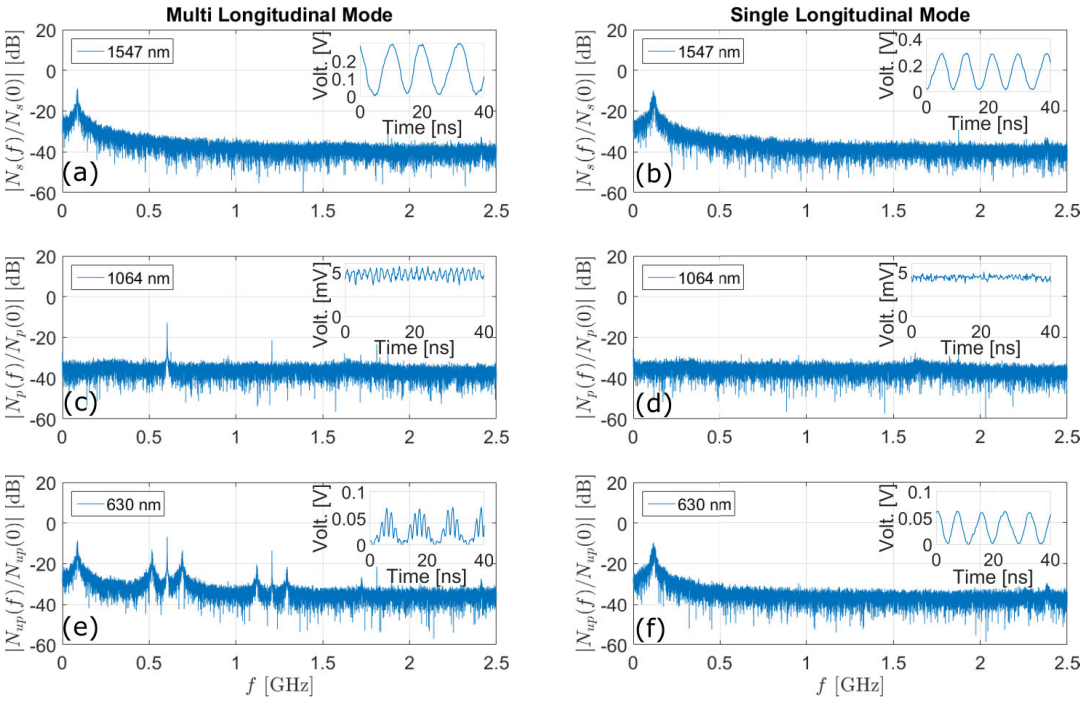

FIGURE 4.4: Modulus of the FFT spectra of simultaneously detected powers of (a), (b) the 1547 nm signal, (c), (d) the 1064 nm pump, and (e), (f) the 630 nm SFG output for (a), (c), (e) multimode and (b), (d), (f) single longitudinal mode pump operation. Each inset shows a time series of the detected instantaneous power (i.e. InGaAs or Si detector voltage) for the respective wavelength. Each FFT spectrum is normalized by their zero-frequency component.

By analyzing figure 4.4e in detail, it turned out that the peaks in the 630 nm spectrum can be separated into different groups based on their frequency spacing.

For the convenience of further discussion, these groups are named as follows: the fundamental group has only one peak at frequency $f = f_M = 88.4\,\text{MHz}$ which corresponds to the original signal shown in figure 4.4a; the secondary group contains three peaks with $f = \Delta f$ and $f = \Delta f \pm f_M$; the tertiary group also contains three peaks with $f = 2\Delta f$ and $f = 2\Delta f \pm f_M$. Even higher order peak groups well beyond the 1 GHz bandwidth of the oscilloscope are observed but highly attenuated and thus ignored in the analysis. In contrast, figure 4.4f shows no additional spurious peaks for the spectrum of the SFG signal, i.e. only the original signal at $f = f_M = 116.2\,\text{MHz}$ shown in figure 4.4b is reproduced when the pump runs in single mode.

As presented in theory, the 630 nm SFG Fourier spectrum can be calculated from the convolution of the FFT of the 1547 nm signal with the FFT of the conversion efficiency, which is revealed by equation 4.7. Alternatively, the appearance of the additional peaks in 4.4e can be explained in the following manner: it is perhaps obvious that the frequency sum $\Delta f + f_M$ and difference $\Delta f - f_M$ give rise to the side peaks of the secondary peak group. But the reason for the tertiary group is more complex. Figure 4.3a clearly shows that the 1064 nm pump has more than two oscillating modes. The beating of the two closest side-modes, one to the left and the other to the right of the strongest mode, gives rise to the frequency component at $f = 2\Delta f$, which is also confirmed by figure 4.4c. Similarly, the frequency sum $2\Delta f + f_M$ and difference $2\Delta f - f_M$ contribute to the tertiary peak group. Additionally, the higher order frequency response of the detector $(\Delta f \rightarrow 2\Delta f)$, see for example figure 4.1c, may also contribute to the tertiary group. In other words, it is possible to observe the tertiary group even if there are only two longitudinal pump modes with mode spacing Δf.

The blue curve in figure 4.1c uses the parameters $\alpha = 0.05$ and $P_{ave} = 0.25 P_{max}$, which are similar to those in the experimental result for the case of multimode pump operation (the amplitude of the peak at $f = \Delta f$ in 4.4c is –12.91 dB). This curve simulates the effect of higher order frequency response due to the beating of only two adjacent longitudinal modes. The simulation shows that the amplitude ratio between the peaks at $f = \Delta f$ and $f = 2\Delta f$ is 21 dB, which is quite larger than the measured amplitude ratio of 7 dB between the corresponding secondary and tertiary peaks shown in 4.4e. The measured ratio would be even smaller had the oscilloscope bandwidth been large enough to accommodate the tertiary group. Therefore, it is concluded that the tertiary group of peaks is predominantly due to the beating of non-adjacent pump modes (separated by $2\Delta f$) instead of the higher order $(\Delta f \rightarrow 2\Delta f)$ frequency response due to the adjacent pump mode beating.

In the following experiment, the transfer function of the upconversion detector with single mode pump is studied by tuning the modulation frequency f_M. During the measurement, the 1064 nm pump power remains constant and so does the conversion efficiency. The normalized FFT spectra of the 1547 nm signal and the 630 nm SFG output signal power are monitored simultaneously. Figures 4.5a to 4.5c show the modulus of the two spectra for different f_M values. Figure 4.5d is the measured modulus of the normalized transfer function $|\tilde{H}(f)|$ of the upconversion detector which is relatively flat in the range of 0 to 1 GHz.

The theoretical model of the single axial mode pumped UCD implies that the IR detector has the ability to measure the signal with an unlimited bandwidth (or more precisely, limited only by the fast Si based detector that detects the SFG output). Figure 4.5d empirically proves that the modulus of the normalized transfer function is flat with less than $\pm$ 0.5 dB deviation from unity within DC to $\sim$ 1 GHz. No further measurement is done due to the bandwidth limitation of the oscilloscope. If an electronic spectrum analyzer with several GHz of bandwidth is used, the effective

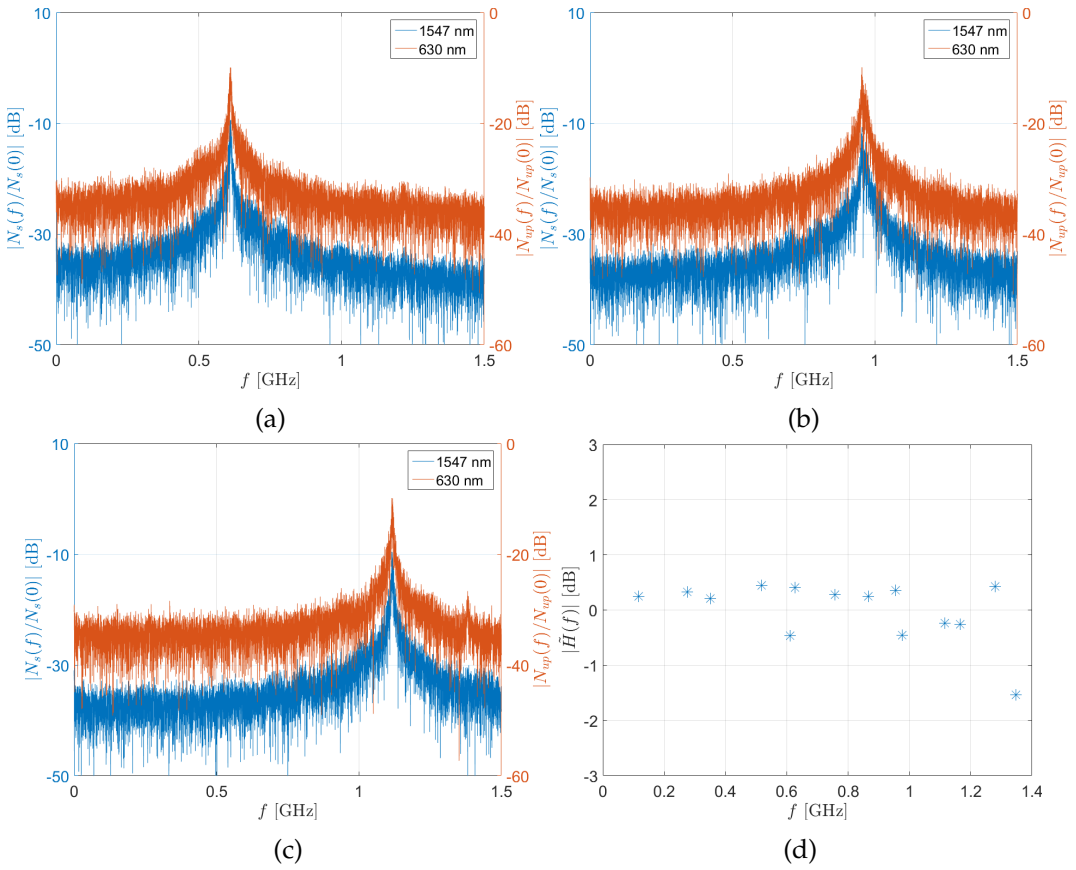

FIGURE 4.5: Magnitude of the normalized FFT spectra of the 1547 nm input signal and the 630 nm SFG output power for single frequency pump operation and for signal modulation frequency of (a) 611.8 MHz, (b) 954.4 MHz, and (c) 1.19 GHz, and (d) the measured normalized transfer function of the GHz-bandwidth upconversion detector.

detection bandwidth of the UCD can instead become limited by the bandwidth of the Si detector for the SFG signal. In the experiment, the oscilloscope limits the ability to accurately assess the transfer function of the UCD above 1 GHz.

In order to further test the frequency response of the UCD when it works in the MIR region, the source of the 1547 nm IR signal in figure 4.2a is replaced by a He-Ne laser at 3.39 µm (Model R-32172, Newport). Moreover, M4 (the IR signal coupler) mirror made of BK7 is replaced by a YAG one, which has significantly lower absorption at 3.39 µm. Another 20-mm long PPLN crystal with a poling period of $\Lambda = 22.5$ µm is used here. The maximum SFG (810 nm) output power is obtained when the temperature of the PPLN crystal is kept at 70.0 °C.

Following the same procedures of data processing as the experiment of measuring the 1547 nm IR signal, the 1064 nm pump power and the upconverted power are measured with the InGaAs and the Si based detectors, respectively. The left column of figure 4.6 shows the magnitude of normalized spectra when the 1064 nm pump operates with multilongitudinal modes, and the right column corresponds to the singlelongitudinal mode operation. The spectra of the IR signal (3.39 µm) is not included in figure 4.6 due to the lack of fast direct detector working in the MIR region. Similar to figure 4.4c, figure 4.6a also shows several beat frequencies of the pump with a frequency difference of $\Delta f = 603.6$ MHz. The first and the secondary peak are marked by red and green colour, respectively. Figure 4.6d is the spectra of the upconverted signal when the pump operates with single longitudinal mode,

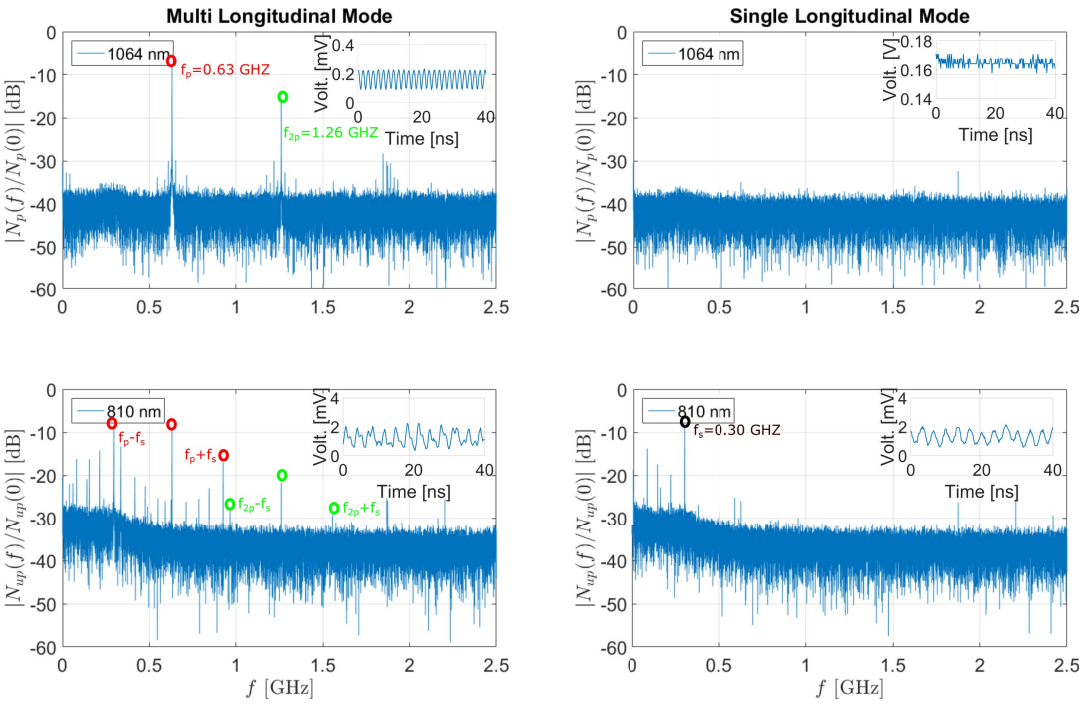

FIGURE 4.6: Modulus of the FFT spectra of simultaneously detected powers of (a), (b) the 1064 nm pump, and (c), (d) the 810 nm SFG output for (a), (c) multimode and (b), (d) single longitudinal mode pump operation. Each inset shows a time series of the detected instantaneous power (i.e. InGaAs or Si detector voltage) for the respective wavelength. Each FFT spectrum is normalized by their zero-frequency component.

and it is suspected that the peaks in the figure are due to the frequency beat between the different longitudinal modes inherent in the He-Ne laser. The highest peak at $f = 0.3\,\text{GHz}$ corresponds to the FSR of the He-Ne laser cavity (consistent with the manufacturer specified mode spacing of 316 MHz). When the UCD is in the multilongitudinal-mode operation, the spectra of the upconverted signal becomes more complicated, but the peaks can still be separated following the same principle as analyzing the peaks in figure 4.4e. The first $(f_p, f_p \pm f_s)$ and the secondary $(f_p, 2f_p \pm f_s)$ group of peaks are marked with red and green colour, respectively.

4.1.5 Discussion and Conclusion

To achieve optimal conversion efficiency with an upconversion detector, high-power pump lasers are usually employed. Since high-power pump sources tend to operate in multilongitudinal mode, Pan et al. [20] previously investigated theoretically and experimentally whether or not the quantum feature of incident signal photons is altered in the corresponding SFG photons when a multimode pumped UCD is used. Theoretically, they assumed that the total pump intensity is given by the incoherent sum of the individual mode intensities. This model failed to capture the temporal fluctuations of the pump intensity caused by the beating of the modes, which was shown in a later work by Pelc et al. [73] to be correctly described by a coherent sum (i.e. summing the fields of the modes first before taking the squared modulus). The first study into the effects of multimode pumping in a UCD initiated by Pan et al. also provided experimental results illustrating the intensity stability of the SFG output at high power levels of the pump in multimode operation. The implications of

the beating of the pump modes were not revealed by their SFG intensity time-series (neither by its spectrum had it been shown). It is possible due to the fact that their SFG output was detected by a Si single-photon counting module, which typically has a limited photon count rate of about 10 MHz (i.e. single-photon counting UCD bandwidth is well below the expected pump beat frequencies).

One can consider the results presented in this section as an extension of the study done by Pelc et al. [73]. However, investigations shown here differ from theirs in a number of aspects. Their model and experiments were expanded to accommodate for amplitude modulated IR signals at modulation frequencies covering GHz-wide dynamic range. In the previous work, only a constant (or DC) IR signal was considered. Furthermore, the instantaneous power of the 1547 nm signal, the 1064 nm pump, and the 630 nm SFG output (and for different 1547 nm signal modulation frequencies in either single or multilongitudinal pump mode operation) were monitored simultaneously. Pelc et al. only monitored their residual (1.55 µm) IR signal power, which they analysed in terms of its RF spectrum. Using a DC 1.55 µm signal, they only showed experimentally that the mode beating of the pump is manifested in the spectrum of the residual IR signal. In this work, the RF spectra of all three interacting waves were measured simultaneously, as shown in figure 4.4, demonstrating explicitly that the SFG output inherits the spectral peaks of the pump (caused by the beating of its modes) convolved with the spectrum of the IR signal. A further confirmation of the single or multimode operation of the 1064 nm pump was also performed by sending it through a scanning FPI for high-resolution spectral analysis that allows us to determine the actual number of longitudinal modes present. In the previous work, no direct measurement of the number of pump modes was performed. Instead, the authors estimated the number of modes from the ratio of their pump laser spectral linewidth (measured by an OSA) and the FSR of the laser resonator. In the present study (due to the ability to achieve single longitudinal pump mode operation), it is confirmed that the UCD has a uniform frequency response in a bandwidth as high as 1 GHz, as shown in figure 4.5 - in agreement with the theoretical model. In Pelc et al., the UCD was a single-pass type which used a PPLN waveguide and a fibre laser emitting a 1.94 µm pump with about 300 oscillating modes.

The theoretical model provides a good description of the performance of the unidirectional ring-cavity based UCD operating in either single frequency or multilongitudinal mode operation. However, it is necessary to emphasize that the model, particularly for the multimode case, can be applied to other types of upconversion detectors like those based on linear cavity [19] or single-pass systems [73] as long as the instantaneous pump power fluctuation and its influence on the upconversion efficiency are accounted for.

Fluctuations of the pump power in a linear cavity can be neglected if its beat frequency is larger than the bandwidth of the RF signal. Theoretically, the beat frequency Δf is set by the cavity length. However, the maximum Δf is limited by the shortest cavity length that can be implemented in practice. For example, if the bandwidth of the RF signal is 10 GHz, the cavity length should not exceed 15 mm, which is unrealistic for linear intracavity UCDs. Furthermore, the maximum average conversion efficiency near unity is only possible when a single longitudinal mode pumping is used [73]. The ring cavity UCD that has the potential for stable single frequency pump operation is, therefore, a better choice for high-bandwidth IR signal detection.

The implementation of an intracavity upconversion detection of sinusoidally modulated IR signals at 1547 nm with modulation frequencies as high as 1 GHz was

presented in this work. A unidirectional Nd:YVO_4 ring cavity was employed to produce 1064 nm circulating pump powers reaching 150 W. Using a theoretical model, the UCD's ability to transfer the sinusoidal intensity variation from the IR signal to the SFG output at 630 nm is shown, with equally high fidelity at any modulation frequency is made possible by operating the pump in single longitudinal mode. Theoretical/numerical predictions also showed that for multimode pump operation, spurious noise spikes in the RF spectrum of the SFG output will appear due to a convolution of the spectral features of the conversion efficiency (due to the beating pump) with that of the IR signal. These noise peaks in the SFG output spectrum ultimately degrades the upconversion detector's SNR particularly for signal frequencies located near the noise peaks. Furthermore, multimode pump operation results in unwanted higher order replicas of the signal, which create ambiguities and thereby limit the effective bandwidth of the UCD. Experimentally, it is demonstrated that the GHz-bandwidth UCD running in single frequency pump operation has a uniform frequency response over a wide range of modulation frequencies ($0 \sim 1$ GHz). The average internal conversion efficiency achieved by the presented UCD was 52.7% (or an overall detection efficiency of about 40%) at a pump power of 147 W. Like Si based detectors, fast InGaAs detectors with bandwidths of several GHz are available and can be used for telecom wavelengths. Moreover, it was also demonstrated that this GHz-UCD can easily be extended to the MIR region ($2 \sim 5\,\mu$m) by implementing minor changes to the PPLN period (i.e. change to $\Lambda > 20\,\mu$m) and the surface coatings of the ring cavity optical components [33, 79]. The experiment of measuring the 0.3 GHz beat frequency due to inherent longitudinal modes of a He-Ne laser operating at 3.39 µm confirmed that this UCD is capable of high-bandwidth detection in the MIR range. Such MIR GHz-UCD may serve as a better alternative to liquid-N_2 cooled HgCdTe photodetectors, not only for the elimination of cumbersome cooling requirements but also for significant enhancements in SNR. This variant of the high-bandwidth UCD may find great potential in MIR related applications in wireless optical communications, heterodyne detection, and laser (e.g. QCL and OPO) characterization [74–77].

4.2 Noise from the Parametric Process

As mentioned in Chapter 2, a high-intensity pump field inside the UCD usually leads to some unintended parametric processes, especially when a PPLN crystal is used as the $\chi^{(2)}$ material. Unlike that in the unpoled bulk nonlinear crystal, the RDC error in the PPLN crystal results in a pedestal effect [23], which can enhance the non-phase-matched parametric processes, such as SPDC and SHG processes. When the new designed 2nd generation UCD works in normal conditions, the typical 1064 nm pump power is larger than 100 W, and the parametric processes induced by that usually results in a significant amount of noise photon, which affects the overall detectivity (or the NEP) of the UCD.

Four kinds of the noise source (USPDC, SHG-SPDC, upconverted thermal radiation and upconverted spontaneous Raman scattering) are investigated experimentally and theoretically in this Ph.D. project. In this section, the first three noise sources (USPDC, SHG-SPDC and the upconverted thermal radiation) will be discussed in detail because these three terms are the primary noise sources for the short-wavelength-pumped UCD. However, instead of using the intracavity-pumped

UCD (introduced in Chapter 3) to investigate these noise sources directly, a single-pass upconversion system pumped by a high-power 1064 nm Yb-fibre laser is employed instead. The reasons for using a single-pass system are: 1) the laser crystal (Nd:YVO_4) in the intracavity-pumped UCD is optically pumped by an 808 nm laser diode. Hence the fluorescence generated during the lasing cannot be distinguished from the noise sources of interest directly. 2) The thermal lensing effect of the laser crystal degrades the transverse profile and changes the beam size of the pump (1064 nm) inside the PPLN crystal. 3) The 1064 nm pump power of the UCD cannot be tuned continuously. In contrast, the structure of the single-pass upconversion system is simple, and the pump power can be easily controlled by adjusting the output power of the Yb-fibre laser directly with no effect on the other experimental parameters.

The setup for the single-pass upconversion system is built in ICFO, Barcelona, Spain. The experiment is the collaboration with Anuja Padhye from ICFO, she is also a Ph.D. student working in the Mid-TECH project.

4.2.1 Introduction

As a new-concept IR detector, the upconversion detector stands out because of its low background noise at the room-temperature working conditions. However, during the process of upconversion (transfer the information contained by the IR signal to the VIS/NIR spectral range), it is also affected by some unique noise sources due to the unintended parametric processes, which decreases the detectivity of the UCD eventually. The physical principle for these noise sources (USPDC [13, 23, 24], upconverted thermal radiation [41] and upconverted SRS [25, 80]) have been reported in the literature before, but from the perspective of UCDs, the effects caused by these noise sources should be summarized in order to evaluate the performance of an UCD in general. This section provides an overview of the noise properties of the UCD.

The unexpected noise was first reported by Midwinter et al. [7] when the upconversion was used for IR detection in the 1960s. The authors suspected that the USPDC process would be the potential noise source, which was confirmed by Tang theoretically with the QED theory afterwards [13]. With the invention of periodical poling technology, the PPLN based UCD started being reported [18] in the past two decades. Some short-wavelength-pumped UCDs achieved high upconversion efficiency, but also showed a relatively large dark-count rate (>1×10^5/s). Pelc et al. analyzed the pedestal effect on the upconversion efficiency and the noise spectrum [23, 24]. As another noise source, the upconverted thermal radiation cannot be ignored when the IR signal is in the MIR ($2 \sim 5\,\mu$m) range, which was confirmed by Barh et al. experimentally [41]. It is also worth pointing out that a new noise source, the SHG-SPDC process, is identified in this Ph.D. project for the first time, and this noise source can be one of the primary noise source for an UCD potentially.

The basic principles of these noise sources are different from each other. Thus, their relative intensities have different dependencies on the working conditions. In this section, the noise power due to the USPDC, SHG-SPDC and the upconverted thermal radiation is investigated both theoretically and experimentally. It is believed that the models here can provide guidance for the calculation of the NEP (or the DCR) of an UCD, and these models can also be used to estimate the performance of an UCD during the designing process.

4.2.2 Theory

The theoretical models for USPDC, SHG-SPDC and the upconverted thermal noise processes will be introduced separately here. All these models are built on top of the theory and assumptions (page 12) that have been discussed in Chapter 2. For the convenience of further discussion, the following input parameters shared by those models are summarized in table 4.1.

	Optical Pump			PPLN crystal			
Parameters	Pump power	Beam waist	Wavelength	Crystal Length	Poling period	RDC error	Temperature
Symbol	P_p	ω_0	λ_p	L	Λ	σ	T

TABLE 4.1: Input parameters used in the theoretical models for the noise calculation.

USPDC Noise

When a short-wavelength pump is used in a UCD, the USPDC noise becomes one of the primary noise sources which cannot be removed using spectral filters due to the small spectral separation between the USPDC noise and the upconverted signal. The Feynman diagram of the USPDC process is shown in figure 1.4b. The corresponding spectral diagram and k-vectors are shown in figure 4.7.

To simplify the problem, the USPDC process is split into two steps: SPDC and upconversion. The SPDC process is very weak since it is usually non-phase matched.

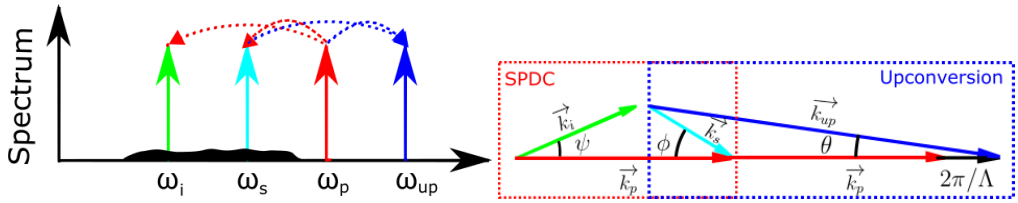

(a) (b)

FIGURE 4.7: (a) Spectral diagram and (b) k-vectors for the USPDC process in the PPLN crystal of an upconversion detector.

Therefore, the effect (e.g. depletion) caused by the SPDC process on the high-intensity pump field is neglected. Starting from equation 10 in [81], the intensity of SPDC at position z has the following form:

$$I_s(z) = \frac{\hbar\omega_s^2\omega_i d_{eff}^2 I_p z}{\pi^3\varepsilon_0 c^3 n_s n_i n_p} d\mathbf{K_s} d\omega_s \left| \int_z dz' g(z') exp(i\Delta k_d z') \right|^2, \tag{4.12}$$

where $\mathbf{K_s}$ is the transverse component of the $\mathbf{k}$ vector of the IR signal, which can be calculated by $\mathbf{K_s} = k_s\phi\hat{\mathbf{n}}$ and $\Delta k_d = k_p - k_s - k_i$. Substituting equation 3.1 into equation 4.12 gives:

$$I_s(z) = \frac{2\hbar\omega_s^2\omega_i d_{eff}^2 I_p z}{\pi^3\varepsilon_0 c^3 n_s n_i n_p \Delta k_d^2 \Lambda} [1 - exp(-\Delta k_d^2 \sigma_z^2)] d\mathbf{K_s} d\omega_s. \tag{4.13}$$

Equation 4.13 shows that the intensity of SPDC noise increases linearly with the propagation distance. Therefore,

$$dI_s = \frac{2\hbar\omega_s^2\omega_i d_{eff}^2 I_p}{\pi^3\varepsilon_0 c^3 n_s n_i n_p \Delta k_d^2 \Lambda}[1 - exp(-\Delta k_d^2\sigma_z^2)]d\mathbf{K_s}d\omega_s dz. \tag{4.14}$$

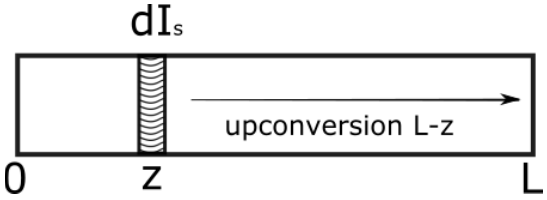

FIGURE 4.8: The USPDC process is split into two steps: the photon generated in the slab of dz due to the SPDC process is upconverted when it passes through the rest of the nonlinear crystal.

As shown by figure 4.8, the SPDC noise dI_s generated at position z will be upconverted when it goes through the remaining part of the crystal. Thus:

$$dI_{up}(z) = \frac{\omega_{up}}{\omega_s} dI_s \eta_{L-z}(\phi, \lambda_s) \tag{4.15a}$$

$$= \frac{2\hbar\omega_{up}\omega_s\omega_i d_{eff}^2 I_p}{\pi^3\varepsilon_0 c^3 n_s n_i n_p \Delta k_d^2 \Lambda}[1 - exp(-\Delta k_d^2\sigma_z^2)]\eta_{L-z}(\phi, \lambda_s)d\mathbf{K_s}d\omega_s dz, \tag{4.15b}$$

where $\eta_{L-z}(\phi, \lambda_s)$ is the upconversion efficiency as a function of λ_s and ϕ. Considering that only the IR photon fulfilling the QPM condition can be upconverted efficiently, λ_s and ϕ can be treated as dependent. Therefore, η_{L-z} can be approximated as:

$$\eta_{L-z}(\phi, \lambda_s) = \eta_{L-z}(\phi)\delta(\Delta k_{up} - 2\pi/\Lambda = 0) \tag{4.16a}$$

$$= sin^2(\sqrt{\frac{P_p}{P_{max}(L_{eff})}}\frac{\pi}{2})\delta(\Delta k_{up} - 2\pi/\Lambda = 0), \tag{4.16b}$$

where $P_{max}(L_{eff})$ is given by equations 2.11, where L is replaced by L_{eff} [82]:

$$L_{eff} = \begin{cases} L - z, \phi < \tan^{-1}(2\omega_0/(L-z)) \\ 2\omega_0/\tan(\phi), \phi \geq \tan^{-1}(2\omega_0/(L-z)). \end{cases} \tag{4.17}$$

substituting equations 4.16 into equations 4.15 gives:

$$I_{up} = \frac{2\hbar\omega_{up}\omega_s\omega_i d_{eff}^2 I_p k_s^2}{\pi^3\varepsilon_0 c^3 n_s n_i n_p \Delta k_d^2 \Lambda}[1 - exp(-\Delta k_d^2\sigma_z^2)] \cdot \int_L \int_{\Omega(L_{eff},\phi)} sin^2(\sqrt{\frac{P_p}{P_{max}(L_{eff})}}\frac{\pi}{2})\Delta\omega_s(L_{eff}, \phi)d\Omega dz, \tag{4.18}$$

where $\omega_s(L_{eff}, \phi)$ and $\Omega(L_{eff}, \phi)$ are the acceptance bandwidth and the acceptance solid angle of the upconversion, respectively. Equation 4.18 can be used for the calculation of the USPDC noise.

SHG-SPDC Noise

Similar to the USPDC process, the SHG-SPDC is also a two-step parametric process. It can be a noise source for the short-wavelength-pumped UCD potentially. Its Feynman diagram is shown in figure 2.10b. Figure 4.9a and 4.9b represent the spectral diagram and the k-vectors of the SHG-SPDC process, respectively.

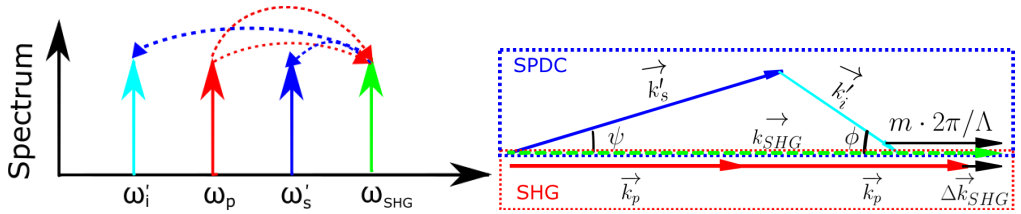

(a) (b)

FIGURE 4.9: (a) Spectral diagram and (b) k-vectors for the SHG-SPDC process in the PPLN crystal of a UCD.

As the first step of SHG-SPDC, the SHG process is non-phase matched, so its intensity is a few orders of magnitude lower than that of the pump field. In the experiment, the typical power level of SHG is $\sim$ 100 µW when a 25-mm long PPLN is pumped by a $\sim$ 100 W 1064 nm laser. In contrast, as the second step, the SPDC process is quasi-phase-matched. Therefore, the wavelength of the SPDC photon is decided by the QPM condition, and it is different from that of the upconverted signal in general. Note that the effect of SPDC process on the SHG field can still be neglected since the efficiency of SPDC is very low due to the low intensity of the SHG field, even though the SPDC process here is quasi-phase-matched.

Starting for equation 2.7.11 in [46]:

$$\frac{dE_{SHG}}{dz} = K_{SHG} g(z) e^{-i\Delta k_{SHG} z}, \tag{4.19a}$$

where

$$K_{SHG} = \frac{i\omega_{SHG} d_{eff}}{n_{SHG} c} |E_p|^2. \tag{4.19b}$$

The intensity of the SHG at position z is:

$$I_{SHG}(z) = 2n_{SHG} c\epsilon_0 |E_{SHG}|^2 \tag{4.20a}$$

$$= 2n_{SHG} c\epsilon_0 |K_{SHG}|^2 | \int_0^z g(z') \exp(i\Delta k_{SHG} z') dz' |^2 \tag{4.20b}$$

$$= \frac{\omega_{SHG}^2 d_{eff}^2}{2n_{SHG} n_p^2 c^3 \epsilon_0} I_P^2 |\widetilde{g}(\Delta k_{SHG})|^2 \tag{4.20c}$$

$$= \frac{\omega_{SHG}^2 d_{eff}^2 z}{n_{SHG} n_p^2 c^3 \epsilon_0 \Delta k_{SHG}^2 \Lambda} I_P^2 [1 - exp(-\Delta k_{SHG}^2 \sigma_z^2)]. \tag{4.20d}$$

Apparently, the intensity of the SHG increases linearly with z. Therefore, the field amplitude of SHG can be assumed as:

$$E_{SHG}(z) = \alpha\sqrt{z}, \tag{4.21a}$$

where

$$\alpha^2 = \frac{\omega_{SHG}^2 d_{eff}^2}{2n_{SHG}^2 n_p^2 c^4 \epsilon_0^2 \Delta k_{SHG}^2 \Lambda} I_P^2 [1 - exp(-\Delta k_{SHG}^2 \sigma_z^2)]. \tag{4.21b}$$

The SPDC process pumped by the SHG field fulfils the QPM condition. Therefore, equations 2.5 become:

$$\frac{dE_s'}{dz} = \frac{2i\omega_s' d_{eff}}{n_s' c} E_{SHG}(z) E_i'^* \tag{4.22a}$$

$$\frac{dE_i'}{dz} = \frac{2i\omega_i' d_{eff}}{n_i' c} E_{SHG}(z) E_s'^*, \tag{4.22b}$$

where E_s' and E_i' represent the signal and the idler fields, respectively. The symbol $'$ here is to distinguish it from the SPDC process in the USPDC process.

Based on equations 4.21 and 4.22, $E_s'(z)$ has the following form:

$$\frac{dE_s'^2}{d^2 z} = \frac{1}{2z}\frac{dE_s'}{dz} + \gamma z E_s', \tag{4.23a}$$

where

$$\gamma = \frac{4\omega_s' \omega_i' d_{eff}^2}{n_s' n_i' c^2} |\alpha|^2. \tag{4.23b}$$

Equation 4.23a has a general solution as:

$$E_s'(z) = C_1 \sinh(\frac{2}{3}\sqrt{\gamma} z^{\frac{3}{2}}) + C_2 \cosh(\frac{2}{3}\sqrt{\gamma} z^{\frac{3}{2}}). \tag{4.24}$$

Considering the system has the following initial conditions:

$$I_s'(0) = 0 \tag{4.25a}$$

$$I_i'(0) = I_{i0}, \tag{4.25b}$$

where I_{i0} is given by equation 2.7. I_s' can be solved as:

$$I_s'(z) = \frac{\omega_s' \omega_i'^2 n_i'^2 \hbar \psi}{4\pi^2 c^2} \sinh^2(\frac{2}{3}\sqrt{\gamma} z^{\frac{3}{2}}) d\omega_i' d\psi. \tag{4.26}$$

Equation 4.26 is used for the SHG-SPDC calculation.

Upconverted Thermal Radiation

When the UCD works in the MIR ($3 \sim 5\,\mu m$) region, the upconverted thermal radiation becomes the primary noise source [41]. In order to calculate its corresponding noise contribution, the crystal is treated as a thermal radiation source, its spectral radiance with one polarization state is [83]:

$$dI_{Thermal} = \frac{\alpha_{crystal} c^2 h n_s^2 dz d\lambda_s d\Omega}{\lambda_s^5} \frac{1}{exp(hc/\lambda_s k_B T) - 1}, \tag{4.27}$$

where $\alpha_{crystal}$ is the absorption coefficient for the nonlinear crystal, $d\Omega$ is the solid angle from which to collect the $dI_{Thermal}$. Following the same strategy for the USPDC

calculation as shown in figure 4.8,the upconverted thermal noise is:

$$dI_{upThermal} = \frac{\omega_{up}}{\omega_s} dI_{Thermal}(z)\eta_{L-z}(\phi,\lambda_s) \tag{4.28a}$$

$$= \frac{\omega_{up}\alpha_{crystal}chn_s^2}{2\pi\lambda_s^4}\frac{1}{exp(hc/\lambda_s k_B T)-1}\eta_{L-z}(\phi,\lambda_s)dzd\lambda_s d\Omega. \tag{4.28b}$$

Thus,

$$I_{upThermal} = \frac{\omega_{up}\alpha_{crystal}chn_s^2}{2\pi\lambda_s^4}\frac{1}{exp(hc/\lambda_s k_B T)-1} \cdot \int_L \int_{\Omega(L_{eff},\phi)} sin^2\left(\sqrt{\frac{P_p}{P_{max}(L_{eff})}}\frac{\pi}{2}\right)\Delta\lambda_s(L_{eff},\phi)d\Omega dz. \tag{4.29}$$

4.2.3 Experimental Setup

A single-pass upconversion system is built in order to analyze the noise generation process in the short-wavelength-pumped UCD experimentally. Figure 4.10 shows the experimental setup. A single-frequency, CW Yb-fibre laser (YLR-30-1064-LP-SF,

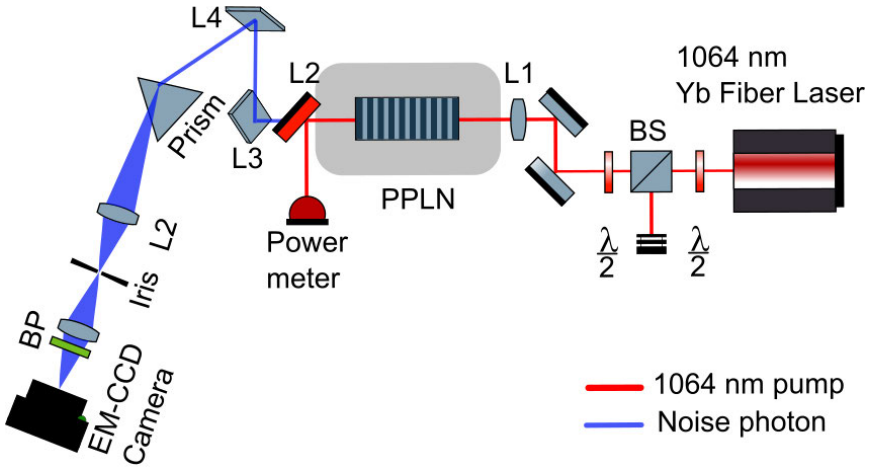

FIGURE 4.10: Single-pass, short-wavelength-pumped UCD for the noise investigation.

IPG Photonics) with a maximum output power of 30 W is used as the 1064 nm pump for the upconversion. The collimated 1064 nm beam out of the fibre laser is focused by a lens (L1, $f = 200$ mm) into a PPLN crystal with a beam diameter of $2\omega_0 = 95\,\mu$m. Afterwards, the 1064 nm pump beam is reflected by M1 and monitored by a power meter. Meanwhile, the noise photon passes through M1 partially and is converted into the p-polarization state with respect to the working surface of the prism by a periscope (M2, M3). On the image plane of L2, an iris is used to filter out the remaining 1064 nm pump and the 532 nm SHG. A bandpass filter is placed before an EM-CCD camera, which is used to measure the amount of noise photon. In order to use the full dynamic range of the camera, the integration time is selected from 3 sec to 1 min according to the intensity of the noise. The PPLN crystal is mounted into a PPLN oven with the ability of temperature tuning.

Three different PPLN crystals are used in this experiment, and the proper band-pass filters are applied accordingly. The experimental parameters will be specified for the particular measurements in the following section.

4.2.4 Results

4.2.4.1 NIR Detection with poling periods of $\Lambda = 12\,\mu m$ and $\Lambda = 12.69\,\mu m$

Firstly, a 40-mm long PPLN crystal with two channels of $\Lambda = 12\,\mu m$ and $\Lambda = 12.69\,\mu m$ is placed into the PPLN oven, the noise photon from two channels is measured separately. During the measurement, a bandpass filter with $\lambda_c = 625\,nm$ and $\Delta\lambda_{FWHM} = 50\,nm$ is used to remove the noise outside the spectrum of interest. Figure 4.11a and 4.11b show the images taken by the EM-CCD camera while the temperature of the crystal is kept at 50 °C. Due to the dispersion caused by the prism, the image suffers from astigmatism, but it does not affect the dark-count rate (DCR) measurement since only the total noise count is used here.

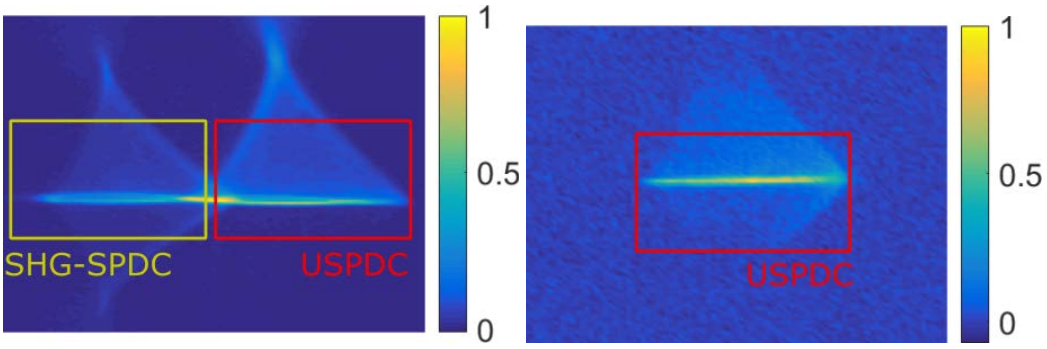

(a) (b)

FIGURE 4.11: Image taken by the camera when the channels of (a) $\Lambda = 12\,\mu m$ and (b) $\Lambda = 12.67\,\mu m$ are used. The temperature of the PPLN crystal is $T = 50\,°C$.

In this experiment, the wavelength of the IR signal under detection is between $1.55 \sim 1.65\,\mu m$. According to equation 4.27, the thermal radiation in this spectral range is small enough to be neglected. Therefore, only the USPDC and the SHG-SPDC are investigated here. According to the QPM condition, the central wavelength of the SHG-SPDC and the USPDC noise can be calculated as $\lambda_s' = 605\,nm$ and $\lambda_{up} = 634.9\,nm$, respectively. Therefore, the noise can be separated spatially by the prism, which results in two diamond-shape patterns in figure 4.11a ($\Lambda = 12\,\mu m$). In contrast, figure 4.11b ($\Lambda = 12.69\,\mu m$) has one diamond-shape pattern caused by the USPDC process only, and its wavelength is $\lambda_{up} = 646.7\,nm$.

Figure 4.12a shows the wavelength of USPDC (λ_{up}) and SHG-SPDC (λ_s') as a function of the temperature of the PPLN crystal when a 1064 nm laser is chosen as the pump. Generally, λ_{up} and λ_s' are different from each other, this is also the reason why two diamond-shape patterns in figure 4.11a are separate spatially. In other words, the noise from the SHG-SPDC process can be removed easily. However, two wavelengths can be the same in a particular condition (i.e. the black dot in figure 4.12a). From the perspective of the UCD, it will suffer from higher background noise if the UCD works in this condition.

The DCR due to the SHG-SPDC process as a function of the pump power is shown in figure 4.12b. There is a significant deviation between the experimental result (blue circle) and the theoretical one given by equation 4.26 when the pump power is high ($P_p > 15\,W$). Meanwhile, figure 4.12c and 4.12d are the USPDC noise count with different pump power. The theoretical results are given by equation 4.18. The deviation between the experimental and the theoretical results can be neglected.

In order to further investigate the properties of USPDC and SHG-SPDC process, the power of the 1064 nm pump is fixed at 22 W while the temperature of the PPLN

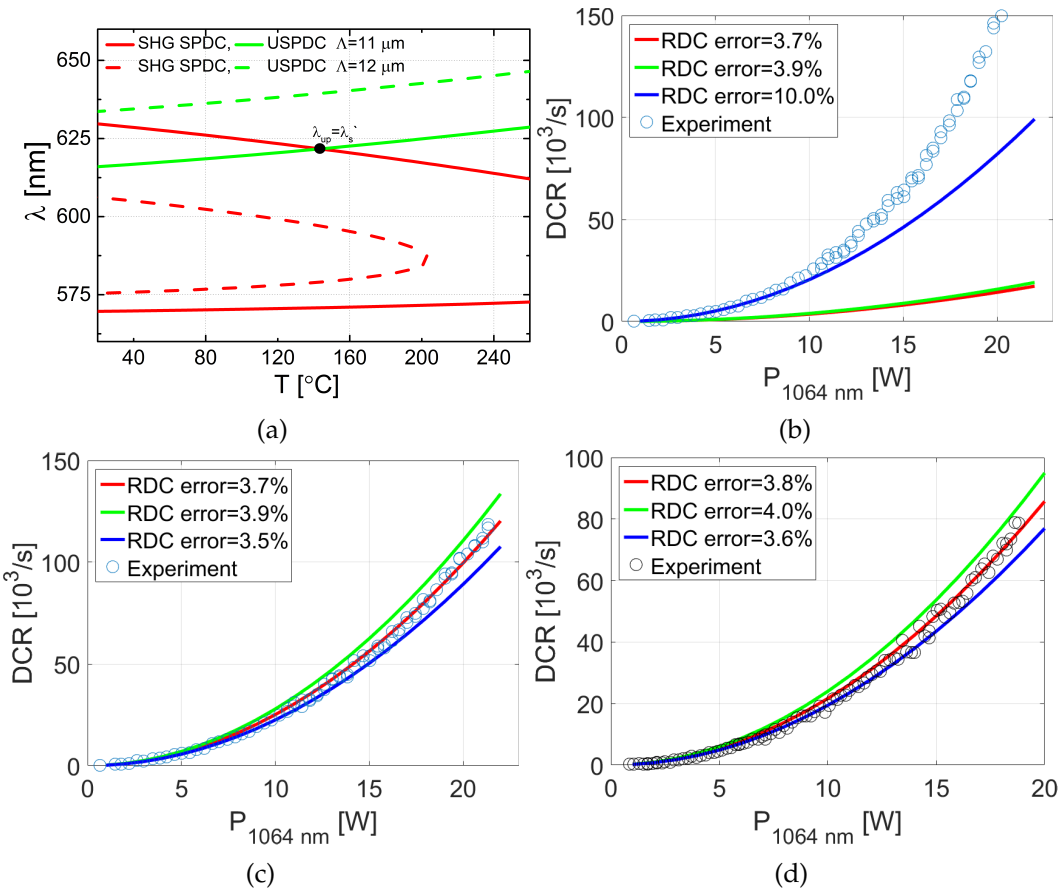

FIGURE 4.12: (a) λ (λ_{up} and λ_s') as a function of T given by the collinear QPM condition for the USPDC (green) and the SHG-SPDC (red) processes. DCRs due to (b) the SHG-SPDC and the (c) USPDC process versus the 1064 nm power when the poling period is $\Lambda = 12\,\mu$m. (d) DCR due to the USPDC process with the poling period of $\Lambda = 12.69\,\mu$m. The blue circles represent the measurement results, and the hard lines are the simulation results based on the corresponding models. The other parameters used in the simulations are: $\omega_0 = 48\,\mu$m, $\lambda_p = 1064\,$nm, $T = 50\,^\circ$C and $L = 40\,$mm.

crystal is increased gradually from 50 °C to 160 °C. Figure 4.13a shows the DCR as a function of temperature. Figure 4.13b shows the calculated λ under different T. The red curve indicates that the bandpass filter ($\lambda_c = 625\,$nm, $\Delta\lambda_{FWHM} = 50\,$nm) starts blocking the noise photon induced by the SHG-SPDC process when $T > 100\,^\circ$C, because λ_s' is smaller than 600 nm in this case but the transmission window of the filter is $600 \sim 650\,$nm. Thus, the DCR due to the SHG-SPDC process is close to 0 when $T > 100\,^\circ$C.

The inset plot of figure 4.13a clearly indicates that the change of temperature has a larger impact on the SHG-SPDC process than on the USPDC process. This can be explained by comparing equation 4.12 and 4.20: the SPDC (in the USPDC process) and the SHG (in the SHG-SPDC process) are both phase-mismatched, and their intensities are proportional to $|\widetilde{g}(\Delta k)|^2$. However, only the average of $|\widetilde{g}(\Delta k_d)|^2$ can affect the intensity of USPDC because the SPDC is broadband. On the contrary, the SHG process is narrow-band since the linewidth of the 1064 nm pump is very narrow. Thus, the intensity of SHG is decided by the instantaneous value of $|\widetilde{g}(\Delta k_{SHG})|^2$ instead of its average. Considering the value of Δk_{SHG} changes during the temperature T tuning, the fluctuation of $|\widetilde{g}(\Delta k_{SHG})|^2$ leads to the power fluctuation of SHG, which results in the fluctuation of the noise count (SPDC in the SHG-SPDC process)

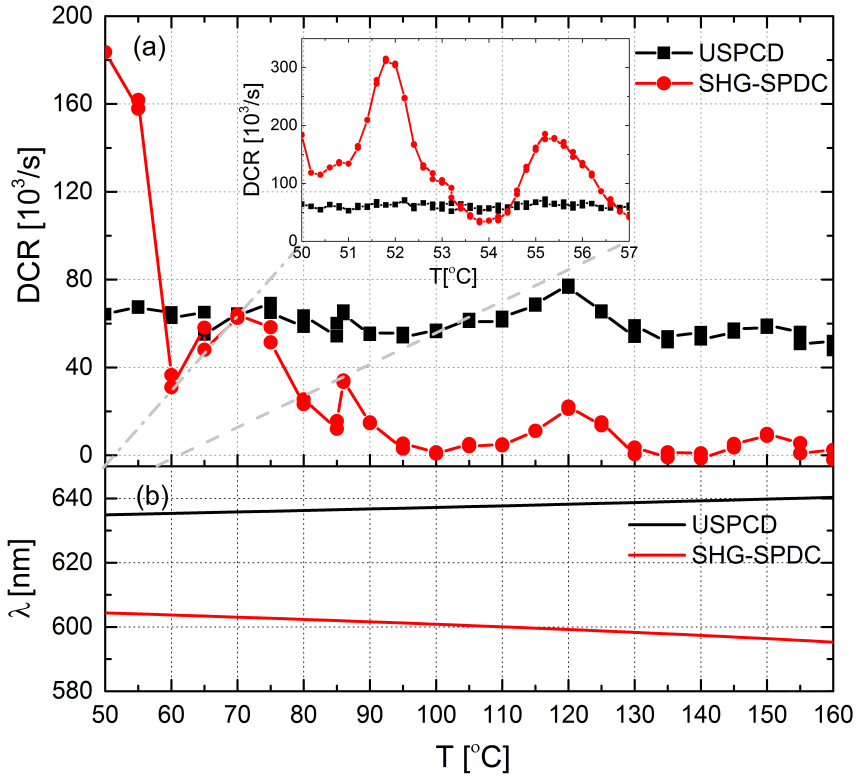

FIGURE 4.13: (a) Measured DCRs caused by the USPDC (black) and the SHG-SPDC (red) processes versus the temperature of the PPLN crystal, the inset figure shows the fine temperature tuning in the range of 50 $\sim$ 57 °C. (b) λ (λ_{up} and λ_s') versus T given by the collinear QPM condition.

effectively. In fact, the power fluctuations of the green light (SHG) is observable during the temperature tuning in the experiment.

4.2.4.2 MIR Detection with poling periods of $\Lambda = 22\,\mu m$ and $\Lambda = 23\,\mu m$

The noise photon due to the upconverted thermal radiation and the USPDC cannot be separated experimentally. However, the noise contribution from the upconverted thermal radiation can still be investigated when it becomes the dominant noise source. According to equation 4.27, the intensity of the thermal radiation becomes larger with the increase of IR wavelength. Thus, the MIR region (3 $\sim$ 5 µm) is chosen as the spectral region of interest by using a 20-mm long PPLN with poling periods of $\Lambda = 22\,\mu m$ and $\Lambda = 23\,\mu m$ in the following experiment. According to the principle of energy conservation, the wavelength of the upconverted signal is between 750 $\sim$ 850 nm in this case. Accordingly, a new bandpass filter with $\lambda_c = 800\,nm$ and $\Delta\lambda_{FWHM} = 100\,nm$ is used here.

Figure 4.14 shows the images taken by the camera. Similar to figure 4.11a, the images in figure 4.14 all have two separate patterns, which correspond to the 3rd order SHG-SPDC and the upconverted thermal radiation/USPDC process, respectively. The k-vectors diagram of the 3rd order SHG-SPDC process is given by figure 4.9b with $m = 3$. To be more specific, the SPDC following the SHG process is 3rd order quasi-phase-matched. According to equation 2.17b, d_{eff} for the SPDC process decreases by a factor of 3, so the intensity becomes 9 times lower than the 1st order one when working in the same conditions. This is also the reason why its intensity is relatively low in figure 4.14.

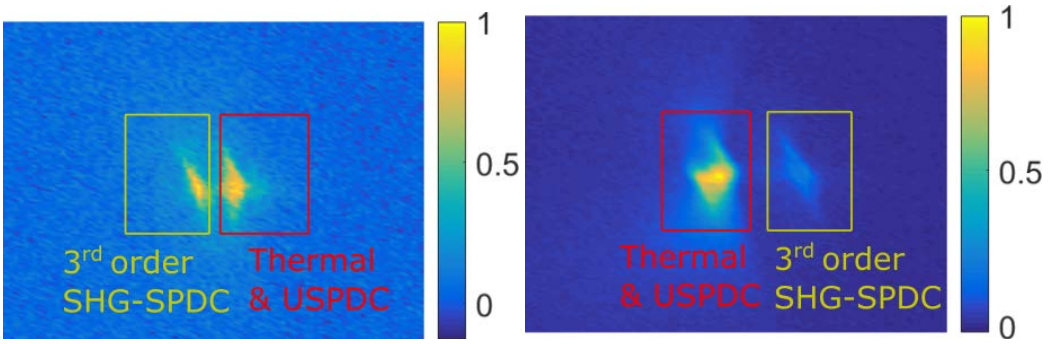

(a) (b)

FIGURE 4.14: Image taken by the camera when the channels of (a) $\Lambda = 22\,\mu m$ and (b) $\Lambda = 23\,\mu m$ are used. The temperature of the PPLN crystal is $T = 50\,°C$.

Figure 4.15a shows λ (λ_{up} and λ_s') as a function of T calculated by the QPM condition for the upconversion and the 3rd order SHG-SPDC process. Similar to the black dot in figure 4.12a, the wavelength degeneration ($\lambda_{up} = \lambda_s'$) also happens for the condition of $\Lambda = 22\,\mu m$ at $T = 165\,°C$ (black dot in figure 4.15a). Apparently, the UCD will suffer higher background noise in this case. Figure 4.15b shows the DCR given by the experimental and the theoretical results when the UCD is pumped with the same pump power ($P_p = 22\,W$) but at different working temperatures. The blue circles indicate the total measured noise count due to both USPDC and upconverted thermal radiation. The red and the green curves are the theoretical results, which represent the noise sources due to the upconverted thermal radiation and the USPDC, respectively. Clearly, the thermal part is the dominant noise source in the UCD here.

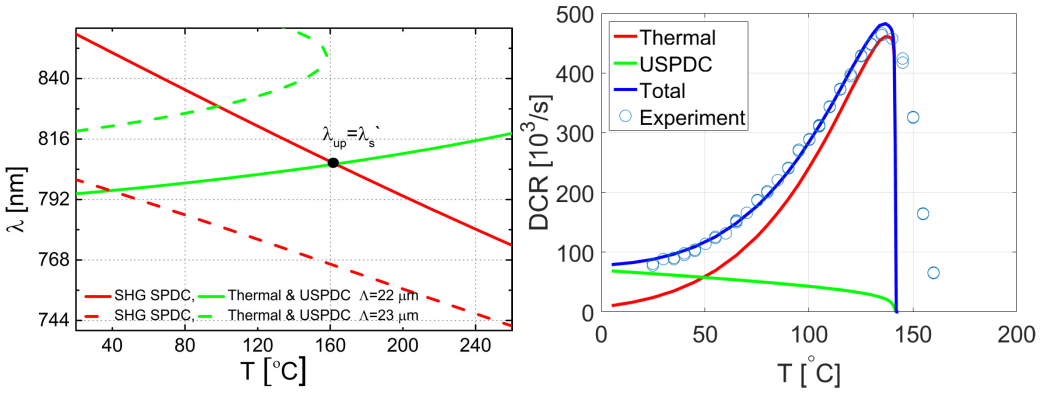

(a) (b)

FIGURE 4.15: Calculated (a) λ (λ_{up} and λ_s') and (b) DCR as a function of temperature T. The parameters used in the simulations are: $P_p = 22\,W$, $\omega_0 = 48\,\mu m$, $\lambda_p = 1064\,nm$, $L = 20\,mm$ and $\sigma_z/\Lambda = 7\,\%$.

4.2.5 Conclusion

The noise sources of the short-wavelength-pumped UCD: USPDC, SHG-SPDC and the upconverted thermal radiation were investigated thoroughly in this study. Especially, the SHG-SPDC process was identified, to our best knowledge, as a new potential noise source for UCD for the first time. In general, the wavelength of the noise

photon due to the SHG-SPDC process is different from that of the upconversion signal ($\lambda_s' \neq \lambda_{up}$). Therefore, it can be removed by using a bandpass filter accordingly. But for some particular cases (e.g. the cross points in figure 4.12a and figure 4.15a), it cannot be removed due to the degeneration of the noise wavelength. Thus the SHG-SPDC process can increase the background noise of a UCD significantly. From the perspective of UCD design, the noise due to the SHG-SPDC process can be avoided by choosing the correct combination of poling period Λ, working temperature T and bandpass filters.

The noise from the USPDC and the upconverted thermal radiation have the same wavelength as the upconverted signal. An ultra-narrow bandpass filter (e.g. volume Bragg grating) is helpful for noise reduction, but it is impossible to remove these noise sources completely. However, these two noise sources have different dependencies on the working conditions. The USPDC noise strongly depends on the pump power and the poling error of the crystal. On the contrary, the upconverted thermal radiation is mainly affected by the λ_s and the working temperature. Figure 4.16 shows the noise count due to the USPDC and the upconverted thermal radiation at different detection wavelength. Apparently, the USPDC is the primary noise source when $\lambda_{IR} < 3.5\,\mu m$ and the upconverted thermal radiation becomes the dominant one when $\lambda_{IR} > 3.5\,\mu m$. In general, using a crystal with less poling error and working at low temperature is a good strategy for noise reduction.

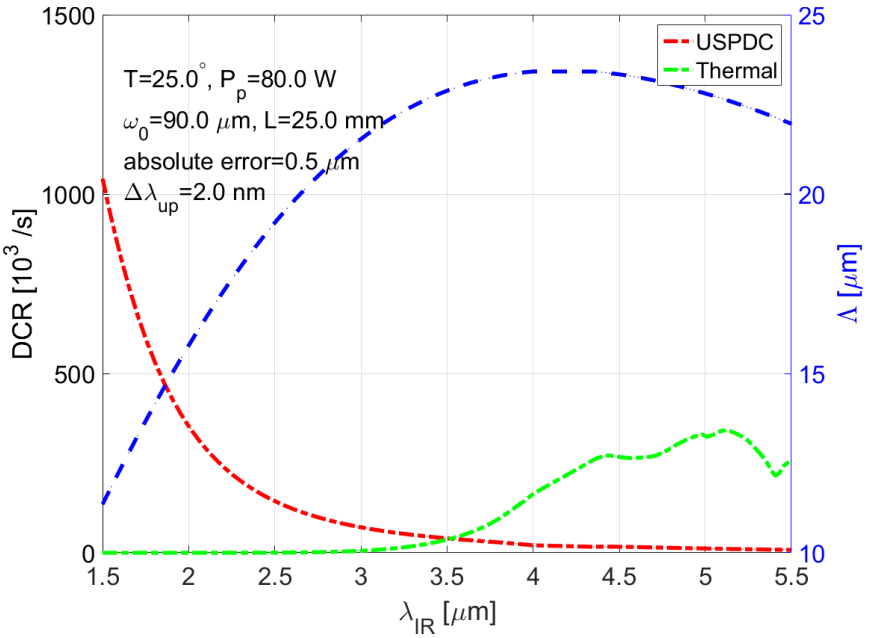

FIGURE 4.16: DCR due to the USPDC (red) and the upconverted thermal noise (green) as a function of the wavelength of IR signal. In the simulation, the temperature of the crystal is set as constant $T = 25\,°C$, and the poling period Λ of the PPLN crystal is calculated for the different λ_{IR} based on the collinear QPM condition (blue dash line). The parameters used in the simulation are: $P_p = 80\,W$, $\omega_0 = 90\,\mu m$, $\lambda_p = 1064\,nm$, absolute poling error $\sigma_z = 1\,\mu m$, the central wavelength of the bandpass filter corresponds to the wavelength of the upconverted signal, $\Delta\lambda_{up} = 2\,nm$ and $L = 25\,mm$.

This physical model provides theoretical support for the quantitative analysis of UCD noise when the scheme of short-wavelength pumping is used. But it is worth pointing out that the model for the SHG-SPDC calculation may have a large error compared with the measurement result, which is caused by the deviation between

the average and the instance value of $|\widetilde{g}(\Delta k_{SHG})|^2$. When the effect of the SHG-SPDC is removed by choosing the proper design, the noise power can be calculated by combining the contributions from the USPDC and the upconverted thermal radiation together. Afterwards, the NEP of the whole detection system can be calculated by considering the upconversion efficiency and the performance of the detector (for the upconverted signal) in total.

4.3 Upconverted SRS Noise of the Long-wavelength-pumped UCD

In this thesis, a UCD for atmospheric lidar application is designed and built based on the scheme of short-wavelength pump. Four reasons for choosing this specific design have been listed in Chapter 3 (page 25). Moreover, Our system shows a better performance than the direct InGaAs detector in a real lidar measurement (in Chapter 5), which proves it to be a promising technology for the future lidar application. However, the DCR of our UCD is still relatively large (DCR $\sim 1 \times 10^4$/s) even though several strategies are implemented for noise reduction. Apparently, the high DCR of the UCD limits the fields of application such as quantum network where a low DCR is highly demanded [84]. Meanwhile, a long-wavelength-pumped UCD has the potential of achieving ultra-low background noise since it can remove the USPDC noise source fundamentally. The waveguide-based, long-wavelength-pumped UCD for IR signal detection in the telecom band has been demonstrated in [25, 26], wherein the DCR is in the level of 1×10^2/s with an internal upconversion efficiency $\eta_{up} > 80\,\%$. However, the waveguide-based UCD has a very small étendue, which limits its ability of signal collection. On the other hand, a UCD based on the bulk crystal has a relatively large étendue, but it has seldom been demonstrated with an intracavity-enhanced long-wavelength-pumped system. In order to investigate the potential of the long-wavelength-pumped upconversion technology, a UCD based on a 2 µm solid-state laser is built, and its noise properties are studied accordingly.

4.3.1 Theory

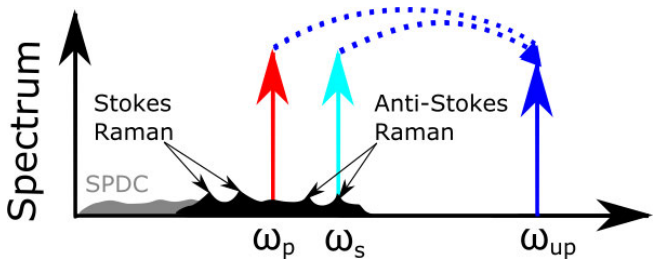

FIGURE 4.17: The spectral diagram of the upconverted SRS process. The SPDC process is also included.

Upconverted SRS has been proved to be the main noise source in the long-wavelength-pumped UCD [25, 80, 85]. Figure 4.17 shows a spectral diagram of the noise generation for a long-wavelength-pumped UCD, the upconverted SRS can be separated into two steps: 1) The high-intensity pump inside the crystal induces a broadband noise floor due to the anit-Stokes Raman scattering effect. 2) The noise photon located in the acceptance bandwidth ($\sim \omega_s$) of the upconversion process can be further

upconverted and becomes the upconverted SRS noise. It is worth pointing out that the high-intensity pump also induces broadbanded SPDC noise, but since the wavelength of SPDC is smaller than λ_s, it contributes no noise photon to the upconversion anymore, i.e. the USPDC process is removed fundamentally here.

The noise power due to the anti-Stokes Raman scattering can be simplified as [25, 46]:

$$dP_{anti-Stokes} = CP_p\rho \exp(-\hbar\Delta\omega/k_BT)g_L(\Delta\omega)\frac{d\sigma}{d\Omega}\Delta\omega d\Omega dz, \tag{4.30}$$

where C is a constant, $\Delta\omega$ is the angular frequency shift of the Raman scattering, ρ is the number density of unit cells, $g_L(\Delta\omega)$ is the Raman lineshape function and $d\sigma/d\Omega$ is the differential cross section. Considering the power of SRS is proportional to the propagation distance (similar to equation 4.14), the procedure for the calculation of upconverted SRS noise is similar to that of the USPDC process: by substitute equation 4.30 into equation 4.15b.

4.3.2 Experimental Setup

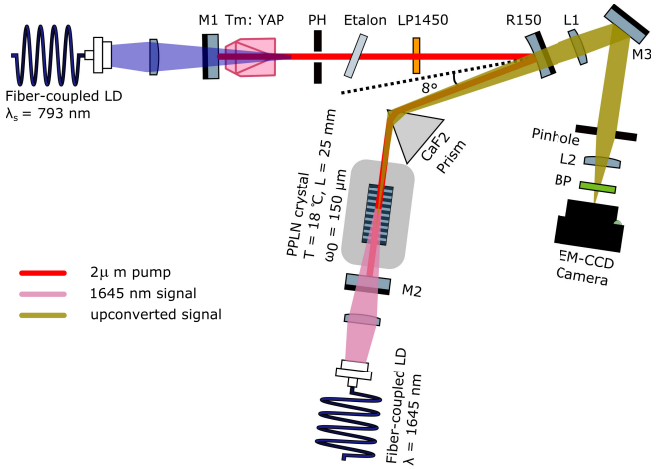

FIGURE 4.18: Scheme of the long-wavelength-pumped, intracavity-enhanced UCD for the noise investigation. When the channel of $\Lambda = 26.05\,\mu m$ is used for the upconversion, $\lambda_{up} = 901\,nm$ and the bandpass filter has $\lambda_c = 900\,nm$ and $\Delta\lambda_{FWHM} = 10\,nm$. When the channel of $\Lambda = 23.70\,\mu m$ is used , $\lambda_{up} = 852\,nm$ and the bandpass filter has $\lambda_c = 850\,nm$ and $\Delta\lambda_{FWHM} = 40\,nm$.

Figure 4.18 shows the experimental setup for the noise investigation of a long-wavelength-pumped UCD. A diode-pumped Tm:YAP laser operating near 2 µm is the backbone of the UCD. The cavity mirrors (M1, M2 and R150) are all HR coated for 2 µm, and the transmission of M1 is characterized as $T_{M1} = 2.86 \times 10^{-3}$ before the laser is used for upconversion. The leakage power $P_{leakage}$ from M1 is monitored during the noise measurement, the intracavity power can be calculated using the same strategy as introduced in Chapter 3 (page 31). An etalon and a CaF_2 prism are put inside the laser cavity in order to stabilize the central wavelength and also to decrease the linewidth of the 2 µm laser. A pinhole and a long-pass filter with $\lambda_{cut} = 1450\,\mu m$ are placed right after the laser crystal for the reduction of fluorescence generated inside the Tm:YAP crystal. A 25-mm long PPLN crystal with poling periods of $\Lambda = 23.70\,\mu m$ and $\Lambda = 26.05\,\mu m$ is used for the upconversion of IR signal at $\lambda_s = 1.48\,\mu m$ and $\lambda_s = 1.64\,\mu m$, respectively. The temperature of the PPLN is maintained at 18 °C and the beam waist of the 2 µm pump laser inside the PPLN

crystal is $\omega_0 \approx 75\,\mu m$. The upconverted signal (and the noise) passes through a 4f lens system consisting of L1 and L2. A pinhole with a diameter of 2.5 mm is placed on the Fourier plane to remove the noise. A fibre coupled LD (FPL1059S, Thorlabs) at $\lambda_s = 1.65\,\mu m$ is used as an IR source for the alignment. After passing through a bandpass filter, the noise photon is measured by an EM-CCD camera.

4.3.3 Results and Discussion

The central wavelength of the IR signal under detection, the acceptance angle and the acceptance bandwidth can be calculated based on the collinear QPM condition considering a 25-mm long PPLN at 18 °C is pumped with a 1.998 µm laser. The calculated results are summarized in table 4.2.

	λ_s [nm]	$\Delta\lambda_s$ [nm]	$\Delta\phi$ [mrad]
$\Lambda = 23.70\,\mu m$	1484.7	1.2	16.5
$\Lambda = 26.05\,\mu m$	1639.1	1.7	16.6

TABLE 4.2: Parameters of the upconversion

A proper IR source with a linewidth smaller than the acceptance bandwidth $\Delta\lambda_s$ is not available in our laboratory. The 1640 nm LD used in this experiment as shown in figure 4.18 has a relatively larger linewidth ($\Delta\lambda \approx 10\,nm$). The spectrum of the LD is shown in figure 4.19a, in which the multiple peaks indicate that the LD lases with multimode. Therefore, it is not possible to characterize the internal upconversion efficiency of the UCD experimentally. However, based on the calculation, the upconversion efficiency is expected $\eta_{up} = 16\,\%$ when the pump power is 50 W.

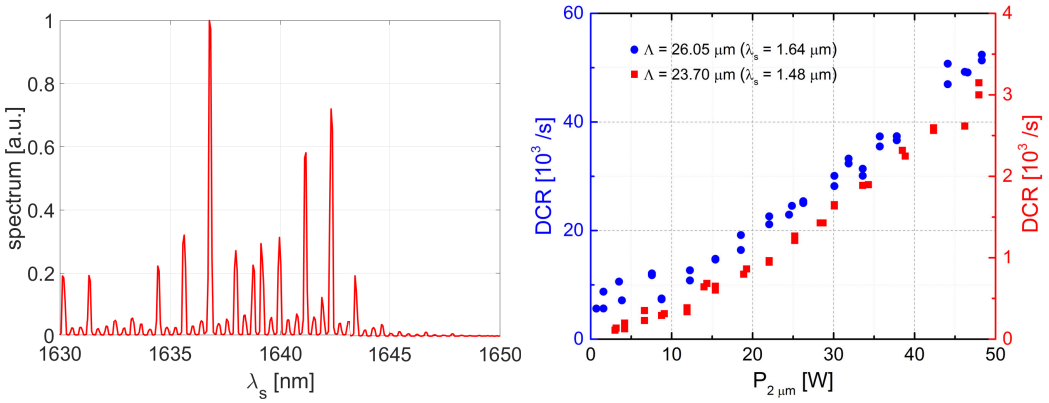

(a) (b)

FIGURE 4.19: (a) Spectrum of the IR source, (b) DCR as a function of pump power.

Figure 4.19b shows the DCR as a function of pump power. Apparently, the DCR increases linearly with respect to the pump power, which does not fit with the theory (it is expected to behave like figure 4.12c). It is believed due to the enlargement of the beam size caused by the thermal lensing effect in the laser crystal [86].

According to equation 4.30, parameters of working temperature T, frequency shift $\Delta\nu$, pump power P_p and the length of crystal (or waveguide) affect the intensity of Raman scattering together, all these parameters for several different UCDs are summarized in table 4.3. In addition, the quantum efficiency (η_{Si}) of Si based detectors used in different cases is also included in order to evaluate the DCR fairly. The normalized factor F_i is defined as $F_i = P_p L \eta_{Si}$.

The waveguide-based UCD has a DCR level of $\sim 1 \times 10^2$/s, which is almost 2 orders of magnitude lower than our experimental results (Bulk 1 and 2), this is mainly due to the large pump power P_p used in this experiment. Meanwhile, the DCR for the $\lambda_s = 1.65\,\mu m$ detection is around 18 times larger than that of $\lambda_s = 1.48\,\mu m$, which is caused by the larger $d\sigma/d\Omega$. The relative values of $d\sigma/d\Omega$ for

	T[°C]	$\Delta\nu$ [1/cm]	P_p [W]	L [mm]	$\eta_{detector}$	F_i/F_1	DCR [1×10^3/s]
Waveguide [80]	40	-917.3	0.215	52	52	1	2.79
Waveguide [85]	30	-1253	0.12	50	65	0.67	0.6
Waveguide [87]	38	-2971	0.085	48	70	0.49	0.045
Bulk 1, $\Lambda = 26.05\,\mu m$	20	-1059	50	25	8	17.2	50
Bulk 2, $\Lambda = 23.70\,\mu m$	20	-1763	50	25	16	34.4	3

TABLE 4.3: Parameter of the long-wavelength-pumped UCD

each case can be evaluated by comping DCR_i/F_i accordingly.

In summary, an intracavity-enhanced, long-wavelength-pumped UCD based on the bulk PPLN crystal was built in this experiment, and its background noise was measured at different conditions. The experimental result proved that the upconverted SRS is the primary noise source for the UCD, and the absolute DCR level of the UCD is $> 1 \times 10^3$/s. The work presented in this section is only a preliminary study on the upconverted SRS. It can be used for the estimation of DCR in the design of an UCD, but more experimental and theoretical investigations are needed for the understanding of the physical process in the long-wavelength-pumped UCD. It is highly recommended to use a single-pass scheme that is similar to that of figure 4.10 for the further investigation of the upconverted SRS noise in the future.

4.4 Pattern of USPDC and Noise Reduction

4.4.1 Introduction

The power of the USPDC noise generated in the short-wavelength-pumped UCD was discussed before, and its typical value is DCR $= 5 \times 10^5$/s when an IR signal at 1.5 µm is measured [72]. In some particular applications, the USPDC noise can be removed fundamentally by using a long-wavelength pumping scheme, which can lower the DCR to the level of $\sim 1 \times 10^2$/s that primarily originates from the upconverted SRS process [25, 80]. However, the scheme of long-wavelength pumping is impractical for the upconversion detection in the mid/far IR range, and its disadvantages have been listed in Chapter 3 (page 25). In particular, the DCR in the level of $\sim 1 \times 10^2$/s can only be achieved by using a waveguide-based UCD with a low-power pump ($\sim 100\,mW$). For a UCD based on the bulk crystal, a high pump power ($> 10\,W$) is needed in order to get a reasonably high upconversion efficiency. Considering the SRS noise is proportional to the pump power, the DCR in the bulk crystal based UCD will end up in the level of $\sim 1 \times 10^3$/s at least, which is also experimentally proved in the previous section. Thus, instead of implementing UCD based on the scheme of long-wavelength pump, the UCD with a short-wavelength pumping is a better choice, and more effort should be put on its noise reduction.

In this section, the first experimental and theoretical study of the spatial and spectral distribution of the USPDC noise when a short-wavelength pump is applied

in an upconversion single-photon detector is presented. A new physical model considering the non-collinear parametric process is developed in order to explain experimental observations. Furthermore, a novel yet simple method of using a spatial filter for DCR reduction is proposed by taking advantage of the spatially non-uniform intensity distribution and the relatively broadband spectrum of the noise. An experimental demonstration is performed showing 14 dB DCR reduction with only a 2.2 dB penalty for the signal.

The material present in this section (Section 4.4) can also be found in paper [88].

4.4.2 Spatial Distribution of USPDC Noise

A unique spatial distribution of the USPDC noise is first observed when the background noise of the intracavity pumped UCD is measured by an EM-CCD camera that has single-photon counting capability. This is a newly discovered phenomena that can be exploited for DCR suppression in upconversion detectors. Therefore, further experimental and theoretical investigations are performed.

Experiment

Figure 4.20 shows the experimental setup where the ring pattern of USPDC noise from a short-wavelength-pumped UCD is first discovered. More details of the UCD has been introduced in Chapter 3 (page 25). It is worth mentioning that the USPDC noise locates in the transmission window of the bandpass filter set in front of the camera. Three images of the ring pattern as shown in figure 4.20 are obtained using three different PPLN crystals at the same operating temperature $T = 50\,^{\circ}\mathrm{C}$. PPLN 1 has a length of 25 mm and a poling period of $\Lambda = 11.97\,\mu\mathrm{m}$. PPLN 2 and PPLN 3 are both 40-mm long with $\Lambda = 12\,\mu\mathrm{m}$. All three PPLN crystals have a lateral size of 1 mm $\times$ 1 mm. The ring patterns from these three crystals are different from each other. This suggests that it is the specific poling structure rather than the design parameters of each crystal that determines the distribution of the ring pattern. Additionally, the output of a 633 nm He-Ne laser is transmitted through the PPLN directly and no interference ring pattern is found. Thus, interference is ruled out as a mechanism for the ring pattern generation.

Figure 4.21 shows the USPDC ring pattern of PPLN 1 crystal operating at different temperatures. The diameter of the rings decreased with increasing temperature. The overlaying plot with the ring pattern at $\mathrm{T} = 40\,^{\circ}\mathrm{C}$ is calculated based on the non-collinear QPM condition and it shows the central wavelength λ_s of the signal as a function of the angle θ_{ext} described in figure 4.20. The length of the vertical bars included in the plot indicates the acceptance bandwidth ($\Delta\lambda_s \approx 0.52\,\mathrm{nm}$). The spectral content of the ring pattern at different position varies along the radius. The average intensity of the ring pattern is also found to vary with temperature, which is primarily due to the variation of the 1064 nm pump power inside the laser cavity with changing PPLN temperature.

Theory and Simulations

The RDC error in QPM devices (e.g. PPLN crystal) is the reason for the USPDC pattern. In the previous section (page 51), the total noise power due to the USPDC process was investigated experimentally, and the theoretical results given by the model had a good agreement with the experimental ones. However, the model is based on the pedestal effect, and it can only provide the averaging number. In order

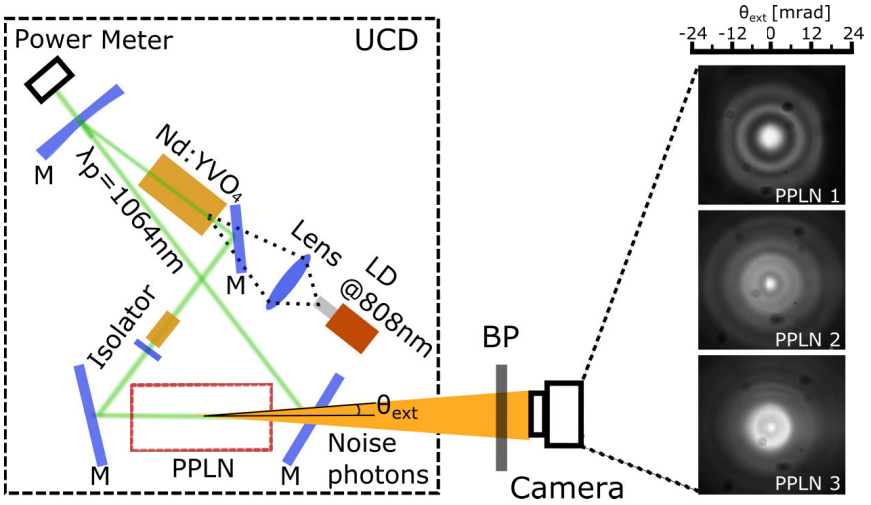

FIGURE 4.20: Experimental setup for the USPDC ring pattern observation and three images taken by the camera for three different PPLN crystals at the same operating temperature T = 50 °C. M, mirrors; LD, laser diode. The BP filter set contains a 600 nm long-pass filter, a 650 nm short-pass filter, and a bandpass filter with λ_c = 635 nm and $\Delta\lambda_{FWHM}$ = 10 nm. The scale on top of the images indicates the angle θ_{ext} corresponding to a lateral position on the image. Diffraction patterns caused by dust particles on the filter are visible on the image.

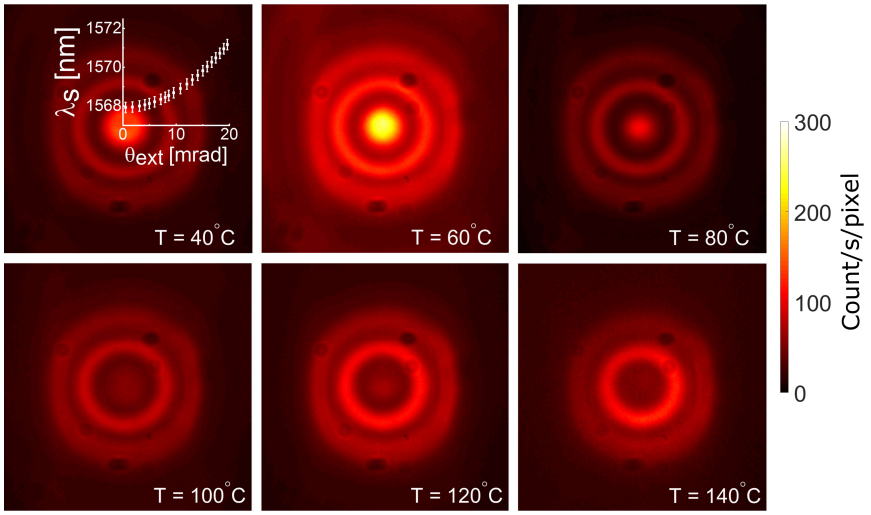

FIGURE 4.21: Intensity profiles of the USPDC noise for PPLN 1 crystal operating at different temperatures

to explain the angular distribution of USPDC noise photons that is observed in the experiment, a model involving the non-collinear interaction needs to be established.

The assumption used in the previous section is still valid. Figure 4.7b can still be used to demonstrate the k-vectors for the phase mismatched but parasitic SPDC process and the QPM upconversion process. Based on equations 2.4 and 2.5, the electric field E_j propagating along the z-direction is governed by the following differential

equations,

$$\frac{dE_s}{dz} = -K_s^* g(z) E_{up}^* e^{-i\Delta k_{up} z} + K_s g(z) E_i^* e^{i\Delta k_d z} \tag{4.31a}$$

$$\frac{dE_{up}}{dz} = K_{up} g(z) E_s^* e^{i\Delta k_{up} z} \tag{4.31b}$$

$$\frac{dE_i}{dz} = K_i g(z) E_s^* e^{i\Delta k_d z}, \tag{4.31c}$$

where

$$K_j = \frac{2i\omega_j d_{eff}}{n_s c} E_p \tag{4.31d}$$

$$\Delta k_{up} = k_p + k_s - k_{up} - (k_s - \frac{k_s^2}{k_{up}})\frac{\phi^2}{2} \tag{4.31e}$$

$$\Delta k_d = k_p - k_s - k_i + (k_s + \frac{k_s^2}{k_i})\frac{\phi^2}{2}. \tag{4.31f}$$

Δk_{up} and Δk_d are the phase mismatch of the upconversion and the downconversion, respectively. $g(z)$ is given by equation 2.16. The maximum upconversion efficiency is expected when the non-collinear QPM condition is fulfilled, i.e.

$$\Delta k_{up}(\lambda_s, \phi) = 2\pi/\Lambda. \tag{4.32}$$

According to the length L, poling period Λ and specified RDC error of PPLN 1, $g(z)$ is assigned with discrete values. Afterwards, E_s and E_{up} are solved numerically based on equation 4.31 for a given λ_s and ϕ. Figure 4.22 shows an example of the numerical calculation. As expected, the normally phase mismatched SPDC photons are broadband. Unlike the spectrum of the SPDC, the spectral coverage of USPDC photons is narrower with the central peak governed by the non-collinear QPM condition, i.e. the quasi-phase-matched upconversion process with the condition given by equation 4.32 determines where the USPDC photon count will be significant.

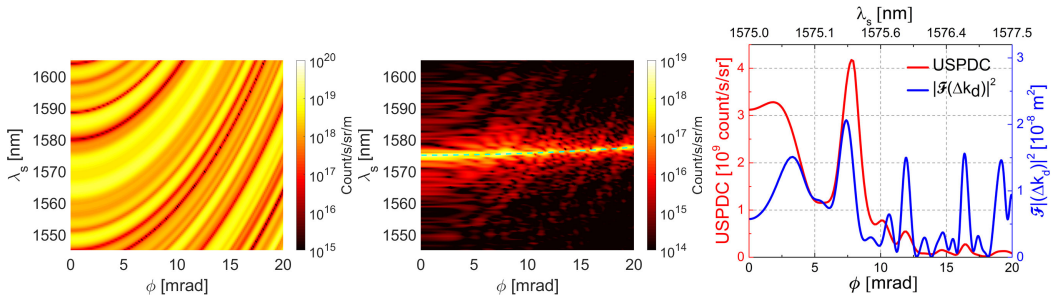

(a) (b) (c)

FIGURE 4.22: (a) SPDC and (b) USPDC given by the simulation results. (c) Angular profile of the USPDC noise and the corresponding spectrum $|\mathcal{F}(\Delta k_d)|^2$ of the simulated poling structure.

In the simulation, the following parameter settings are used: 1064 nm pump power $P_p = 100\,\mathrm{W}$, pump beam diameter $2\omega_0 = 400\,\mu\mathrm{m}$, PPLN length $L = 25\,\mathrm{mm}$, poling period $\Lambda = 11.97\,\mu\mathrm{m}$, $T = 66.7\,^\circ\mathrm{C}$ and the RDC error is 6 % with a Gaussian distribution. The red dash curve in figure 4.22c is the angular profile of the USPDC photon count rate obtained by integrating figure 4.22b over the λ_s axis (i.e. a range that, on the upconverted side, corresponds to the 635 ± 5 nm pass-band of

the filter used in the experiment), and the blue dash curve is the $|\mathcal{F}(\Delta k_d)|^2$ [89], where $\mathcal{F}(\Delta k_d)$ is the Fourier transform of $g(z)$, and Δk_d is given by equation 4.31 and 4.32. The strong correlation between these two curves indicates that the USPDC can be separated into SPDC and upconversion stages. The SPDC process is phase mismatched, but not negligible, and the profile of I_{SPDC} is decided by the specific poling structure with a corresponding $|\mathcal{F}(\Delta k_d)|^2$. The upconversion efficiency $\eta_{up}(\lambda_s, \phi)$ has the optimum values when equation 4.32 is satisfied. Assuming that the acceptance bandwidth and angle are small enough ($\Delta\lambda_s < 1\,\text{nm}$, $\Delta\theta < 1\,\text{mrad}$), the upconversion efficiency can be simplified as $\eta_{up}(\lambda_s, \theta) = \eta(\theta)\delta(\Delta k_{up} - 2\pi/\Lambda)$, where $\eta(\theta)$ is the upconversion efficiency considering the reduction of interaction length due to the non-collinear interaction [82]. Then, the power of USPDC can be written as:

$$P_{USPDC} \propto \int I_{SPDC}(\lambda_s, \theta)\eta(\lambda_s, \theta)d\lambda_s \tag{4.33a}$$

$$= \int I_{SPDC}(\lambda_s, \theta)\eta(\theta)\delta(\Delta k_{up} - 2\pi/\Lambda)d\lambda_s \tag{4.33b}$$

$$= \eta(\theta)I_{SPDC}(\Delta k_{up} = 2\pi/\Lambda). \tag{4.33c}$$

Thus, the angular profile of the USPDC power is mainly decided by the SPDC intensity profile combined with the quasi-phase-matched upconversion process.

By converting the angular distribution of the USPDC noise into a radial profile, the two-dimensional USPDC pattern with rotation symmetry is generated. Figure

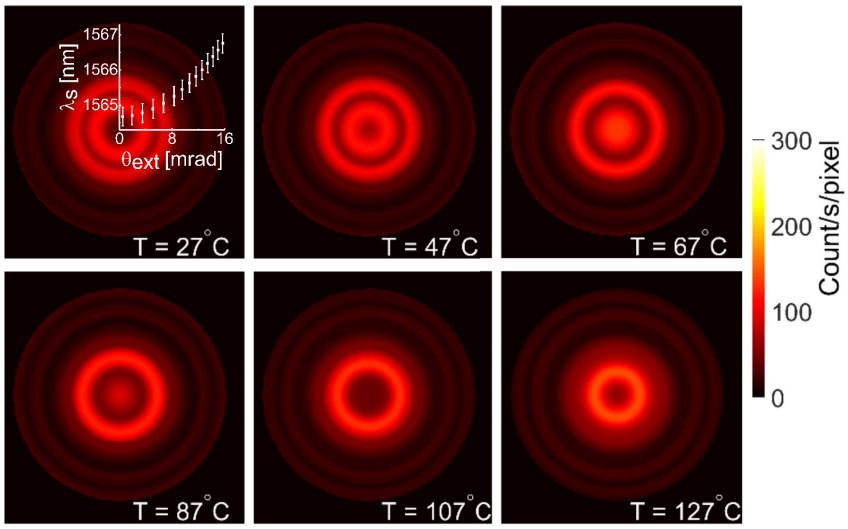

FIGURE 4.23: Simulation results showing the USPDC pattern using crystal parameters specified for PPLN 1 operating at different temperatures considering the 45 % (at 635 nm) quantum efficiency of the EM-CCD camera.

4.23 shows the USPDC pattern with the same simulation parameters except for the crystal temperature. Consistent with the experimental result, the simulated USPDC noise emerges as a ring pattern; the diameter of the ring decreases with increasing temperature and that the radial positions of local minima change with temperature.

4.4.3 Signal-to-Noise Ratio Improvement for the Short-wavelength-pumped Upconversion Single-photon Detector

When a monochromatic IR signal is measured with the UCD, the bandwidth of the upconverted signal is usually narrower than that of the USPDC noise. Therefore, the use of a narrow bandpass (spectral) filter was the typical method for DCR reduction in previous works [21, 72]. Experiments and simulations show that both the intensity and the spectrum of USPDC noise vary spatially, which implies that the noise can also be removed by spatial filtering when the upconverted signal is located at a local minimum of the noise pattern. A demonstration of weak IR signal detection, at low photon count rates measurable with single-photon counters, is performed in order to confirm this novel DCR reduction scheme.

Experimental Setup

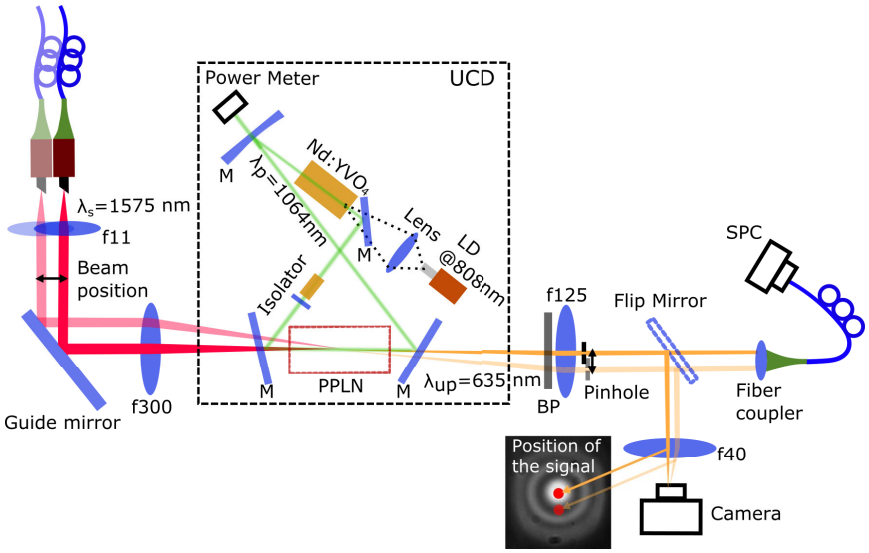

FIGURE 4.24: Experimental setup for single-photon detection based on a short-wavelength-pumped UCD. SPC, single-photon counter (Si based); LD, laser diode; BP, bandpass filter set.

Figure 4.24 shows a setup for single-photon detection with a short-wavelength-pumped UCD. The linearly polarized output of a fibre laser at 1575 nm is attenuated to the pW level before coupling into the UCD. The fibre tip and the collimating lens are mounted onto a translation stage, which enables angle tuning of the IR signal by translating the stage horizontally. The IR signal is mixed with the 1064 nm pump field inside a 25-mm long PPLN crystal with $\Lambda = 11.97\,\mu m$. The power of the upconversion signal is optimized by tuning the angle of incidence of the IR signal for different operating temperatures of the PPLN crystal. After collimation and spatial filtering, the UCD output is guided by a flip mirror, and either measured by a Si based single-photon counter (COUNT-250C-FC, intrinsic DCR = 70/s, Laser Components) directly or imaged by a camera. The red dots on the USPDC ring pattern in figure 4.24 illustrate two different positions of the upconverted signal for two different angles ϕ. Using the collinear case ($\phi = 0$), the efficiencies of different components used in the experiment are characterized as shown in table 4.4.

The diameter of the pinhole in figure 4.24 is 400 µm, which corresponds to the width of the innermost dark annular region of the USPDC noise pattern shown in the

Mirror transmission	Internal upconversion efficiency η_{up}	Pinhole efficiency
72 %	6 %	83 %
fibre coupling efficiency	QE of SPC @ 635 nm	Total efficiency η_{total}
81 %	73 %	2.1 %

TABLE 4.4: Efficiency characterization

inset of figure 4.24. Therefore, a strongly reduced DCR is expected when the pinhole is placed at the local minimum of the noise pattern. Meanwhile, in order to ensure that the upconverted signal passes through the pinhole efficiently, the IR signal from the single mode fibre (N.A. = 0.12; mode-field diameter = 10 µm) is coupled inside the PPLN with a 4f lens system (f300 and f11 with a focal length of 300 mm and 11 mm, respectively). The diameter of the upconverted signal at the position of the pinhole (placed after a collimating lens f125 with a focal length of 125 mm) is around 450 µm, which is comparable to the size of the pinhole. However, the $1/e^2$ beam diameter of the IR signal inside the PPLN crystal is $\sim$ 270 µm, which is larger than the required value that leads to optimal spatial overlap between the interacting pump and IR signal. Therefore, the measured internal upconversion efficiency η_{up} (6 %) is lower than the theoretical one (16 %) considering a 60 W 1064 nm pump power with a pump size $2\omega_0 = 400$ µm. In principle, η_{up} can be further improved by increasing the pump power. Using a similar UCD design ($\Lambda = 12.07$ µm, $\lambda_s =$ 1646 nm), it has been demonstrated that a 160 W pump with optimal spatial overlap with the signal can achieve η_{up} as high as 45 % [90]. In this work, a moderate pump power is used to maintain a stable operation of the UCD over the range of operating temperature in which USPDC noise is investigated.

Results

For every PPLN crystal operating temperature, the IR signal angle ϕ is fine tuned in order to maximize the power of the upconverted signal. The red square in 4.25a shows the temperature of the PPLN crystal versus the experimentally obtained optimal ϕ along with the numerical result (black curve) given by the QPM condition. The upconverted SCR and the DCR are shown in figure 4.25b and figure 4.25c, respectively. The collinear upconversion is achieved at 68.5 °C. The markers A and B indicate the data for cases with and without pinhole, respectively. Comparing these two cases, the SCR and DCR are reduced by 0.6 dB and 8 dB, respectively. With increasing angle ϕ, the SCR decreases due to a reduction in the effective crystal length [82]. Comparing the collinear upconversion (marker A) at 68.5 °C with the non-collinear case at 66.4 °C (marker C), the DCR decreases from $\sim 1.4 \times 10^4$/s to $\sim 3.6 \times 10^3$/s with a signal reduction of 1.6 dB.

Comparing the collinear upconversion without pinhole (marker B) to the non-collinear case with the spatial filter at the local minimum (marker C), this method achieves a DCR reduction of 14 dB with only a 2.2 dB penalty on the SCR. Based on the formula for the noise-equivalent-power (NEP) calculation [91]:

$$NEP = \hbar\omega_s\sqrt{2DCR}/\eta. \tag{4.34}$$

The NEP values at marker B and C are around 2.2 fW/$\sqrt{\text{Hz}}$ and 0.7 fW/$\sqrt{\text{Hz}}$, respectively. Therefore, this proposed method achieved an overall NEP improvement factor of 3.

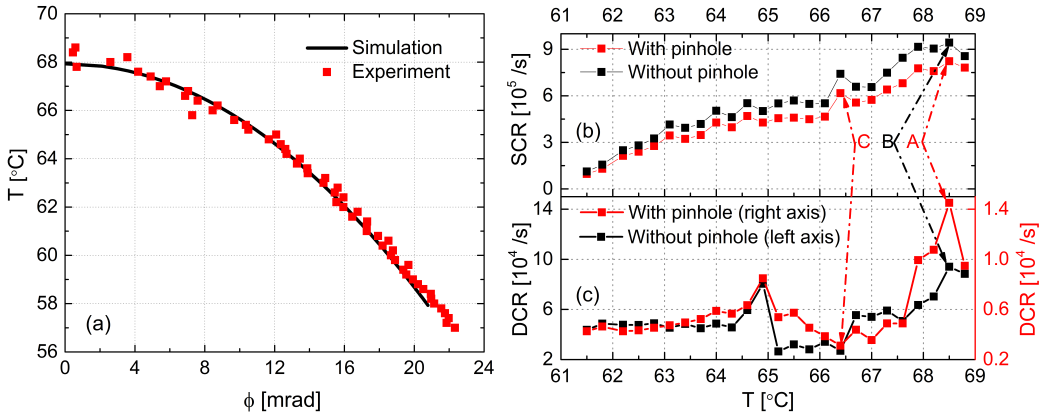

FIGURE 4.25: (a) PPLN crystal temperature versus the corresponding optimal IR signal angle ϕ. The red square is the experimental result and the black curve is the numerical simulation given by the QPM condition. Due to slight discrepancy introduced by the Sellmeier equations, a small offset of 1.2 °C is used in the simulated results in order to fit with the experimental one. (b) SCR and (c) DCR measured at different operating temperatures of the PPLN crystal.

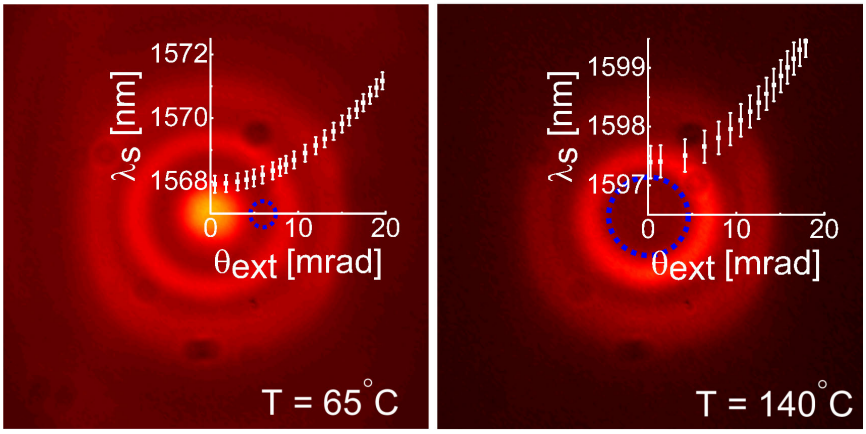

FIGURE 4.26: USPDC pattern for PPLN 1 operating at temperature of 65 °C and 140 °C. The overlay plots show λ_s as a function of θ_{ext}. The blue dash circles indicate the areas from which to collect the upconverted signal.

At marker B, the measured DCR is $\sim 1 \times 10^5$/s. Using the same parameters as the simulation result shown in figure 4.22, the USPDC count rate of 22 virtual PPLN crystals with the same RDC error of 6 % but different poling structures are calculated. The average USPDC count rate is 3×10^5/s (standard deviation of 1.3×10^5/s), which is in the same order of magnitude as the measured DCR.

Based on both experimental and theoretical investigation, the USPDC photons are mainly distributed in a solid cone corresponding to –15 mrad < θ_{ext} < 15 mrad and the spectrum of the noise pattern at different position varies along the radius. Therefore, the central wavelength of the spatially filtered noise is determined by the pinhole position on the USPDC noise pattern. Furthermore, the diameter of the pinhole and the acceptance bandwidth of the upconversion process determine the final spectral bandwidth of the noise. For example, figure 4.26a shows the USPDC pattern at a PPLN crystal temperature T = 65 °C. A pinhole with a diameter of 400 µm located at $\theta_{ext} = 6$ mrad (local minimum between the central peak and the innermost bright ring) would result in $\lambda_s = 1574.8$ nm and $\Delta\lambda_s = 0.5$ nm. Figure 4.26b is for

the case of T = 140 °C, in which the local minimum locates near the centre of the ring pattern. A larger pinhole can be applied in this case since the dark area around the local minimum is larger than in the previous one. Therefore, using collinear upconversion that maximizes interaction length (and, thus, conversion efficiency), a centred pinhole of 1.2 mm diameter would result in $\lambda_s = 1597.5$ nm and $\Delta\lambda_s = 0.6$ nm. A larger pinhole also means that the IR signal can be focused with a beam diameter of less than 270 µm inside the PPLN crystal to optimize its spatial overlap with the pump beam and consequently improve conversion efficiency. The bandwidth of the upconverted noise after the pinhole is $\Delta\lambda_{up} = \Delta\lambda_s\lambda_{up}^2/\lambda_s^2 = 0.1$ nm, which is comparable to the 0.06 nm bandwidth of the VBG used in a previous work on DCR reduction with a spectral filter [85].

For weak IR signal detection with short-wavelength-pumped UCD, the procedure for noise reduction with a pinhole is summarized as follows: first, optimize the collinear conversion efficiency by temperature tuning and obtain the corresponding USPDC noise pattern. Second, locate the local minimum of the noise pattern and choose a pinhole with the proper size that matches the width of the darkest annular region of the noise pattern. Third, with the assistance of a sensitive (EM-CCD) camera, fine tune the temperature of the PPLN crystal until the upconversion signal locates at a local minimum of the noise pattern. Fourth, block the noise with the pinhole and measure the upconverted signal with a Si based single-photon counter.

4.4.4 Summary and Discussion

For the first time, the non-uniform angular distribution of USPDC noise photons was measured in a short-wavelength-pumped UCD based on a bulk PPLN crystal. In order to explain its mechanism, a model considering non-collinear parametric interaction was established. Due to the presence of RDC error in the PPLN crystal poling structure, the SPDC intensity is enhanced, and it also has a unique spatial and spectral distribution $I_{SPDC}(\lambda_s, \phi)$. However, only the SPDC photons that fulfil the non-collinear QPM condition $\Delta k_{up}(\lambda_s, \phi) = 2\pi/\Lambda$ can be further upconverted efficiently. Therefore, the intensity of USPDC noise can be written as a function of the IR signal angle ϕ only. In order to further verify this model, simulations were run, and the results were consistent with the experimental results: (1) the USPDC photons given by simulation results also have angular distribution in both spatial and spectral region of interest. The USPDC count rate given by the simulation is comparable to the experimental one. (2) The rings in the spatial pattern of USPDC photons given by both experimental and numerical results contract towards the centre with the increase of temperature. (3) The PPLN crystal with the same designed parameters but different RDC error shows different ring patterns.

Based on the discovery of the USPDC ring pattern, a simple method for DCR reduction is proposed for single-photon detection using UCD. By choosing the proper non-collinear upconversion, the position of the upconverted signal can be moved to a local minimum of the USPDC ring pattern that enables a more efficient spatial filtering of the USPDC noise. Accordingly, a single-photon detection experiment based on the short-wavelength-pumped UCD was performed. This method achieved a 14 dB DCR reduction with only 2.2 dB penalty in SCR.

The central wavelength of the filtered USPDC noise photons is a function of the radial position of the pinhole on the ring pattern, and the 400 µm diameter pinhole used in the experiment is equivalent to an ultra-narrow (spectral) bandpass filter with an FWHM of $\sim$ 0.1 nm at the output of the UCD. Therefore, this method is a promising alternative to the use of expensive bandpass filters (e.g. volume Bragg

grating). Moreover, the pinhole used in the experiment can be replaced by an annular aperture for free-space IR signal detection considering a ring-shaped upconverted signal. In the previous work where UCD was used for an atmospheric lidar application [33], no spatial filter was applied for USPDC noise reduction. If an annular aperture is applied in that experiment, the signal-to-noise ratio of the detector is expected to improve following the same principle of using a pinhole to suppress USPDC noise without significant signal losses as demonstrated in this paper. The use of a spatial filter is also a potential low-cost alternative to the use of ultranarrow bandpass filters to reduce the DCR in 2 µm upconversion detector (with 1064 nm pump) [44] and in long-wavelength-pumped UCDs based on bulk periodically poled nonlinear crystals (i.e. suppression of upconverted spontaneous Raman scattering noise).

The side-effect of using non-collinear upconversion for DCR reduction is the decrease in total detection efficiency. However, the experiment also showed that a local minimum could also appear in the centre of the ring pattern where collinear upconversion occurs. This implies that for a certain IR wavelength signal, maximum detection efficiency and significant DCR reduction by simple spatial filtering can be achieved simultaneously.

4.5 Choice of Detectors for IR Detection

The properties of UCD including the upconversion efficiency, frequency response, noise sources and the corresponding noise reduction have been discussed. Apparently, UCDs with different design schemes possess different properties, which decide their overall performance. From the perspective of applications, choosing a UCD with the correct scheme for one specific application is important. Therefore, a strategy for the selection of IR detector is developed based on the knowledge gathered about the UCD so far.

To reduce the scope of this discussion to a digestible size, only InGaAs and MCT detectors together with four types of UCD (long-wavelength-pumped single-pass waveguide-based UCD; long-wavelength-pumped linear-cavity-enhanced UCD; short-wavelength-pumped ring-cavity-enhanced UCD; short-wavelength-pumped linear-cavity-enhanced UCD) are involved in the discussion. Moreover, all UCDs here are assumed to be based on PPLN, i.e. the spectrum of detection is limited between 1 µm and 5.5 µm, wherein the $LiNbO_3$ is transparent. It is necessary to emphasize that other detectors including new-concept IR detectors (e.g. e-APD MCT) and UCD based on other $\chi^{(2)}$ material should also be considered during the detector selection, the strategy demonstrated here just provides a reference to the UCD by comparing it with InGaAs and MCT based detectors.

In the flowchart (figure 4.27) of the proposed guide for IR detector selection, four conditions (in terms of *detection wavelength* λ_{IR}, *sensitivity to noise*, *large étendue* and *high bandwidth*) are used in the selection process.

- **Detection wavelength λ_{IR}?**
  PPLN-based UCD can work in the spectral region of (1 µm $\sim$ 5.5 µm), other $\chi^{(2)}$ material should be considered if the wavelength of IR signal is larger than 5.5 µm (i.e. "Other" in figure 4.27). IR signal in the region of (1 µm $\sim$ 2 µm) can be detected by an InGaAs based detector, and an MCT detector can work in the region of beyond 2 µm. In general, the acceptance bandwidth of UCD is much smaller than the spectral response range of the direct detector. Therefore,

strategies for the acceptance bandwidth broadening (e.g. temperature gradient on PPLN [92], chirped poling period [93], noncollinear QPM [40]) should be considered when the UCD is used for the polychromatic IR detection.

- **Noise-sensitive?**
  In order to decide whether the application is noise-sensitive or not, it is necessary to compare the signal photon budget with the noise of the competing direct detector (InGaAs or MCT). Therefore, this condition can be replaced by "large signal photon budget?". UCD working in the different spectral region has different background noise level, and its dominant noise sources vary with the working conditions. For example, the long-wavelength-pumped, waveguide-based UCD working at 1.5 µm has been shown to reach a DCR level of $\sim 1 \times 10^2$/s, which is mainly from the upconverted SRS [25]. In contrast, the short-wavelength-pumped, cavity-enhanced UCD working at 4 µm mainly suffers from the upconverted thermal noise, and its typical DCR is $\sim 1 \times 10^5$/s (figure 4.16).
  In order to take the full potential of upconversion, noise introduced by the detector (e.g. Si based detector, PMT) for the upconverted signal should be smaller than the noise induced by the upconversion module.

- **Large étendue?**
  In order to enlarge the étendue of a UCD, bulk PPLN and large pump area are used instead of the waveguide-PPLN. However, not all application needs a detector with a large étendue. For example, systems based on fibre/waveguide components has limited étendue, which make the waveguide-based UCD preferable for the IR detection.

- **High bandwidth?**
  In comparison with conventional direct IR detectors, a UCD has relatively large detection bandwidth. Moreover, the UCD with ring-cavity enhancement (or simply pumped by a single frequency laser) has a flat frequency response. In contrast, the UCD with linear-cavity enhancement usually has a non-uniform frequency response due to the beat noise originating from the multilongitudinal mode pumping, especially when the modulated frequencies of IR signal is very close to the pump beat frequency and/or its harmonics. If the application needs high bandwidth ($B > FSR$ of the linear cavity), a ring cavity is necessary. Otherwise, both schemes can be used for the detection.

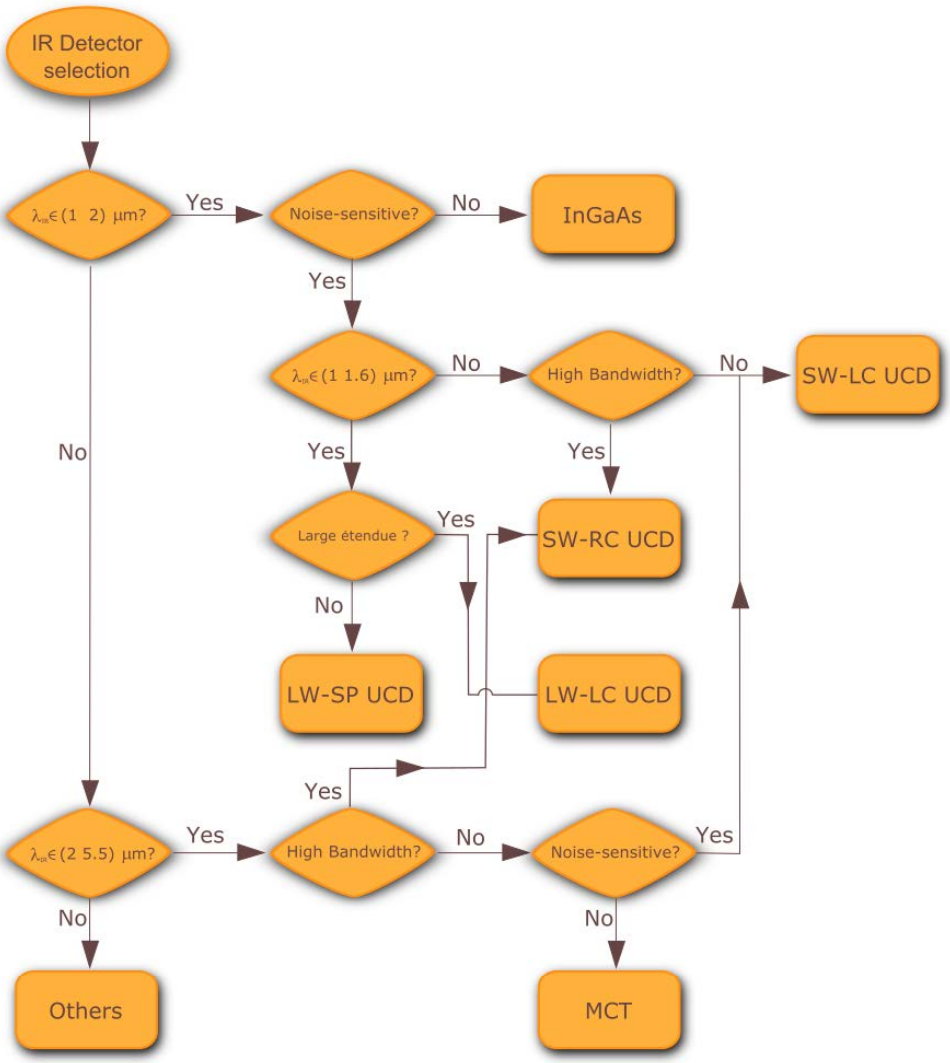

FIGURE 4.27: Flowchart for the IR detector selection procedure. LW-SP UCD, long-wavelength-pumped single-pass waveguide-based UCD; LW-LC UCD, long-wavelength-pumped linear-cavity-enhanced UCD; SW-RC UCD, short-wavelength-pumped ring-cavity-enhanced UCD; SW-LC UCD, short-wavelength-pumped linear-cavity-enhanced UCD.

After the specification of those conditions according to the requirement of the application, an optimal choice of IR detector can be obtained by following the flowchart shown in figure 4.27.

Chapter 5

Atmospheric CH_4 Sensing Using Upconversion Detector

In this chapter, the experiment of measuring the atmospheric CH_4 using a UCD will be introduced. This work is an outcome of the collaboration between our group (Optical Sensor, DTU Fotonik) and the Atmospheric Physics Department at DLR, Oberpfaffenhofen, Germany. The focus of this study is to evaluate the performance of the UCD for atmospheric lidar application. The principles of upconversion and noise generation in the UCD has been discussed in the previous chapters of this thesis. Thus, they will not be repeated here. But it is worth pointing out that a PMT is used to detect the upconverted signal, and the signal-to-noise ratio of the detection system including the performance of the PMT is analyzed in this study. Moreover, the noise equivalent power of the detection system is measured to be $\sim 127\,\mathrm{fW}/\sqrt{\mathrm{Hz}}$, which outperforms a conventional InGaAs based APD by a factor of 2 to 4 when both detection systems are used for DIAL measurements. Based on the UCD, CH_4 DIAL measurements have been performed yielding differential absorption optical depths with relative error of less than 11 % at ranges between 3 and 9 km.

It is necessary to point out that most of the material discussed in this chapter (Chapter 5) can also be found in [90], but more details about the the effect of PMT's gain and the noncollinear upconversion on the performance of the system will be presented here.

5.1 Introduction

Global warming and climate change are growing threats to our world and pose serious environmental challenges to society [94]. In order to mitigate the effects of climate change, it is important to understand the greenhouse gas (GHG) cycles on a global scale [95]. CH_4, in particular, is the second most relevant anthropogenic GHG after CO_2 and a recent study shows that it plays an increasing role in global warming [96]. Thus, there is a significant interest in developing highly accurate remote sensing systems for CO_2 and CH_4 monitoring.

Two potential and closely related technologies for accurate GHG measurement by means of active remote sensing are the differential absorption lidar (DIAL) and the integrated path differential absorption (IPDA) [97, 98]. DIAL can measure the profiles of target gas mixing ratio in a certain range by analyzing the atmospheric backscatter signals on two different wavelengths. In contrast, IPDA does not use backscatter signals from molecules or aerosol but from a hard target. Therefore, IPDA only measures the average mixing ratio of the gas in the columnar volume between the transceiver and the hard target. The working principles of these two

technologies are nevertheless similar. However, the intensity of the backscatter signal from the hard target is usually much stronger than the one from the atmosphere; therefore, the required detectivity of the detector for the DIAL system should be higher than that for the IPDA system when both systems operate under similar conditions. Unfortunately, the required wavelengths for lidar measurement of the GHGs (CO_2 and CH_4) are within the infrared range, wherein the detectivity of commercially available InGaAs and HgCdTe based infrared detectors are orders magnitude lower than those working in the visible band, i.e. Si based detectors or photomultiplier tubes (PMT) [99]. State-of-the-art airborne and spaceborne lidar applications using direct infrared detectors are currently restricted to deploying IPDA technology [98, 100–104]. The availability of infrared detectors with higher sensitivity will also enable range-resolved DIAL measurements to be performed.

Instead of using direct infrared detectors, a promising approach is to use an upconversion detector (UCD) – a combination of an optical upconverter that efficiently translates infrared signals to the visible region and a visible detector that has high detectivity. Previously, an intracavity UCD for a CO_2 IPDA/DIAL system was demonstrated, wherein its performance was compared against an InGaAs detector directly[45]. In that UCD, a 20-mm long PPLN bulk crystal was applied to upconvert a 1572 nm signal to 635 nm by mixing with a 1064 nm intracavity pump. Even though the previous UCD did not yet have better performance than the reference InGaAs detector, it showed a high potential for further improvement.

In this chapter, an improved upconversion detector which outperforms an InGaAs based APD for long-range DIAL measurements is demonstrated. A number of improvements over the previous UCD for CO_2 IPDA/DIAL are discussed. This time, the target gas of interest is CH_4 rather than CO_2. Note that this is the first report of a CH_4 lidar enabled by the UCD technology. The on- and off-line signals for CH_4 probing at 1645.56 nm and 1645.84 nm, respectively, are mixed with a 1064 nm pump in a 25-mm long PPLN bulk crystal. The upconverted signal at 646 nm is detected by a standard PMT. The simple and compact receiver optics used with the improved UCD only consists of a 3-inch diameter plano-convex lens with a focal length of 750 mm. The backscatter signals from the atmosphere in ranges of a few kilometres are detected by both UCD and the conventional InGaAs APD. It is experimentally confirmed that the UCD achieves better performance thus constituting a novel alternative for atmospheric lidar signal detection.

5.2 Theory

5.2.1 Detector Étendue

Similar to a conventional detector, the ability of UCD for infrared signal collection is determined by its étendue ($A\Omega$). A is the detector area and Ω is the solid angle from which the detector can receive the signal. The UCD has a relatively small acceptance angle which is fundamentally limited by the upconversion process [45]. In the following experiment, a 25-mm long PPLN is applied, which corresponds to an external acceptance half-angle of 14.7 mrad. The beam waist of the pump inside the PPLN crystal is around 200 µm. Therefore, the étendue of the UCD is $A\Omega = 85\,\mu m^2 rad^2$. On the contrary, the étendue of a typical InGaAs APD for atmospheric lidar application [98] is $A\Omega = 2.36 \times 10^4\,\mu m^2 rad^2$ (diameter D = 0.2 mm; field-of-view (FOV) = 56°), which is around 280 times larger than that of the UCD.

5.2.2 Signal-to-Noise Ratio

In the following lidar measurement, an InGaAs APD is used as a reference detector to benchmark the performance of the UCD. Meanwhile, the upconverted signal in the UCD is detected by a PMT. For both, APD and PMT, the same formula may be used for SNR calculation [105]:

$$\frac{S}{N} = \frac{i_{signal}}{\sqrt{2eFB(i_{signal} + i_b + i_d) + i_N^2/M^2}}, \tag{5.1}$$

where e is the electron charge, B the detection bandwidth, i_{signal} the photocurrent generated by the incident signal photons, i_b the photocurrent due to background noise, i_d the dark current, i_N the amplifier circuit thermal noise, F the noise figure, and M the gain. It has to be emphasized that in comparison to InGaAs APD, the PMT has lower noise figure ($F_{APD} \approx 3$; $F_{PMT} \approx 1$) and much higher gain ($10 < M_{APD} < 20$; $10^5 < M_{PMT} < 10^6$). Therefore, the PMT has better performance in terms of suppressing the noise generally.

The SNR for the APD can be calculated using equation 5.1 directly. But for the case of the UCD, its quantum efficiency and USPDC noise should be considered along with the properties of the PMT when equation 5.1 is used. The photocurrent of the UCD is:

$$i_{signal} = \frac{P_{IR}\eta_{up}\eta_{PMT}\eta_{opt}e}{\hbar\omega_{IR}}, \tag{5.2}$$

where ω_{IR} is the angular frequency of the IR signal, η_{up} and η_{PMT} are the quantum efficiencies for the upconversion and the PMT respectively, while η_{opt} is the coupling efficiency of the optical system. The current due to the background noise is:

$$i_b = \frac{(P_b\eta_{up}\eta_{opt} + AI_{USPDC})\eta_{PMT}e}{\hbar\omega_{IR}}, \tag{5.3}$$

where P_b is the power of the ambient noise, I_{USPDC} is the intensity of the USPDC noise, and A is the cross-sectional area of the pump beam in the PPLN crystal.

In the following experiment, the total quantum efficiency ($\eta_{up}\eta_{PMT}\eta_{opt}$) of the UCD is around 8 %, which is smaller than that of the APD ($\sim$ 60 %). But the UCD has a higher detectivity than the APD and it can only succeed in outperforming the APD when relatively weak signals are measured.

5.3 Characteristics of the UCD

5.3.1 Setup of the UCD

Figure 5.1 shows the schematic diagram of the UCD (its real photograph is shown in figure 3.2). Its design is similar to the upconversion module discussed in Chapter 3, but some components and parameters are changed in order to suit the CH_4 IPDA/DIAL application. The poling period of the PPLN crystal is 12.45 µm and the temperature of the crystal is precisely maintained at 129.9 °C. The upconversion photon is detected by a PMT (H7422-40, Hamamatsu Photonics) and the PMT output current is amplified by a current amplifier (DHPCA-100, FEMTO GmbH). The output voltage of the current amplifier is treated as the final output of the UCD prior to data sampling (sampled by an A/D converter or monitored by an oscilloscope).

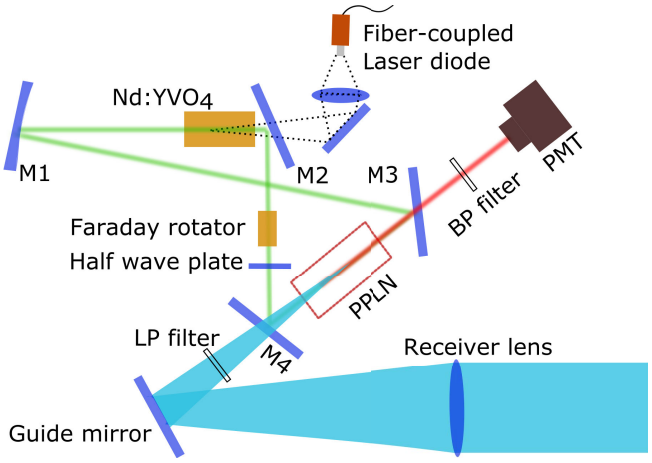

FIGURE 5.1: The schematic diagram of the UCD where the guide mirror and the receiver lens are included. The PPLN crystal has a length of 25 mm and a poling period of 12.45 µm, the LP filter has a cut-on wavelength of 1250 nm, the BP filter has a central wavelength of 647.1 nm and a bandwidth of 2.5 nm. The cyan, green and red beams represent the 1646 nm signal, 1064 nm pump and 646 nm upconverted signal, respectively. More details of the UCD can be found in Chapter 3 (page 25).

Based on the experience gained from the preliminary development of the CO_2 lidar UCD [45], the following performance improvements are applied in the new UCD. First, a ring laser cavity with the capability of unidirectional lasing at 1064 nm (upconversion pump wavelength) is implemented. In comparison to a linear laser cavity used in the CO_2 lidar UCD, the ring design enables single longitudinal mode pump lasing. At high pump power levels, single mode operation of the ring laser improves upconversion efficiency [73]. Furthermore, unwanted noise due to multi-mode pumping [70] is avoided. Second, the overall QE of the new UCD is improved by employing a longer PPLN crystal (25 mm versus 20 mm), a larger intracavity

Parameter	UCD in Ref. [45]	New UCD
Signal wavelength (nm)	1572	1646
Upconverted wavelength (nm)	635	646
1064 nm pump cavity type	Linear	Ring
PPLN length (mm)	20	25
PPLN period Λ (µm)	11.8	12.45
Intracavity pump power (W)	50	150
Pump beam waist ω_0 (µm)	100	200
Étendue (µm^{2}rad^2)	25	85
LP filter cut-on wavelength (nm)	n.a.	1250
FWHM of BP filter, $\Delta\lambda_{FWHM}$ (nm)	10	2.5
Visible PMT Detector	Hamamatsu (R928)	Hamamatsu (H7422-40)
QE of the PMT	8 % @635 nm	20 % @646

TABLE 5.1: Parameters of the previous and the new UCD.

pump power (150 W versus 50 W), and a larger pump beam waist ω_0 (200 µm versus 100 µm). Third, the étendue of the new UCD is 3.2 times that of the previous one as a result of the combination of larger detection area and slightly reduced acceptance angle (due to longer crystal length). Fourth, more suitable filters are employed in the CH_4 lidar UCD: a long-pass (LP) filter with cut-on wavelength at 1250 nm is

placed right before the M4 to filter out the atmospheric stray-light noise in the visible band; a bandpass (BP) filter (Semrock, LL01-647-12.5) with a central wavelength of $\lambda_c = 647.1$ nm and a bandwidth of $\Delta\lambda_{FWHM} = 2.5$ nm suppresses the pump-induced noise more efficiently. Lastly, a visible PMT with an improved QE (20 % versus 8 %) is used to detect the upconverted photons at 646 nm. A list of all improvements of the new UCD versus the previously used configuration is given in table 5.1.

5.3.2 Quantum Efficiency of the UCD

In order to optimize the performance of the UCD, the upconversion quantum efficiency is measured as a function of PPLN crystal temperature T. A beam from a CW fibre-coupled DFB laser with a wavelength of 1645.85 nm is focused into the PPLN crystal (transmitted through mirror M4 in figure 5.1) with precise position and angle tuning for collinear upconversion. Only the unconverted power of the 1646 nm beam through the upconversion module is measured by filtering out all other wavelengths with an LP filter (1250 nm cut-on wavelength) placed in front of a power meter, which temporarily replaces the PMT in figure 5.1. The upconversion QE, $\eta_{up}(T)$, is characterized as:

$$\eta_{up}(T) = 1 - P_r(T)/P_R, \tag{5.4}$$

where $P_r(T)$ is the unconverted 1646 nm power at temperature T. P_R is the transmitted 1646 nm power when no 1064 nm pump is applied. Figure 5.2 shows the relation

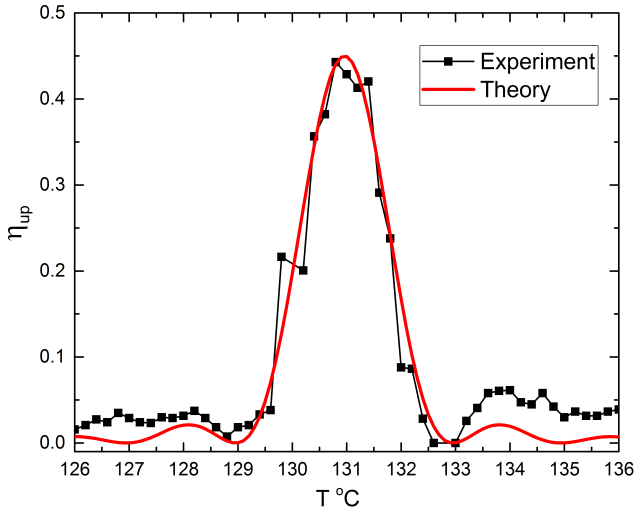

FIGURE 5.2: Measured (black square) and theoretical (red line) internal quantum efficiency of the upconversion module as a function of the temperature of the PPLN crystal. The theoretical model (red) is horizontally shifted by 2.5 °C, so its central lobe coincides with that of the measured curve. The temperature offset is contributed to the slight inaccuracy in the refractive indices calculated using the Sellmeier equation.

between the internal upconversion efficiency (i.e. without the effect of transmission losses due to cavity mirrors) and the temperature of the PPLN crystal. At a signal wavelength of 1645.85 nm, the UCD achieves maximum internal QE of 45 % at a PPLN crystal temperature around 131 °C. During long-term operation, the temperature was stabilized to better than 0.02 °C, thus, variations in the QE of the UCD due to temperature changes can be neglected.

The intracavity pump power is monitored by measuring the proportional 1064 nm leakage power through M1 (see figure 5.1). Over a 30-minute period, the measured 1064 nm leakage power is 16.4 $\pm$ 0.2 mW (sampled every 3 minutes). Therefore, the standard deviation in the UCD quantum efficiency caused by pump power variation is only around 1.2 % during half an hour period. In a calibration measurement, it was proved that 16.4 mW leakage power corresponds to $\sim$ 150 W intracavity pump power.

5.3.3 Noise Properties of the UCD

The UCD can be treated as a combination of an upconversion module and a PMT. The SNR of the UCD can be calculated with equation 5.1 by considering the following two prevailing optical noise sources, which potentially contribute to i_b.

The atmospheric background noise at 1646 nm. A long-pass filter with a cut-on wavelength at 1250 nm is applied in front of the entrance of the UCD to block the solar background noise that the PMT is sensitive to. The PPLN crystal has a small acceptance bandwidth ($\sim$ 0.6 nm) and a small acceptance angle (< 20 mrad) for the input 1646 nm signal. Thus, the upconversion process acts as both a spectral and a spatial filter that suppresses the atmospheric noise further. In general, the atmospheric background noise at 1646 nm is negligible in comparison to other noise sources in the UCD.

Noise generated in the upconversion process. Upconverted thermal radiation [33], upconverted Raman scattering noise [25] and the USPDC noise are the inherent noise sources in the upconversion module. The bandpass filter in front of the PMT can filter the broadband noise (upconverted thermal and upconverted Raman scattering noise) efficiently. However, it is not possible to remove the USPDC noise completely due to its spectral overlap with the upconverted signal. Based on the calculation, the noise source due to SHG-SPDC process does not exist in this case.

In order to quantify the noise generated by the current amplifier, the PMT, and the upconversion module separately, the output of the current amplifier is monitored by an oscilloscope under three conditions: (i) only the output voltage of the current amplifier (N_{AMP}), (ii) the combination of the current amplifier and the PMT ($N_{AMP+PMT}$), and (iii) the overall output of the UCD (at 150 W circulating pump power) without infrared signal input ($N_{AMP+PMT+UP}$). The output signal is sampled over 2 ms at a rate of 25 MHz. The measured root mean squares (RMS) of the sampled output voltage values are listed in table 5.2. The comparison of the RMS values shows that the dominant noise originates from the upconversion module.

Noise source	N_{AMP}	$N_{AMP} + N_{PMT}$	$N_{AMP} + N_{PMT} + N_{UP}$
RMS (mV)	2.3	73	179

TABLE 5.2: Noise in different parts of the upconversion detector system.

Considering the internal upconversion efficiency η_{up} (45%), the estimated optical coupling efficiency η_{opt} (85%), the PMT sensitivity S (106 mA/W) at 646 nm, the PMT gain M (1.11×10^5), the transimpedance R_f (1×10^5 V A^{-1}) of the current amplifier and its detection bandwidth B (10 MHz), the noise equivalent power (NEP) of the

UCD is estimated to be around 124 fW / $\sqrt{\text{Hz}}$ using equation 5.5.

$$NEP = \frac{N}{\eta_{up}\eta_{opt}SR_f M\sqrt{B}}. \tag{5.5}$$

5.4 Experiment

5.4.1 IPDA Measurement

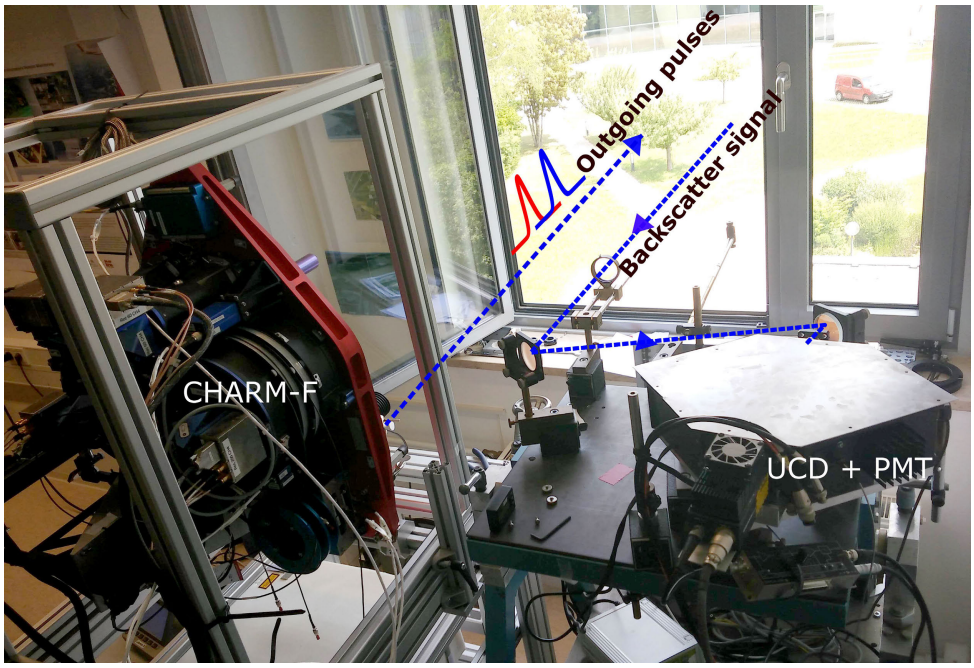

(a)

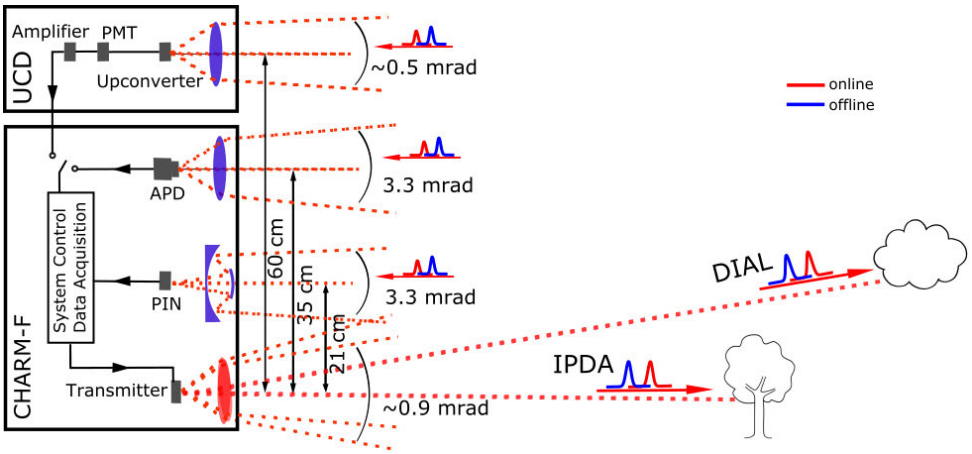

(b)

FIGURE 5.3: (a) Photograph and (b) conceptual sketch of the setup used for the lidar measurements. For comparison with CHARM-F detectors, the UCD can be connected to the data acquisition card otherwise used to digitize the APD signal. For the IPDA measurement, the beam was directed to a distant forest. For the DIAL measurements, the entire system was tilted such that the beam propagated beyond the tree tops. For mechanical reasons, the lateral distance between the outgoing beam and the detector is larger for the UCD in comparison to the CHARM-F receivers. The divergence angle of the transmitter and the receivers' FOVs are also given (not drawn to scale).

In order to evaluate the improvement of this new UCD over the previous one, it is tested under similar conditions as the experiment described in [45] using the CHARM-F system [98] designed as an airborne lidar demonstrator for the French-German MERLIN mission [104]. CHARM-F was devised to measure both CO_2 and CH_4. While in the preceding study [45] the CO_2 channel was used, here only the CH_4 channel was employed. The return signal from a hard target (i.e. the forest located 2.3 km away from the laboratory building) is simultaneously measured by the InGaAs PIN detector of CHARM-F and the UCD. CHARM-F operates in a double pulse mode with a repetition rate of 50 Hz. The wavelengths of the two pulses are 1645.56 nm and 1645.84 nm, which correspond to the on- and off-line of the chosen resonance frequency of the CH_4 molecule. The pulse duration is 20 ns and the pulse energy is around 10 mJ. CHARM-F has two receiver systems. One consists of a 200-mm diameter Cassegrain telescope and a 1-mm InGaAs PIN detector; the other, a 60-mm diameter lens with a 0.2-mm InGaAs APD detector. More specific information about CHARM-F can be found in [98]. As a deviation from the parameters described in [98] the divergence of the transmit beam was reduced from ∼3 mrad (chosen to optimize IPDA measurements from aircraft) to ∼ 0.9 mrad which is much better adapted to the FOV of the UCD. In the previous work on CO_2 lidar measurement with a UCD, an 8-f scaling system with a demagnification of 250 was applied to collimate the backscatter signal into the PPLN crystal. In contrast, the present infrared signal is focused into the PPLN crystal by a single 3-inch diameter plano-convex lens. Figure 5.3a and figure 5.3b show the photograph and sketch of the experiment setup, respectively.

Gain of PMT

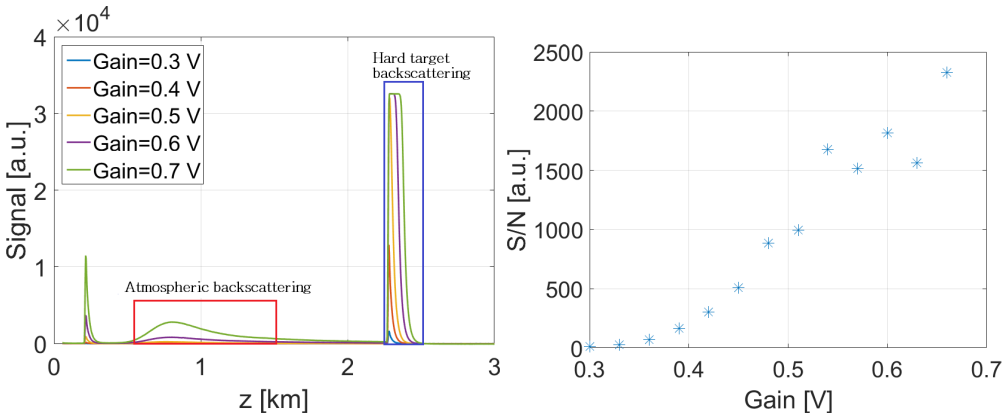

FIGURE 5.4: (a) Backscatter signal from the on-line pulses measured by the UCD at different PMT gain settings. The signal due to the atmospheric scattering and the hard target scattering are marked with the red and blue box, respectively. (b) SNR ratio of the UCD measurement as a function of PMT gain.

In this experiment, the upconverted signal is measured by a PMT (see table 5.1), which affects the SNR of the measurement significantly. Before using the UCD for lidar measurement, the effect of the PMT on the performance of the UCD is investigated by measuring the backscatter signal at different PMT gain settings. It has to be emphasized that the temperature of the PPLN is kept at 129.6 °C during the measurement. Figure 5.4a shows the intensity of the on-line signal with different PMT gain settings. The signal from the hard target (located at 2.3 km) and from the

atmospheric scattering (at the region of $z > 0.5\,\text{km}$) are marked with the blue and the red box in figure 5.4a, respectively. Apparently, the PMT is saturated by the hard target signal when the gain voltage is larger than 0.5 V. Therefore, the signal in the red box is used to characterize the effect of the PMT gain setting on the performance of the system: the maximum signal level in the red box P_{peak} and the standard deviation of signal $N_{background}$ at the region of $z > 17\,\text{km}$ are calculated, respectively. Afterwards, the SNR calculated as $P_{peak}/N_{background}$ is shown in figure 5.4b, which indicates that the SNR gets improved when a larger gain is applied. This is also the main argument of using a PMT, the noise from the PMT, amplifier and the AD converter can be inhibited by using a high PMT gain. Additionally, the measurement here indicates that the UCD is capable of measuring weak signals with a high PMT gain.

Noncollinear Upconversion

The sensitivity of the conventional semiconductor-based detectors can be assumed constant for the on- and off-line signal since the wavelength difference between those two signals is small ($|\lambda_{on} - \lambda_{off}| < 1\,\text{nm}$). In contrast, the upconversion efficiency for the on- and off-line signal has certain difference due to the limited acceptance bandwidth and the different QPM angle (ϕ in figure 2.3c). Thus, the detection efficiency for the on- and off-line signal should be calibrated before using the UCD for the IPDA measurement.

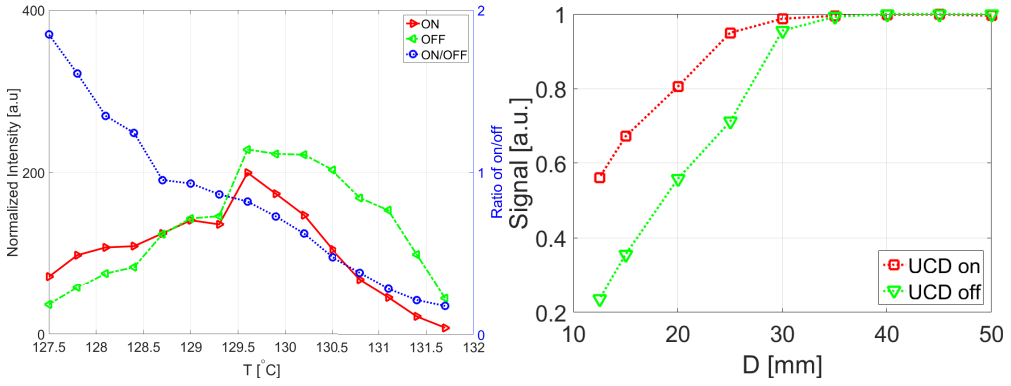

(a) (b)

FIGURE 5.5: P_{peak} for the on- and off-line pulses as a function of (a) the temperature of the PPLN crystal and (b) the diameter of the iris.

For the different PPLN crystal temperature, the normalized P_{peak} in the red box is calculated for both on- and off-line signal, which is shown in figure 5.5a. In addition, the ratio between the on- and off- line signal $P^{on}_{peak}/P^{off}_{peak}$ is also calculated. The PMT gain setting is 0.66 V during the measurement. Based on figure 5.5a, following conclusions can be drew: 1) The optimal temperature for the off-line signal ($T_{opt,off} \approx 129.8\,°\text{C}$) is different from that of the on-line signal ($T_{opt,on} \approx 129.5\,°\text{C}$). 2) The detection efficiency for the on-line signal is higher when $T < 129\,°\text{C}$, while the efficiency for the off-line signal is higher when $T > 129.5\,°\text{C}$. This can be explained using the theory of noncollinear upconversion: when the temperature is lower than 129 °C, two signals fulfil the noncollinear QPM condition, according to equations 2.13b and 4.17, the on-line signal with a larger effective length ($\phi_{off} > \phi_{on}$) is expected to have a higher upconversion efficiency.

In order to further investigate the effect of noncollinear upconversion on the on- and off-line signals, an iris is placed in front of the 3-in plano-convex lens, and the backscattering signal with different iris diameters is measured. During the measurement, the PPLN temperature is kept at 129.6 °C, and the gain voltage of the PMT is 0.66 V. Figure 5.5b shows the normalized P_{max} for the on- and off-line signals as a function of the diameter of iris. The iris has no effect on the measurement when the diameter is larger than 30 mm, and the off-line signal suffers from more signal losses when the diameter is smaller than 30 mm. This is due to $\phi_{off} > \phi_{on}$, thus, the iris starts blocking the off-line signal first when the diameter of the iris decreases.

Comparison with the PIN Detector

Figure 5.6 shows the normalized backscatter signal measured by the UCD and the PIN detector. The relative absorption as measured by the PIN is of the order of 0.7 which is what is expected from an average CH_4 mixing ratio of $\sim$ 1.9 ppmv (using HITRAN 2012). For energy referencing, the internal calibration chain of CHARM-F was used where the ratio of the outgoing on- and off-line pulses are measured by the same PIN. This was, however, not possible with the UCD. Therefore, the energies were referenced to the energy ratio measured by the PIN. Due to the slightly lower conversion efficiency of the UCD at the on-line wavelength at the selected crystal temperature which was confirmed by lab measurements the ratio of the on- to off-line return signals is somewhat lower.

The signals at $\sim$ 18 km range depicted in the inset of figure 5.6 show the background noise. The root mean square (RMS) of the background noise given by the UCD is only 1.3 times that of the PIN detector. On the contrary, the RMS given by the previous UCD was $\sim$ 3.5 times larger than that of the PIN detector [45]. Moreover, benefiting from the improvement of the new UCD, the peak power of the upconversion signal from a hard target can easily saturate the PMT when the recommended gain (1×10^5 to 1×10^6) is applied. The gain setting for the UCD data in figure 5.6 is only around 1×10^3, which implies that the UCD is expected to perform even better if a signal with lower intensity (e.g. atmospheric backscatter signal) is measured and a higher PMT gain setting is used. The result given by the UCD during the IPDA measurement indicates that the UCD can even detect much weaker signals using an appropriate PMT gain. In order to fully explore the potential of the UCD, the atmospheric backscatter signal (few orders of magnitude lower than the IPDA hard target signal) was measured, enabling real DIAL measurements.

5.4.2 DIAL Measurement

First CH_4 DIAL measurements were performed in Oberpfaffenhofen, Germany on June 23rd, 2017 around 11 a.m. UT. The weather was mostly sunny, with few clouds. The temperature was $\sim$ 27 °C and weak ($\sim$ 4 m/s) westerly winds prevailed. The lidar transceiver was slant-pointed at $\sim$ 6° out of the laboratory window (see figure 5.3) steering over the forest such that no hard target (e.g. trees) remained in the beam path. The InGaAs APD in the CHARM-F has better performance than the PIN detector when the atmospheric backscatter signal is measured. Therefore, it is the APD instead of the PIN detector that is used as a reference for comparison with the UCD measurement. Since APD and UCD-PMT require the use of the same data acquisition card they cannot operate simultaneously. Therefore, UCD and APD are sequentially applied for the DIAL measurements with each measurement lasting 15

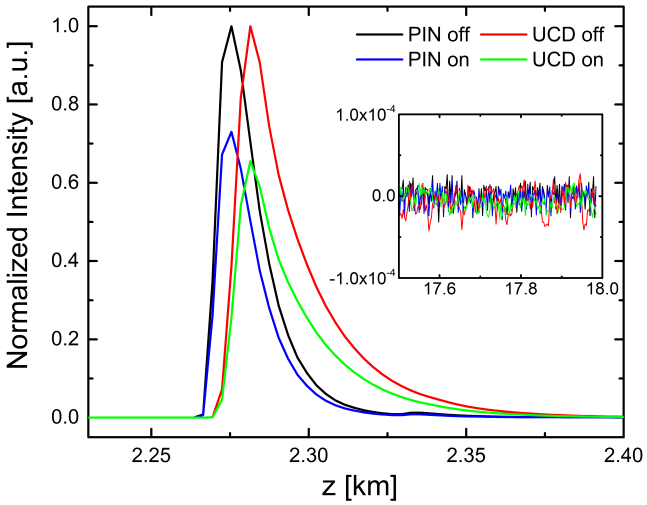

FIGURE 5.6: Backscatter signal from the forest located 2.3 km away measured by the UCD and the reference InGaAs PIN detector and the background signal (inset) from a range of 17.5 km and beyond. The plots are the averages over 6000 pulse pairs (i.e. averaging time of 2 minutes).

minutes. The separation between the two measurements was around 40 minutes. The data was digitized at a sampling rate of 100 MHz for both measurements.

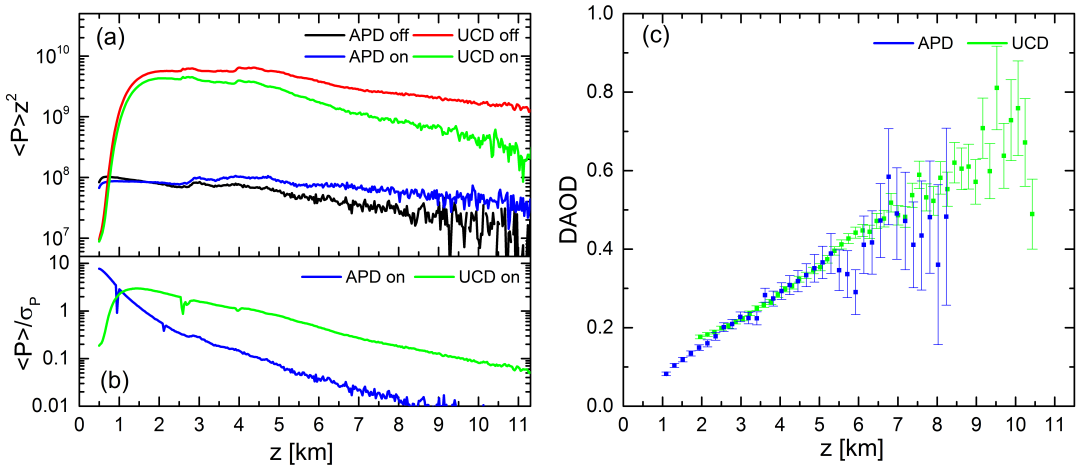

FIGURE 5.7: (a) Range dependence of the on- and off-line range-corrected signals given by the APD and the UCD, (b) signal-to-noise ratio of the on-line backscatter measurement, and (c) the DAOD given by the two detectors. All results are obtained by averaging 45000 pulse pairs (averaging over 15 minutes).

The divergence angle of the transmitter is $\sim$ 0.9 mrad. The nominal FOV of the APD based receiver is 3.3 mrad. The lateral distance between APD and transmitter beam is 35 cm while it is larger (60 cm) between UCD and transmitter beam due to mechanical constraints (see figure 5.3). Therefore the full overlap between transmitter and UCD is shifted towards longer distances. The FOV of the UCD based receiver can be estimated as 0.5 mrad given the ratio between the 1064 nm pump diameter (400 µm) and the focus of the receiver lens (750 mm).

In analogy to the data presented in [106], figure 5.7a shows range-corrected backscatter signal given by the APD and the UCD at position z upon averaging echoes from

45000 pulse pairs (corresponding to a 15-minute average). Due to the stronger on-line absorption by the CH_4 in the atmosphere, the ratio of the off- to the on-line signal becomes larger with increasing distance. In order to compare the performance of the APD and the UCD, ratios of the raw on-line signal average $\langle P \rangle$ to its standard deviation σ_P measured by both detectors are shown in figure 5.7b. Based on the NEP of the UCD and the bandwidth of the detection, the noise floor of the UCD can be calculated as 0.4 nW, which corresponds the intensity of the on-line signal at the range of 5.2 km. For the APD, the NEP can be calculated as 240 fW$/\sqrt{\text{Hz}}$ by considering the RMS of the APD signal at around 18 km (1.36 nA), the APD sensitivity at 1646 nm (1.8 A/W) and the detection bandwidth B (10 MHz). The noise floor is in the 0.8 nW level, and the SNR for the on-line signal is unity at a range of 1.5 km, already. For z >3 km, the $\langle P \rangle / \sigma_P$ of the UCD is more than 5 times better than that of the APD and it clearly shows that the UCD outperforms the APD for this DIAL measurement. In order to obtain the same statistical error when using the UCD, the averaging time thus can be reduced by more than an order of magnitude.

Based on the on- and off-line signal given by the UCD detectors, the differential absorption optical depth (DAOD) and its corresponding error bars are shown in figure 5.7c. Similar to the method used in [107, 108], the DAOD is calculated using equation 5.6:

$$DAOD(z) = \frac{1}{2} ln \left[\frac{P^{off}(z) P^{on}_{pulse}}{P^{on}(z) P^{off}_{pulse}} \right]. \tag{5.6}$$

where $P^{on,off}(z)$ is the backscatter signal measured by the detector and $P^{on,off}_{pulse}$ is the reference pulse energy. The DAOD of the UCD in figure 5.7c increases linearly at ranges between 3 km and 9 km with relative errors from 3 % to 11 %. The DAOD of the APD that was recorded $\sim$ 40 minutes later shows the same range dependence although, as expected, with much higher error bars.

The range-resolved CH_4 mixing ratio can be obtained based on the data in figure 5.7c using the temperature and pressure dependent absorption cross sections of the CH_4 molecule with respect to the on- and off-line wavelengths. The slopes in figure 5.7c suggest a rather constant CH_4 mixing ratio of $\sim$ 1.9 ppmv in the boundary layer. However, since the angle of inclination of the transceiver was not very accurately calibrated and no means for intercomparison of the methane mixing ratio was available during this preliminary experiment, deriving the range-resolved mixing ratio was not performed at this stage.

5.5 Discussion

The previous UCD showed great potential for IPDA CO_2 detection even though its relatively low QE and small étendue limited its performance [45]. In the new CH_4 lidar UCD, these two parameters are effectively improved by applying altogether a ring cavity, a higher pump power, a larger pump area, a longer PPLN crystal, and a visible PMT with improved QE (see Table 5.1). Due to these improvements, the new UCD outperforms the InGaAs APD detector when used for CH_4 lidar application.

In the previous CO_2 measurement, an 8-inch diameter Cassegrain telescope [45] was used for the infrared signal collection. Due to the relatively small étendue of the upconversion module, only a small part of all infrared photons collected by the telescope were upconverted. Furthermore, the secondary mirror of the Cassegrain telescope presumably blocked a part of the infrared signal. In the new UCD receiver system, only a single 3-inch diameter plano-convex lens with a focal length of 750

mm was used. The simple receiver lens system makes the signal collection more efficient and easier to adjust. As before, the CHARM-F system [98] was used as the testbed to compare the UCD receiver to the existing state-of-the-art.

Already at moderate gains of the PMT in the UCD, the backscatter signal from a hard target (2.3 km away) became saturated in the IPDA measurement which could be avoided by either attenuating the energy of the transmitted (or received) pulses or by selecting a hard target at a much farther range (>10 km). The data in figure 5.6 shows that the detection efficiency of the UCD for the off-line signal was ∼14 % higher than that for the on-line. In future IPDA measurements, therefore, the relative detection efficiency of the UCD should be calibrated before performing columnar average CH_4 mixing ratio calculation. No calibration, however, is required for the DIAL technique and the high sensitivity of the UCD versus direct detectors make such measurements possible resulting in range-resolved lidar measurements.

The DIAL measurement results shown in figure 5.7 demonstrate that the UCD outperforms the InGaAs APD. Although the more direct SNR comparison of the two detectors in figure 5.6 shows comparable performance, it is necessary to emphasize that the PMT gain setting used for the UCD in the IPDA measurement was relatively low (i.e. 1×10^3) to avoid saturation. In the DIAL experiment where the lidar system was pointed away from the hard target, it was possible to increase the PMT gain to 1×10^5, thereby increasing the SNR performance of the UCD and allowing for range-resolved CH_4 DIAL measurements.

This UCD can easily be extended to other gas-sensing lidar applications working in the MIR region (e.g. 2 µm to 5 µm) by simply changing the PPLN poling period, spectral filters, and a cavity mirror (M4 in figure 5.3b) to match the specific MIR signal wavelength. Due to high detectivity and room-temperature operating condition, the MIR UCD can serve as a better alternative to conventional MIR detectors (e.g. cryogenically cooled HgCdTe or InSb detector) in atmospheric lidar applications.

5.6 Summary

In this work, the first IPDA and DIAL measurements of CH_4 using an upconversion-based detector are demonstrated. Benefiting from the high signal-to-noise ratio performance of an improved upconversion detector, the system possesses the ability to measure the DAOD between 3 and 9 km with relative errors smaller than 11 %. The CH_4 lidar UCD outperforms a conventional InGaAs APD detector and shows strong potential as an alternative detector for future DIAL applications in wavelength ranges where direct detectors have limited performance and where high quantum efficiency and low noise are required.

Chapter 6

Conclusion and Outlook

6.1 Conclusion

My Ph.D. project is the continuation of Lasse Høgstedt's work [45]: to design and build our 2nd generation UCD for atmospheric sensing. Apparently, the 2nd generation UCD has some similarities with the 1st generation UCD built and tested by Lasse. For example, both UCDs used a bulk PPLN crystal as the $\chi^{(2)}$ material; both are intracavity-pumped with a 1064 nm laser; both were optimized for IR detection around 1.6 µm (1572 nm and 1646 nm for the 1st and 2nd generation UCD, respectively) and the USPDC is the primary optical noise source. However, I made several improvements to the 2nd generation UCD, which resulted in an improved performance than a conventional direct detector when employed in an atmospheric lidar application. To be more specific, the étendue of the new UCD was around 3 times larger and the intracavity pump power was improved by a factor of 3. Most importantly, instead of using a linear cavity, a ring cavity that enabled single longitudinal mode lasing of the 1064 nm pump was used in this new module.

Another focus of my project is to investigate the noise properties of the UCD. Firstly, the beat noise due to the coherent beating between the different longitudinal modes in the 1064 nm laser was studied. The experimental results proved that a UCD with a multi-longitudinal mode pump had a non-uniform frequency response, which narrowed down the detection bandwidth. In contrast, the 2nd generation UCD can operate with a single longitudinal mode benefiting from the ring-laser cavity design. Therefore, the detection bandwidth of the UCD is larger than 1 GHz. Moreover, the detection bandwidth of the current system is limited by the Si based detector, and there is no fundamental limit for even faster detection as long as the bandwidth of the Si detector is large enough. Secondly, a single-pass, short-wavelength-pumped upconversion detector was built in order to study the noise property of the UCD in more detail. The theoretical model for the USPDC, the SHG-SPDC and the upconverted thermal radiation were established accordingly. Due to the poling error (mostly the RDC error) of the PPLN crystal, the non-phase-matched SPDC and SHG processes are strongly enhanced. Afterwards, the SPDC photon and the SHG photon are capable of upconversion and downconversion satisfying the QPM condition, which makes them the primary noise sources of the UCDs. The USPDC noise photon has the same wavelength as the upconverted signal. Thus, it cannot be removed by using a narrow spectral bandpass filter. In contrast, the SHG-SPDC photon usually has a different wavelength compared to the upconverted signal. Therefore, it can be avoided by choosing a correct combination of poling period, working temperature and bandpass filters. It is worth pointing out that, to our best knowledge, it was the first time that the SHG-SPDC was identified as a potential noise source in the UCD. The upconverted thermal radiation becomes the primary noise source of the UCDs if $\lambda_s > 3$ µm, especially when the temperature of the PPLN

crystal is high. Experimentally, it is impossible to separate the noise contribution of the USPDC from the upconverted thermal radiation quantitatively. But the theoretical model shows that the noise from the thermal radiation can be neglected when $\lambda_s < 1.7\,\mu m$ and the USPDC noise can be neglected when $\lambda_s > 4\,\mu m$. Thirdly, the upconverted SRS noise of an intracavity-enhanced, long-wavelength-pumped UCD was measured. As a potential strategy for noise reduction, a PPLN waveguide-based UCD was characterized with a DCR of $\sim 1 \times 10^2/s$ in the literature. On the contrary, the DCR of a PPLN bulk crystal was $> 1 \times 10^3/s$. Considering that the intensity of SRS is proportional to the pump power and the pump power in the bulk PPLN based UCD was around 500 times larger than that of the waveguide UCD, it was reasonable that the measured DCR in the former is around 2 orders of magnitude higher than in the latter. Additionally, the intensity of Raman scattering is strongly affected by the frequency shift ($\Delta\nu$). The DCR given by our long-wavelength-pumped UCD was around $5 \times 10^5/s$ when $\lambda_s = 1645\,nm$, which was comparable to that measured in the short-wavelength-pumped UCD. Therefore, the performance of the long-wavelength-pumped UCD is worse than the short-wavelength-pumped system when $\lambda_s > 1645\,\mu m$, especially considering the lower detection efficiency of Si based detector at the upconverted signal ($\lambda_{up} = 900\,nm$).

During the noise property investigation of the short-wavelength-pumped system, 2D ring patterns were observed when the noise photon generated inside the UCD was measured with a high sensitivity camera. Further study showed that the ring pattern originates from the unique spatial distribution of the USPDC noise. Based on this discovery, a new strategy for noise reduction was proposed: combining the noncollinear upconversion with a spatial filter, the SNR can be improved when the signal is collected from the local minimum of the ring pattern in figure 4.20. In the experiment, this strategy resulted in a 14 dB reduction of the DCR with only a 2.2 dB penalty for the signal.

The last part of my project was to test and prove the potential of the UCD in an atmospheric lidar application. Following the similar procedures of measuring the atmospheric CO_2 with the 1st generation UCD, the atmospheric CH_4 was measured by our 2nd generation UCD, wherein the CHARM-F system (DLR's atmospheric lidar system for CO_2 and CH_4 gas sensing) was still used as the light source and the data acquisition device. The measurement results shown that the DAOD provided by our new UCD yielded a relative error of less than 11 % at ranges between 3 and 9 km, and the new UCD managed to outperform an APD by a factor of 2 to 4 in terms of SNR.

6.2 Outlook

After three years of research work on the upconversion technology, I gained a lot of theoretical knowledge and experimental experience about this research area. Most importantly, I have a deeper understanding about the value of upconversion technology to the scientific community. At the end of my Ph.D project, I would like to share my vision about the potential improvement on the upconversion detection and its future applications.

Further Improvement of the UCD

Benefiting from the experience of the 1st generation UCD, the 2nd generation UCD managed to outperform the conventional APD in the DIAL measurement. It was a

step forward in the exploration of the potential of upconversion technology in atmospheric lidar applications, but I believe more improvements can still be achieved with a proper design. 1) Due to the development of fabrication techniques, the quality of PPLNs with larger aperture (e.g 2 mm×2 mm) has be improved significantly. Therefore, pumping with a larger beam size ($\omega_0 \approx 400\,\mu m$) becomes possible, which will enlarge the étendue of the detection system further. Meanwhile, a higher pump power is needed in order to maintain the high upconversion efficiency. 2) In the 2nd generation UCD, an 808 nm LD was chosen as the optical pump for the 1064 nm Nd:YVO_4 laser yielding $\sim 150\,W$ power for the upconversion pump. However, due to the thermal lensing effect, it becomes challenging to continue increasing the pump power by simply increasing the 808 nm power. In future laser design, an Nd:YVO_4 slab laser or an LD pumped at other wavelengths (880 nm or 916 nm) should be considered in order to obtain a high 1064 nm pump power for the upconversion. 3) Instead of using a bulk PPLN crystal as the $\chi^{(2)}$ material, a PPKTP crystal is a better choice in terms of USPDC noise reduction since the PPKTP crystal has much smaller RDC error [109]. Even though the d_{eff} of PPKTP ($\sim 10\,pm/V$) is smaller than that of the PPLN ($\sim 16\,pm/V$), PPKTP has a smaller refractive index. Based on equations 2.11, both crystals will have comparable upconversion efficiency if they work under the same conditions. However, a smaller refractive index will limit the étendue, which should be considered when the overall performance of the system is being evaluated.

Other Potential Applications using the UCD

The UCD shown in this thesis can be easily adapted to the other detection wavelength ranges. Additionally, this UCD has a high detection bandwidth, which makes it a potential candidate for applications where high-speed detection is necessary such as free space optical communication. In principle, this UCD can significantly improve the performance of the system wherein a MIR signal is being detected.

For the short-term application, we can deepen the cooperation with DLR in the field of atmospheric sensing. In Chapter 5, our 2nd generation UCD outperformed the conventional direct detector in a DIAL measurement. However, that experiment was a just proof of concept since only the DAOD was obtained back then. In the future cooperation with DLR, more well designed field tests can be arranged in order to get range-resolved CH_4 or CO_2 (using a different PPLN channel) mixing ratio in the atmosphere over long distance. In addition, with further improvement based on the knowledge we acquired during the development of the 2nd generation UCD, our 3rd generation UCD can have higher sensitivity and become more compatible with the CHARM-F system. Thus, even better performance in the CH_4 or CO_2 DIAL measurement is expected.

For the long-term application, atmospheric sensing based on the UCD can be extended to other absorption lines of different gases, such as CO_2 (2.1 µm), CH_4 (2.3 µm), N_2O (3.9 µm) [97], CO (4.7 µm) [110], C_3H_8 (3.39 µm), SO_2 (3.98 µm) and NO (5.2 µm) [105]. It is necessary to emphasize that UCDs has massive advantage compared to the conventional direct detector working in the MIR region. In addition, instead of pursuing the measurement over long distance, short-distance sensing is more realistic since some gas species have much stronger absorption in this spectral region.

Appendix A

Derivation of $|\widetilde{g}(\Delta k)|^2$

The structure of the PPLN crystal with a particular duty cycle and RDC error is shown in figure 2.9. The crystal has N domains and the position of the boundary is labeled as z_i, $i = 0, 1 \ldots N$. The poling period is Λ, the duty cycle is D and the randomness of the boundary position follows a Gaussian distribution with a standard deviation of σ_z. The Fourier transform of $g(z)$ is

$$\begin{aligned}
\widetilde{g}(\Delta k) &= \mathcal{F}\{g(z)\} \\
&= \int_L dz g(z) exp(i\Delta k z) \\
&= \sum_{n=1}^{N} \int_{z_{n-1}}^{z_n} (-1)^n exp(i\Delta k z) dz \\
&= \sum_{n=1}^{N} \frac{(-1)^n exp(i\Delta k z)}{i\Delta k} \Big|_{z_{n-1}}^{z_n} \\
&\approx 2 \sum_{n=1}^{N} \frac{(-1)^n exp(i\Delta k z_n)}{i\Delta k} \\
&= 2 \sum_{n=1}^{N} \frac{exp[i(\Delta k z_n + n\pi)]}{i\Delta k} \\
&= 2 \sum_{n=1}^{N} \frac{exp(i\Phi_n)}{i\Delta k},
\end{aligned} \tag{A.1}$$

where $\Phi_n = \Delta k z_n + n\pi$. Then $|\widetilde{g}(\Delta k)|^2$ is

$$\begin{aligned}
|\widetilde{g}(\Delta k)|^2 &= \frac{4}{\Delta k^2} \sum_{n=1}^{N} \sum_{m=1}^{N} exp[i(\Phi_n - \Phi_m)] \\
&= \frac{4}{\Delta k^2} (N + \sum_{n=1}^{N} \sum_{m \neq n}^{N} exp[i(\Phi_n - \Phi_m)]) \\
&= \frac{4}{\Delta k^2} (N + \sum_{n=1}^{N} \sum_{m=n+1}^{N} exp[i(\Phi_n - \Phi_m)] + exp[i(\Phi_m - \Phi_n)]) \\
&= \frac{4}{\Delta k^2} [N + 2 \sum_{n=1}^{N} \sum_{p=1}^{N-n} cos(\Phi_n - \Phi_{n+p})].
\end{aligned} \tag{A.2}$$

Define $\Phi_{n+p} - \Phi_n$ as

$$\begin{aligned}\Delta\Phi_{n,p} &= \Phi_{n+p} - \Phi_n \\ &= \Delta k(z_{n+p} - z_n) + (n+p-n)\pi \\ &= \Delta k(z_{n+p} - z_n) + p\pi \\ &= p(\Delta k l + \pi) + h(n,p) \\ &= p\theta + h(n,p) + \delta z_{p+n} + \delta z_p,\end{aligned} \tag{A.3}$$

where

$$\begin{aligned}\theta &= \Delta k l + \pi \\ l &= \Lambda/2 \\ h(n,p) &= \begin{cases} 0, \text{ |n-p| is even} \\ \delta, \text{ |n-p| is odd and n is even} \\ -\delta, \text{ |n-p| is odd and n is odd} \end{cases} \\ \delta &= \Delta k \Lambda(D - 0.5), D \in [0\ 0.5].\end{aligned} \tag{A.4}$$

The average of $cos(\Delta\Phi_{n,p})$ can be calculated as

$$< cos(\Delta\Phi_{n,p}) >= exp(-\frac{\sigma^2}{2}) cos[p\theta + h(n,p)], \tag{A.5}$$

where

$$\begin{aligned}< \Delta\Phi_{n,p} > &= p\theta + h(n,p) \\ \sigma^2 &= 2\Delta k^2 \sigma_z^2.\end{aligned} \tag{A.6}$$

The elements in $\sum_{n=1}^{N}\sum_{p=1}^{N-n} cos[p\theta + h(n,p)]$ are rearranged as shown in table A.1. Thus,

$$\begin{aligned}< \sum_{n=1}^{N}\sum_{p=1}^{N-n} cos[p\theta + h(n,p)] > &= \sum_{n=1}^{N}\sum_{p=1}^{N-n} < cos[p\theta + h(n,p)] > \\ &= exp(-\frac{\sigma^2}{2}) \sum_{n=1}^{N}\sum_{p=1}^{N-n} cos(p\theta) \\ &= exp(-\frac{\sigma^2}{2}) \sum_{j=1}^{N/2} \{(N-2j)cos(2j\theta) + (N/2-j)cos[(2j-1)\theta + \delta] \\ &\quad + (N/2+1-j)cos[(2j-1)\theta - \delta]\} \\ &= exp(-\frac{\sigma^2}{2})\{-\frac{N}{2} + \frac{(1-cosN\theta)[1+cos(\theta-\delta)]}{2sin^2\theta}\}.\end{aligned} \tag{A.7}$$

Substituting equation A.7 into equation A.2 gives

$$\begin{aligned}|\widetilde{g}(\Delta k)|^2 &= \frac{4N}{\Delta k^2}[1 - exp(-\frac{\sigma^2}{2})] + \frac{4}{\Delta k^2} exp(-\frac{\sigma^2}{2}) \frac{(1-cosN\theta)[1+cos(\theta-\delta)]}{2sin^2\theta} \\ &= \frac{2L}{\Delta k^2 \Lambda}[1 - exp(-\Delta k^2 \sigma_z^2)] \\ &\quad + \frac{4}{\Delta k^2} exp(-\Delta k^2 \sigma_z^2) \frac{(1 - cos\frac{\Delta k L}{2})\{1 - cos[\Delta k \Lambda(1-D)]\}}{sin^2 \frac{\Delta k \Lambda}{2}}.\end{aligned} \tag{A.8}$$

n\p	1	2	3	4	.	.	.	N-3	N-2	N-1	N
1	$cos(\theta-\delta)$	$cos(2\theta)$	$cos(3\theta-\delta)$	$cos(4\theta)$	.	.	.	$cos[(n-3)\theta+\delta]$	$cos[(n-2)\theta]$	$cos[(n-1)\theta-\delta]$	0
2	$cos(\theta+\delta)$	$cos(2\theta)$	$cos(3\theta+\delta)$	$cos(4\theta)$	.	.	.	$cos[(n-3)\theta-\delta]$	$cos[(n-2)\theta]$	0	
3	$cos(\theta-\delta)$	$cos(2\theta)$	$cos(3\theta-\delta)$	$cos(4\theta)$	.	.	.	$cos[(n-3)\theta+\delta]$	0		
4	$cos(\theta+\delta)$	$cos(2\theta)$	$cos(3\theta+\delta)$	$cos(4\theta)$	.	.	.	0			
.	.	.	.	.							
.	.	.	.	.							
.	.	.	.	.							
N-3	$cos(\theta-\delta)$	$cos(2\theta)$	$cos(3\theta-\delta)$	0							
N-2	$cos(\theta+\delta)$	$cos(2\theta)$	0								
N-1	$cos(\theta-\delta)$	0									
N	0										

TABLE A.1: $\Sigma_{n=1}^{N}\Sigma_{p=1}^{N-n} cos[p\theta + h(n,p)]$

Appendix B

Poster Presented at DOPS 2016

Appendix C

Poster at CLEO Europe 2017

Intracavity Upconversion for IR Absorption Lidar: Comparison of Linear and Ring Cavity Designs

Lichun Meng[1], Lasse Hoegstedt[2], Peter Tidemand-Lichtenberg[1], Christian Pedersen[1], and Peter John Rodrigo[1]

[1]*DTU Fotonik, Technical University of Denmark, Frederiksborgvej 399, 4000 Roskilde, Denmark*

[2]*IRSee ApS, Frederiksborgvej 399, 4000 Roskilde, Denmark*

Introduction

❑ Upconversion Technology

Upconversion detection is a promising technology for measuring infrared (IR) lidar signals [1-2]. In comparison to conventional InGaAs detectors, the upconversion detector can achieve IR detection with better signal-to-noise ratio (SNR), not only due to lower dark noise directly, but also because of its limited field-of-view and acceptance bandwidth that result in a much lower background noise. **Fig. 1** shows a typical structure of the upconversion detector.

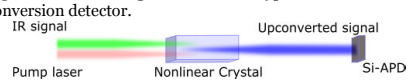

Fig. 1. Schematic diagram of the upconversion detection principle.

❑ Principle of Upconversion

Frequency upconversion relies on sum-frequency generation (SFG) process between the IR signal and a pump in a nonlinear material. The process follows the principle of energy conservation:

$$\hbar\omega_{IR} + \hbar\omega_{pump} = \hbar\omega_{up}$$

Periodically poled lithium niobate (PPLN) is a commonly used nonlinear material that permits high efficiency for the frequency upconversion process. The poling period of the crystal is fabricated to fulfill the quasi phase-matching condition:

$$\vec{k}_{IR} + \vec{k}_{pump} - \vec{k}_{up} = \pm 2\pi/\Lambda;\ \Lambda \text{ is the PPLN poling period.}$$

Experiment & Results

Intracavity pumping is typically used to achieve a sufficiently strong (e.g. 1064 nm) pump field. We investigated both the linear and the ring cavity designs for upconversion of 1.55 μm signals to 631 nm.

❑ Linear Cavity

The linear cavity (**Fig. 2**) is simple and easy to assemble. The thermal lensing effect can be compensated by changing the cavity length. In our setup, the surface coating on opposite ends of the PPLN has a reflectivity of 0.6%, which contributes a total round trip loss of 2.4%. It also tends to operate with multilongitudinal modes due to spatial hole burning.

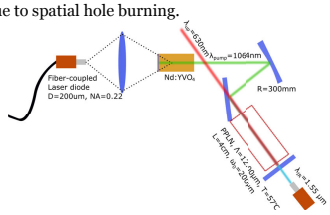

Fig. 2. Upconversion detector based on linear cavity.

❑ Ring Cavity

The ring cavity we constructed (**Fig. 3**) has a relatively more complex structure, but it operates unidirectionally. The coating on the PPLN surfaces only contributes a loss of 1.2%, but a Faraday rotator crystal (TGG) and a half-wave plate introduce additional losses. The ring cavity is easy to run in single longitudinal mode.

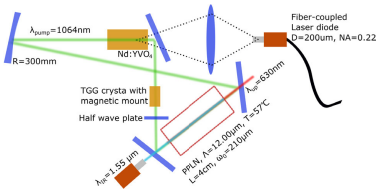

Fig. 3. Upconversion detector based on ring cavity.

❑ Upconversion Efficiency

Quantum efficiencies of the linear and the ring cavity based upconverters as a function of intracavity pump power is shown in **Fig. 4**.

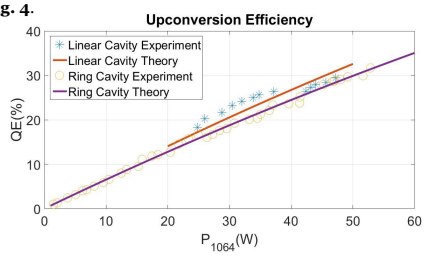

Fig. 4. Upconversion efficiency versus intracavity pump power.

❑ Single and multilongitudinal mode pumping

In our experiment, we observed that only the ring cavity can achieve single longitudinal mode pumping. Multilongitudinal mode pumping can cause fluctuation of the pump power, which introduces additional noise for high-bandwidth signal detection [3]. **Fig. 5** shows modulated IR signal detection via upconversion and compares multi and single longitudinal mode pumping scenarios.

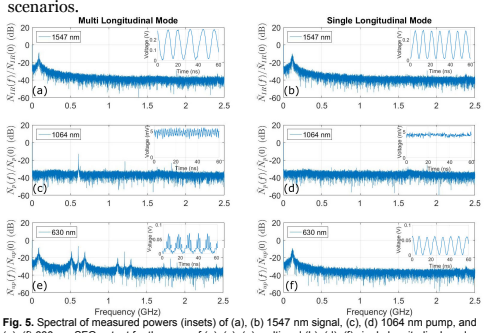

Fig. 5. Spectral of measured powers (insets) of (a), (b) 1547 nm signal, (c), (d) 1064 nm pump, and (e), (f) 630 nm SFG output for the case of (a), (c), (e) multi and (b), (d), (f) single longitudinal mode pump.

Conclusion

- Two intracavity setups (linear and ring cavity) for upconversion detection of 1.55 μm signals were tested.
- The linear cavity was only able to operate in a certain pump power range because of thermal lensing effect.
- The measured maximum conversion efficiency of the linear and the ring cavity based detectors were 30% and 32%, respectively.
- Pump power (and hence, conversion efficiency) fluctuations due to multilongitudinal pump mode beating could introduce additional noise for high-bandwidth detection.
- Only the ring cavity based upconversion detector was able to operate in single longitudinal mode pumping condition.

References

[1] H. Xia, G. Shentu, M. Shangguan, X. Xia, X. Jia, C. Wang, J. Zhang, J. S. Pelc, M. M. Fejer, Q. Zhang, X. Dou, and J.-W. Pan, "Long-range micro-pulse aerosol lidar at 1.5 μm with an upconversion single-photon detector," Opt. Lett. **40**, 1579-1582 (2015).

[2] T. Wong, J. Yu, Y. Bai, W. Johnson, S. Chen, M. Petros, and U. N. Singh, "Sensitive infrared signal detection by upconversion technique," Opt. Eng. **53**, 107102 (2014).

[3] L. Meng, L. Høgstedt, P. Tidemand-Lichtenberg, C. Pedersen, and P. J. Rodrigo, "GHz-bandwidth upconversion detector using a unidirectional ring cavity to reduce multilongitudinal mode pump effects," Opt. Express **25**, 14783-14794 (2017).

Funding: Mid-TECH – H2020-MSCA-ITN-2014 (642661).

Bibliography

[1] Newport. *Technical Note: Optical Detection Systems*. https://www.newport.com/n/optical-detection-systems. (accessed 19-May-2018).

[2] H. P. Weber, E. Mathieu, and K. P. Meyer. "Optical mixing with different relative polarization of the beams". In: *Journal of Applied Physics* 9 (1966), pp. 3584–3586.

[3] P. A. Franken et al. "Generation of optical harmonics". In: *Phys. Rev. Lett.* (1961), pp. 118–119.

[4] D. A. Kleinman. "Nonlinear dielectric polarization in optical media". In: *Phys. Rev.* (1962), pp. 1977–1979.

[5] J. A. Armstrong et al. "Interactions between light waves in a nonlinear dielectric". In: *Phys. Rev.* (1962), pp. 1918–1939.

[6] G. D. Boyd and D. A. Kleinman. "Parametric interaction of focused Gaussian light beams". In: *Journal of Applied Physics* 8 (1968), pp. 3597–3639.

[7] J. E. Midwinter and J. Warner. "Up-conversion of near infrared to visible radiation in Lithium-meta-Niobate". In: *Journal of Applied Physics* 2 (1967), pp. 519–523.

[8] J. E. Midwinter. "Image conversion from 1.6 μm to the visible in Lithium Niobate". In: *Applied Physics Letters* 3 (1968), pp. 68–70.

[9] J. A. Giordmaine and R. C. Miller. "Tunable coherent parametric oscillation in $LiNbO_3$ at optical frequencies". In: *Phys. Rev. Lett.* (1965), pp. 973–976.

[10] C. K. N. Patel. "Parametric amplification in the far infrared". In: *Applied Physics Letters* 9 (1966), pp. 332–334.

[11] R. L. Byer and S. E. Harris. "Power and bandwidth of spontaneous parametric emission". In: *Phys. Rev.* (1968), pp. 1064–1068.

[12] T. G. Giallorenzi and C. L. Tang. "Quantum theory of spontaneous parametric scattering of intense light". In: *Phys. Rev.* (1968), pp. 225–233.

[13] C. L. Tang. "Spontaneous emission in the frequency up-conversion process in nonlinear optics". In: *Phys. Rev.* (1969), pp. 367–374.

[14] T. R. Gurski, H. W. Epps, and S. P. Maran. "Astronomical demonstration of an infrared upconverter". In: *Nature* (1974), p. 638.

[15] R. W. Boyd. "Infrared upconversion for astronomy". In: *Optical Engineering* (1977), pp. 16 –16 –6.

[16] J. Falk and Y. C. See. "Internal cw parametric upconversion". In: *Applied Physics Letters* 2 (1978), pp. 100–101.

[17] K. R. Parameswaran et al. "Highly efficient second-harmonic generation in buried waveguides formed by annealed and reverse proton exchange in periodically poled lithium niobate". In: *Opt. Lett.* 3 (2002), pp. 179–181.

[18] R. V. Roussev et al. "Periodically poled lithium niobate waveguide sum-frequency generator for efficient single-photon detection at communication wavelengths". In: *Opt. Lett.* 13 (2004), pp. 1518–1520.

[19] H. Pan and H. Zeng. "Efficient and stable single-photon counting at 1.55 μm by intracavity frequency upconversion". In: *Opt. Lett.* 6 (2006), pp. 793–795.

[20] H. Pan et al. "Single-photon frequency up-conversion with multimode pumping". In: *Phys. Rev. A* (2008), p. 033815.

[21] H. Pan et al. "Efficient single-photon counting at 1.55 μm by intracavity frequency upconversion in a unidirectional ring laser". In: *Applied Physics Letters* 19 (2006), p. 191108.

[22] H. Dong et al. "Efficient single-photon frequency upconversion at 1.06 μm with ultralow background counts". In: *Applied Physics Letters* 7 (2008), p. 071101.

[23] J. S. Pelc et al. "Efficiency pedestal in quasi-phase-matching devices with random duty-cycle errors". In: *Opt. Lett.* 6 (2011), pp. 864–866.

[24] J. S. Pelc et al. "Influence of domain disorder on parametric noise in quasi-phase-matched quantum frequency converters". In: *Opt. Lett.* 16 (2010), pp. 2804–2806.

[25] J. S. Pelc et al. "Long-wavelength-pumped upconversion single-photon detector at 1550 nm: performance and noise analysis". In: *Opt. Express* 22 (2011), pp. 21445–21456.

[26] G.-L. Shentu et al. "Ultralow noise up-conversion detector and spectrometer for the telecom band". In: *Opt. Express* 12 (2013), pp. 13986–13991.

[27] H. Xia et al. "Long-range micro-pulse aerosol lidar at 1.5 μm with an upconversion single-photon detector". In: *Opt. Lett.* 7 (2015), pp. 1579–1582.

[28] M. Shangguan et al. "All-fiber upconversion high spectral resolution wind lidar using a Fabry-Perot interferometer". In: *Opt. Express* 17 (2016), pp. 19322–19336.

[29] H. Xia et al. "Micro-pulse upconversion Doppler lidar for wind and visibility detection in the atmospheric boundary layer". In: *Opt. Lett.* 22 (2016), pp. 5218–5221.

[30] H. Xia et al. "Brillouin optical time-domain reflectometry using up-conversion single-photon detector". In: *Optics Communications* (2016), pp. 37 –42. ISSN: 0030-4018.

[31] R. Baudoin et al. "Sum frequency generation process for a new astronomical instrument". In: *Proc.SPIE* (2014), pp. 8964 –8964 –9.

[32] J. S. Dam, C. Pedersen, and P. Tidemand-Lichtenberg. "High-resolution two-dimensional image upconversion of incoherent light". In: *Opt. Lett.* 22 (2010), pp. 3796–3798.

[33] J. S. Dam, P. Tidemand-Lichtenberg, and C. Pedersen. "Room-temperature mid-infrared single-photon spectral imaging". In: *Nature Photonics* (2012), p. 788.

[34] Q. Hu et al. "High-resolution mid-IR spectrometer based on frequency upconversion". In: *Opt. Lett.* 24 (2012), pp. 5232–5234.

[35] L. M. Kehlet et al. "Infrared upconversion hyperspectral imaging". In: *Opt. Lett.* 6 (2015), pp. 938–941.

[36] L. Høgstedt et al. "Low-noise mid-IR upconversion detector for improved IR-degenerate four-wave mixing gas sensing". In: *Opt. Lett.* 18 (2014), pp. 5321–5324.

[37] L. Huot et al. "Upconversion imaging using an all-fiber supercontinuum source". In: *Opt. Lett.* 11 (2016), pp. 2466–2469.

[38] P. Tidemand-Lichtenberg et al. "Mid-infrared upconversion spectroscopy". In: *J. Opt. Soc. Am. B* 11 (2016), pp. D28–D35.

[39] M. Mathez et al. "Upconversion imaging using short-wave infrared picosecond pulses". In: *Opt. Lett.* 3 (2017), pp. 579–582.

[40] A. Barh, C. Pedersen, and P. Tidemand-Lichtenberg. "Ultra-broadband mid-wave-IR upconversion detection". In: *Opt. Lett.* 8 (2017), pp. 1504–1507.

[41] A. Barh, P. Tidemand-Lichtenberg, and C. Pedersen. "Thermal noise in mid-infrared broadband upconversion detectors". In: *Opt. Express* 3 (2018), pp. 3249–3259.

[42] S. Junaid et al. "Mid-infrared upconversion based hyperspectral imaging". In: *Opt. Express* 3 (2018), pp. 2203–2211.

[43] Y.-P. Tseng, C. Pedersen, and P. Tidemand-Lichtenberg. "Upconversion detection of long-wave infrared radiation from a quantum cascade laser". In: *Opt. Mater. Express* 5 (2018), pp. 1313–1321.

[44] T.-H. Wong et al. "Sensitive infrared signal detection by upconversion technique". In: *Optical Engineering* (2014), pp. 53 –53 –6.

[45] L. Høgstedt et al. "Upconversion-based lidar measurements of atmospheric CO2". In: *Opt. Express* 5 (2016), pp. 5152–5161.

[46] R. W. Boyd. *Nonlinear Optics, Third Edition*. 3rd. Orlando, FL, USA: Academic Press, Inc., 2008. ISBN: 0123694701, 9780123694706.

[47] K. Rottwitt and P. Tidemand-Lichtenberg. *Nonlinear Optics: Principles and Applications*. CRC Press, 2014. ISBN: 978-1-4665-6582-1.

[48] D. G. M. Richard Lee Sutherland and S. Kirkpatrick. *Handbook of nonlinear optics*. 2nd ed, Revised and Expanded. New York : Marcel Dekker, 2003. ISBN: 0824742435.

[49] C. Pedersen et al. "Non-collinear upconversion of infrared light". In: *Opt. Express* 23 (2014), pp. 28027–28036.

[50] J. E. Pearson, A. Yariv, and U. Ganiel. "Observations of parametric fluorescence and oscillation in the infrared". In: *Appl. Opt.* 6 (1973), pp. 1165–1171.

[51] J. E. Midwinter and J. Warner. "The effects of phase matching method and of uniaxial crystal symmetry on the polar distribution of second-order nonlinear optical polarization". In: *British Journal of Applied Physics* 8 (1965), p. 1135.

[52] J. D. McMullen. "Optical parametric interactions in isotropic materials using a phase corrected stack of nonlinear dielectric plates". In: *Journal of Applied Physics* 7 (1975), pp. 3076–3081.

[53] A. Szilagyi, A. Hordvik, and H. Schlossberg. "A quasi phase matching technique for efficient optical mixing and frequency doubling". In: *Journal of Applied Physics* 5 (1976), pp. 2025–2032.

[54] K. Rustagi, S. Mehendale, and S. Meenakshi. "Optical frequency conversion in quasi phase matched stacks of nonlinear crystals". In: *IEEE Journal of Quantum Electronics* 6 (1982), pp. 1029–1041. ISSN: 0018-9197.

[55] R. A. Andrews, H. Rabin, and C. L. Tang. "Coupled parametric downconversion and upconversion with simultaneous phase matching". In: *Phys. Rev. Lett.* (1970), pp. 605–608.

[56] Z. G. Figen and O. Aytür. "Nanosecond sum-frequency generating optical parametric oscillator using simultaneous phase matching". In: *Opt. Express* 13 (2005), pp. 4896–4902.

[57] Z. G. Figen, A. Yalabik, and O. Aytur. "Highly efficient wavelength conversion of Q-switched Nd:YAG lasers into a red wavelength". In: *IEEE Journal of Quantum Electronics* 7 (2006), pp. 706–712. ISSN: 0018-9197.

[58] X. Zhang, Y. Men, and L. Wang. "Simultaneously phase-matched parametric processes in a single-pass interaction for efficient visible generation". In: *Optics Communications* 16 (2010), pp. 3184 –3188. ISSN: 0030-4018.

[59] D. Eimerl et al. "Optical, mechanical, and thermal properties of barium borate". In: *Journal of Applied Physics* 5 (1987), pp. 1968–1983.

[60] R. S. Weis and T. K. Gaylord. "Lithium niobate: Summary of physical properties and crystal structure". In: *Applied Physics A* 4 (1985), pp. 191–203. ISSN: 1432-0630.

[61] D. A. Bryan, R. Gerson, and H. E. Tomaschke. "Increased optical damage resistance in lithium niobate". In: *Applied Physics Letters* 9 (1984), pp. 847–849.

[62] I. E. Barry et al. "Microstructuring of lithium niobate using differential etch-rate between inverted and non-inverted ferroelectric domains". In: *Materials Letters* 4 (1998), pp. 246 –254. ISSN: 0167-577X.

[63] H. Ishizuki and T. Taira. "High energy quasi phase matched optical parametric oscillation in a periodically poled MgO:$LiNbO_3$ device with a 5 mm$\times$5 mm aperture". In: *Opt. Lett.* 21 (2005), pp. 2918–2920.

[64] M. M. Fejer et al. "Quasi-phase-matched second harmonic generation: tuning and tolerances". In: *IEEE Journal of Quantum Electronics* 11 (1992), pp. 2631–2654. ISSN: 0018-9197.

[65] H. photonics Corp. http://www.hcphotonics.com/products.asp?area=1670&cat=1750. [Online; accessed 29-May-2018]. 2018 (accessed 29-May-2018).

[66] Covesion-Ltd. https://www.covesion.com/. [Online; accessed 29-May-2018]. 2018 (accessed 29-May-2018).

[67] O. Gayer et al. "Temperature and wavelength dependent refractive index equations for MgO doped congruent and stoichiometric $LiNbO_3$". In: *Applied Physics B* 2 (2008), pp. 343–348. ISSN: 1432-0649.

[68] X. Délen et al. "Characteristics of laser operation at 1064 nm in Nd:YVO4 under diode pumping at 808 and 914 nm". In: *J. Opt. Soc. Am. B* 1 (2011), pp. 52–57.

[69] M. Imaki and T. Kobayashi. "Infrared frequency upconverter for high-sensitivity imaging of gas plumes". In: *Opt. Lett.* 13 (2007), pp. 1923–1925.

[70] L. Meng et al. "GHz-bandwidth upconversion detector using a unidirectional ring cavity to reduce multilongitudinal mode pump effects". In: *Opt. Express* 13 (2017), pp. 14783–14794.

[71] C. Langrock et al. "Highly efficient single-photon detection at communication wavelengths by use of upconversion in reverse-proton-exchanged periodically poled $LiNbO_3$ waveguides". In: *Opt. Lett.* 13 (2005), pp. 1725–1727.

[72] M. A. Albota and F. N. C. Wong. "Efficient single-photon counting at 1.55 μm by means of frequency upconversion". In: *Opt. Lett.* 13 (2004), pp. 1449–1451.

[73] J. S. Pelc et al. "Up-conversion of optical signals with multi-longitudinal-mode pump lasers". In: *Phys. Rev. A* (2012), p. 033827.

[74] K.-D. F. Büchter et al. "All-optical Ti:PPLN wavelength conversion modules for free-space optical transmission links in the mid-infrared". In: *Opt. Lett.* 4 (2009), pp. 470–472.

[75] R. Martini et al. "High-speed modulation and free-space optical audio/video transmission using quantum cascade lasers". In: *Electronics Letters* 3 (2001), pp. 191–193. ISSN: 0013-5194.

[76] R. Paiella et al. "Generation and detection of high-speed pulses of mid-infrared radiation with intersubband semiconductor lasers and detectors". In: *IEEE Photonics Technology Letters* 7 (2000), pp. 780–782. ISSN: 1041-1135.

[77] P. M. Henry et al. "HgCdTe photodiodes for heterodyne applications". In: *Proc.SPIE* (1986), pp. 0663 –0663 –10.

[78] J. Q. Zhao et al. "High efficiency, single-frequency continuous wave Nd:YVO_4 ring laser". In: *Laser Physics Letters* 2 (2010), p. 135.

[79] M. Mancinelli et al. "Mid-infrared coincidence measurements on twin photons at room temperature". In: *Nature Communications* (2017). Article, p. 15184.

[80] P. S. Kuo et al. "Using temperature to reduce noise in quantum frequency conversion". In: *Opt. Lett.* 9 (2018), pp. 2034–2037.

[81] K. Koch et al. "Hot spots in parametric fluorescence with a pump beam of finite cross section". In: *IEEE Journal of Quantum Electronics* 5 (1995), pp. 769–781. ISSN: 0018-9197.

[82] S. Wolf et al. "Upconversion-enabled array spectrometer for the mid-infrared, featuring kilohertz spectra acquisition rates". In: *Opt. Express* 13 (2017), pp. 14504–14515.

[83] L. E. Estes et al. "Internal thermal noise in optical frequency converters". In: *J. Opt. Soc. Am.* 3 (1974), pp. 295–300.

[84] P. Kumar. "Quantum frequency conversion". In: *Opt. Lett.* 24 (1990), pp. 1476–1478.

[85] P. S. Kuo et al. "Reducing noise in single-photon-level frequency conversion". In: *Opt. Lett.* 8 (2013), pp. 1310–1312.

[86] B.-Q. Yao et al. "Comparison of Tm:YLF and Tm:YAP in thermal analysis and laser performance". In: *J. Opt. Soc. Am. B* 8 (2011), pp. 1866–1873.

[87] F. Ma et al. "1.064-μm-band up-conversion single-photon detector". In: *Opt. Express* 13 (2017), pp. 14558–14564.

[88] L. Meng et al. "Enhancing the detectivity of an upconversion single-photon detector by spatial filtering of upconverted parametric fluorescence". In: *Opt. Express* 19 (2018), pp. 24712–24722.

[89] C. R. Phillips, J. S. Pelc, and M. M. Fejer. "Parametric processes in quasi-phasematching gratings with random duty cycle errors". In: *J. Opt. Soc. Am. B* 4 (2013), pp. 982–993.

[90] L. Meng et al. "Upconversion detector for range-resolved DIAL measurement of atmospheric CH_4". In: *Opt. Express* 4 (2018), pp. 3850–3860.

[91] A. Korneev et al. "Quantum efficiency and noise equivalent power of nanostructured, NbN, single-photon detectors in the wavelength range from visible to infrared". In: *IEEE Transactions on Applied Superconductivity* 2 (2005), pp. 571–574. ISSN: 1051-8223.

[92] Y. L. Lee et al. "Bandwidth control of a Ti:PPLN Solc filter by a temperature-gradient-control technique". In: *Opt. Express* 18 (2008), pp. 13699–13706.

[93] A. Bostani, A. Tehranchi, and R. Kashyap. "Super-tunable, broadband up-conversion of a high-power CW laser in an engineered nonlinear crystal". In: *Sci Rep* 1 (2017), pp. 883–883. ISSN: 2045-2322.

[94] IPCC. *Climate Change 2013: the physical science basis. Contribution of working group I to the fifth assessment report of the intergovernmental panel on climate change*. Cambridge, United Kingdom and New York, NY, USA: Cambridge University Press, 2013, p. 1535. ISBN: ISBN 978-1-107-66182-0.

[95] K. J. Mach et al. "Understanding and responding to danger from climate change: the role of key risks in the IPCC AR5". In: *Climatic Change* 3 (2016), pp. 427–444. ISSN: 1573-1480.

[96] M Saunois et al. "The growing role of methane in anthropogenic climate change". In: *Environmental Research Letters* 12 (2016), p. 120207.

[97] G. Ehret et al. "Space-borne remote sensing of CO_2, CH_4, and N_2O by integrated path differential absorption lidar: a sensitivity analysis". In: *Applied Physics B* 3 (2008), pp. 593–608. ISSN: 1432-0649.

[98] A. Amediek et al. "CHARM-F a new airborne integrated-path differential-absorption lidar for carbon dioxide and methane observations: measurement performance and quantification of strong point source emissions". In: *Appl. Opt.* 18 (2017), pp. 5182–5197.

[99] A. Rogalski. *Infrared detectors*. Taylor & Francis, 2011.

[100] H. Riris et al. "Airborne measurements of atmospheric methane column abundance using a pulsed integrated-path differential absorption lidar". In: *Appl. Opt.* 34 (2012), pp. 8296–8305.

[101] A. Dumas et al. "Evaluation of a HgCdTe e-APD based detector for 2 μm CO_2 DIAL application". In: *Appl. Opt.* 27 (2017), pp. 7577–7585.

[102] U. N. Singh et al. "Feasibility study of a space-based high pulse energy 2 μm CO_2 IPDA lidar". In: *Appl. Opt.* 23 (2017), pp. 6531–6547.

[103] X. Sun et al. "HgCdTe avalanche photodiode detectors for airborne and space-borne lidar at infrared wavelengths". In: *Opt. Express* 14 (2017), pp. 16589–16602.

[104] G. Ehret et al. "MERLIN: A French-German space lidar mission dedicated to atmospheric methane". In: *Remote Sensing* 10 (2017). ISSN: 2072-4292.

[105] T. Fujii and T. Fukuchi. *Laser remote sensing*. Taylor & Francis, 2005.

[106] D. Sakaizawa et al. "Development of a 1.6 μm differential absorption lidar with a quasi-phase-matching optical parametric oscillator and photon-counting detector for the vertical CO_2 profile". In: *Appl. Opt.* 4 (2009), pp. 748–757.

[107] F. Gibert et al. "Two-micrometer heterodyne differential absorption lidar measurements of the atmospheric CO_2 mixing ratio in the boundary layer". In: *Appl. Opt.* 18 (2006), pp. 4448–4458.

[108] S. Ishii et al. "Ground-based integrated path coherent differential absorption lidar measurement of CO_2: foothill target return". In: *Atmospheric Measurement Techniques* 5 (2013), pp. 1359–1369.

[109] J. Hellström et al. "Real-time and in situ monitoring of ferroelectric domains during periodic electric field poling of $KTiOPO_4$". In: *Journal of Applied Physics* 3 (2001), pp. 1489–1495.

[110] K. Wu et al. "Development of an imaging gas correlation spectrometry based mid-infrared camera for two-dimensional mapping of CO in vehicle exhausts". In: *Opt. Express* 7 (2018), pp. 8239–8251.